UNIVERSITY OF OKLAHOMA

GRADUATE COLLEGE

APPLICATION OF NUCLEAR MAGNETIC RESONANCE TO INVESTIGATE ENHANCED OIL RECOVERY AND GEOSTORAGE OF CO_2 AND H_2

A DISSERTATION

SUBMITTED TO THE GRADUATE FACULTY

in partial fulfillment of the requirements for the

Degree of

DOCTOR OF PHILOSOPHY

By

SIDI MAMOUDOU
Norman, Oklahoma
2025

Downloaded from SHAREOK. Persistent Handle URL: https://hdl.handle.net/11244/341558

APPLICATION OF NUCLEAR MAGNETIC RESONANCE TO INVESTIGATE ENHANCED OIL RECOVERY AND GEOSTORAGE OF CO_2 AND H_2

A DISSERTATION APPROVED FOR THE
MEWBOURNE SCHOOL OF PETROLEUM AND GEOLOGICAL ENGINEERING

BY THE COMMITTEE CONSISTING OF

Dr. Chandra S. Rai, Chair

Dr. Benjamin (Bor-Jier) Shiau

Dr. Deepak Devegowda

Dr. Son T. Dang

Dr. Matthew J. Pranter

© Copyright by SIDI MAMOUDOU 2025
All Rights Reserved.

Acknowledgments

I want to express my deepest gratitude to my family for their unwavering support throughout my doctorate, with special thanks to my aunt, Rahama Beida, for her moral support.

I am immensely grateful to Dr. Rai and Dr. Dang for their invaluable guidance throughout this journey. Their mentorship has challenged my knowledge and elevated my critical thinking.

I would also like to thank Dr. Curtis and Dr. Devegowda for their insightful contributions. Additionally, I thank Dr. Tinni and Dr. Sondergeld for their previous mentorship and advice, which greatly influenced my scientific reasoning.

Special thanks to Micaela Langevin and Gary Stowe (MVP) for their daily assistance and support.

I extend my heartfelt appreciation to my colleagues at the University of Oklahoma for making these years an enjoyable journey, especially Ashutosh Sharma, Tunc Burak, Nabe Konate, Abdelali Guezei, Mohamed Aljishi, Felipe Adriao Cruz, Kachi Ogbonnaya and so many others.

I would also like to thank Encana/Ovintiv and Sandia National Laboratories for their sponsorship of these projects.

Finally, I would like to thank Felipe Perez (El Mejor Amigo) for his kind words and Alexandro Vera (Primo) for our long discussions and walks.

Table of Contents

Acknowledgments iv
List of Tables viii
List of Figures viii
Abstract xv
Chapter 1: Introduction 1
1.1 Motivation 1
1.2 NMR Theory 2
1.3 Laboratory NMR Application in Oil and Gas. 7
1.4 Energy transition a new NMR opportunity 11
1.5 Objectives of this study. 12
1.6 Outline of the dissertation 13
Chapter 2: NMR Application for Improved Recovery Characterization During EOR Huff-n-Puff. 14
2.1 Abstract 14
2.2 Introduction 15
2.2 Methods 16
2.2.1 Sample description 16
2.2.2 Experimental procedure 18
2.2.3 NMR methods 19
2.3 Results 23
2.3.1 Fluid Recovery 23
2.3.2 Hydrocarbon Characterization 26
2.3.3 Pore Size 28
2.3.4 Pore Connectivity 30
2.4 Discussion 34
2.6 Conclusion 38
Chapter 3: Experimental Evaluation of Cement Integrity on Exposure to Supercritical CO2 using NMR: Application to Geostorage. 39
3.1 Abstract 39

3.2 Introduction 40
3.3 Theory and/or Methods 43
3.3.1 Sample Description and Exposure 43
3.3.2 Diffusional Tortuosity 44
3.3.3 Chemical and Microstructural Analysis 46
3.3.3 Pore Structure Alteration 47
3.4 Results 47
3.4.1 Diffusional Tortuosity 47
3.4.2 Pore Structure Alteration 50
3.4.3 Chemical and Microstructural Analysis 51
3.5 Discussion 55
3.6 Conclusions 57
Chapter 4: Hydrogen Interaction in Bulk Fluids for Geological Storage Application Using NMR 58
4.1 Abstract 58
4.2 Introduction 59
4.3 Theory and/or Methods 61
4.3.1 Sample Selection 61
4.3.2 Experimental Procedure 62
4.3.3 T_2 Subtraction and Hydrogen Signal Analysis 63
4.4 Results 64
4.4.1 Deuterated and DI water 64
4.4.2 Fluorinert 66
4.4.3 Hydrocarbons 68
4.5 Discussion 71
4.6 Conclusion 73
Chapter 5: Hydrogen Interaction in Cyclohexane Using NMR for Geostorage Application 75
5.1 Abstract 75
5.2 Introduction 75
5.3 Theory and/or Methods 76
5.4 Results 77

5.4.1 Hydrogen vaporization 77
5.5 Discussion 81
5.6 Conclusion 82
Chapter 6: Evaluation of Hydrogen Storage in Sandstone and Shales using NMR. 83
6.1 Abstract 83
6.2 Introduction 83
6.3 Experimental Methods 85
6.3.1 Sample description and experimental apparatus 85
6.3.2 Baseline signal subtraction 87
6.4 Results 87
6.4.1 Free hydrogen signal 87
6.4.2 Hydrogen in shales 88
6.4.3 Hydrogen in sandstones 91
6.5 Discussion 94
6.6 Conclusion 94
General Conclusion and Recommendations for Future Work 95
References 98

List of Tables

Table 2.1 - Eagle Ford and Wolfcamp sample description. Liquid-filled porosity and the oil saturation were measured with NMR (T_2 and T_1-T_2 maps) on the samples in the "as-received state." TOC was measured using a LECO instrument, and the mineralogy was based on transmission Fourier transform infrared spectroscopy (FTIR) (Sondergeld and Rai 1994). 16
Table 2.2 - Eagle Ford and Wolfcamp samples used for EOR (white color) and pressure stepped saturation (yellow color). Note: For the Eagle Ford samples the dominant clay was Illite, while for the Wolfcamp samples the total clays were a combination of Illite and mixed clays. 30
Table 3.1- X-ray fluorescence-derived mineralogy measured on the untreated cement, showing mostly CaO and SiO_2 components. 43
Table 3.2 - Derived tortuosity from Figure 3.6. The tortuosity increased by 6 and only by 3 after 2 and 5 weeks, respectively. This suggests an initial precipitation of calcium carbonate and a later dissolution. 50
Table 6.1 - Petrophysical sample description. 85

List of Figures

Figure 1.1 - Diagram illustrating an inversion recovery pulse sequence (a) alongside the raw data obtained after inversion from the sequence (b). The detected NMR signal is referred to as the echo (Tinni 2015). 3
Figure 1.2 - Diagram depicting a CPMG sequence (a) and the raw data obtained following the inversion sequence. Here, τ corresponds to TE/2. Lower TE values result in shorter observable relaxation times (Tinni 2015). 3
Figure 1.3 - Diagram showing a T_1-T_2 sequence (a) and the raw data obtained from the sequence (b). The observed spikes represent the first echoes recorded at each time interval (Tinni 2015)... 4
Figure 1.4 - Expected T_1-T_2 response for hydrocarbons in shales (Fleury and Romero-Sarmiento 2016). 6
Figure 1.5 - NMR uptake of dodecane (A) and brine (B) as a function of TOC and clay content in shales. Results indicate that a minimum of 2-3 wt% TOC and 20% clay content is required to establish connectivity between organic and inorganic pores (Tinni 2015). 8
Figure 1.6 - Example of visual representation of pore partitioning in Barnet shale sample after brine, dodecane saturation and $MnCl_2$ imbibition using NMR (Gannaway 2014) 9
Figure 1.7 - NMR application in EOR Huff-n-Puff optimization highlighting the impact of gas composition in Eagle Ford shale. The study demonstrates solvent performance, with ethane and CO_2 identified as the most effective solvents for this shale (Min et al. 2020). 10
Figure 1.8 - Real-time NMR recovery in a shale plug highlighting the impact of diffusion. The recovery during injection phases follows a similar trend to recovery during production phases,

suggesting that diffusion plays a dominant role in Huff-n-Puff recovery, as opposed to convective flows (Dang 2019). 11
Figure 2.1 - Pore throat (A) and pore body (B) size distributions of dry Eagle Ford and Wolfcamp samples. Pore throat sizes were determined using MICP, while pore body sizes were derived from nitrogen adsorption data analyzed via density functional theory with a slit-shaped pore model. The surface area was calculated using the Brunauer-Emmett-Teller (BET) theory (Brunauer et al. 1938). MICP results show pore sizes below 10 nm for both samples, indicating tight formations. Nitrogen adsorption further confirms a greater volume of nanopores in the Wolfcamp sample compared to Eagle Ford. 17
Figure 2.2 - HAWK® modified dry pyrolysis technique for hydrocarbon potential assessment. S1 dry pyrolysis is broken down into 4 peaks (S11-S14). The results indicate that the Eagle Ford sample has higher hydrocarbon content (particularly in light hydrocarbons, $<C_{13}$) compared to Wolfcamp. 18
Figure 2.3 - Huff-n-puff experimental schematic. The sample is placed inside a high-pressure cell located within an oven. A mixture of C_1:C_2 (72:28) is injected into the high-pressure cell via a pump station with precise pressure control; the pressure vessel outlet has a production choke to control the production rate and time. 19
Figure 2.4 - NMR T_2 distribution of an Eagle Ford sample before and after a single injection cycle (5-hour soak, 3-hour production) with a C_1:C_2 (72:28) gas mixture at 150°F and 4000 psi. The results show a 0.23 cc fluid volume reduction after injection. The pre- and post-EOR decay curves were subtracted, and the resulting decay curve was inverted using Green Imaging Software to obtain the T_2 distribution and determine the total fluid produced volume. 20
Figure 2.5 - 2D T_1-T_2 maps used for fluid characterization of the data in Figure 2.4. After subtraction of the pre (A) and post (B) injection maps, the amplitude of both the water and hydrocarbon signals was reduced, but the bound water signal (interlayer water and structural hydroxyl) stays the same. (C). Note: All three figures are plotted on the same scale, and SNR>45 was achieved pre- and post-EOR. However, the produced volume (i.e., subtracted) SNR ranged from 10-15 due to the small amount of fluid produced. 22
Figure 2.6 - NMR produced volumes of water and hydrocarbon calculated by integrating T_1-T_2 maps and T_2 relaxation data after one gas injection cycle with a mixture of C_1:C_2 (72:28). 23
Figure 2.7 - Oil and water recovery for the Eagle Ford sample, shows oil recovery increasing to 25% after six cycles, while water recovery plateaus at 15% after three cycles. 24
Figure 2.8 - Oil and water recovery for the Wolfcamp sample, with water recovery reaching 27% and oil recovery limited to 10% after seven cycles, reflecting its high-water saturation and clay content. 24
Figure 2.9 - Water–Oil Ratio (WOR) versus Huff-n-Puff cycle for Eagle Ford and Wolfcamp samples. Eagle Ford shows a gradual increase in WOR, while Wolfcamp transitions rapidly to water-dominated production after cycle 2. 25
Figure 2.10 - HAWK® analysis on Eagle Ford crushed sample pre and post EOR showing preferential vaporization of lighter hydrocarbons S11 and S12. 27

Figure 2.11 - HAWK® analysis on Wolfcamp crushed sample pre and post EOR showing preferential vaporization of lighter hydrocarbons S11 and S12. 27
Figure 2.12 - Evolution of the produced fluids over time using molecular simulation after 6ns using C_1:C_2 (72:28) in black oil nanopores showing preferential vaporization of the methane and intermediate species (Perez and Devegowda 2020)..... 28
Figure 2.13 - NMR T_2 relaxation obtained from the subtracted signal showing the produced volume as a function of cycles in Eagle Ford. Most fluid production originates from T_2 >1 ms (i.e., large pores). 29
Figure 2.14 - NMR T_2 relaxation obtained from the subtracted signal showing the produced volume as a function of cycles in Wolfcamp. The results indicate that most fluid production originates from T_2 <1 ms pores (i.e., small pores) except for cycle 1..... 29
Figure 2.15 - NMR T_2 relaxation during pressure stepped saturation in Eagle Ford 2 with 2.5% KCl brine, shows initial intrusion in inorganic pores (T_2<1ms) up to 750 psi. After 1000 psi injection, brine starts to invade organic pores (T_2 =1-10ms). Note: Relaxation time around 100ms is attributed to brine present in larger pores or cracks in the sample..... 32
Figure 2.16 - NMR porosity of Eagle Ford 2 during pressure-stepped saturation in 2.5% KCl brine shows an inflection around 850 psi, where connection is established with organic pores. The organic porosity represents 2.4 %. Note: 1 psi corresponds to the dried state, and 14 psi corresponds to the porosity after imbibition. 33
Figure 2.17 - NMR porosity of Wolfcamp 2 during pressure-stepped saturation in 2.5% KCl brine shows an inflection at 300 psi where the connection is established between inorganic and organic pores. Most connectivity is established during imbibition as brine enters inorganic and mixed wet pores. 33
Figure 2.18 - NMR porosity as a function of pressure during dodecane saturation for Eagle Ford and Wolfcamp samples, shows flat profiles indicative of full pore access during imbibition and minimal pure inorganic wet porosity. 34
Figure 2.19 - Pore connectivity model in shales based on NMR saturation uptake using 2.5% KCl brine at 7000 psi (Tinni 2015). The Eagle Ford sample corresponds to Type 2 connectivity, characterized by an organic network with some mixed wet pore network, organized in a pseudo-parallel flow network. In contrast, the Wolfcamp aligns with Type 3 connectivity, where fluid flow is entirely controlled by the clay matrix in a serial flow configuration..... 35
Figure 2.20 - Proposed pore connectivity and depletion model for the Eagle Ford shale during EOR. (a) The formation is characterized by a Type 2 connectivity structure with pores organized in pseudo-parallel: organic pores (black), mixed-wet pores (gray), and unconnected pores (yellow). (a)The sample is made of large mixed wet and small organic pore throats. (b) Before EOR, hydrocarbons fill the organic pores (green), and mixed-wet pores host both fluids. (c) During early solvent injection (C_1:C_2 72:28), hydrocarbons are preferentially vaporized from the organic pores. (d) With continued injection, water is incrementally displaced from mixed wet pores, leading to sustained oil and water production over multiple cycles. (e) Following depletion, some water and oil remain trapped within mixed wet pores and unconnected pores.. 36

Figure 2.21 - Proposed pore connectivity and depletion model for the Wolfcamp shale during EOR. (a) This formation follows a Type 3 connectivity model with serial flow dominated by mixed wet pores (a). (b) Before EOR, larger mixed-wet pores contain hydrocarbons while smaller mixed-wet pores are water saturated c) During early solvent injection, lighter hydrocarbons are vaporized preferentially. (d) After depletion of most hydrocarbons, water is mobilized intermittently due to capillary-driven displacement from clay-bound pore throats, leading to episodic water production. (e) Post-EOR, most hydrocarbons are depleted, while some hydrocarbons remain confined within the mixed wet pore network..... 37
Figure 3.1 - Experimental workflow used in the present study. Flow path alteration was determined by comparing D_2O-brine diffusivity before and after exposure to $scCO_2$. 44
Figure 3.2 - Schematic of CO_2 exposure apparatus. Exposure was carried out at 20.7 MPa and 65°C, conditions at which CO_2 is in a supercritical state. 44
Figure 3.3 - NMR T_2 relaxation distribution of the controlled cement plug immersed in D_2O-brine showing a gradual decrease in volume of the H_2O-brine as D_2O-brine replaces H_2O-brine inside the plug. Over 168 hours, the volume of H_2O-brine decreased from 6.7 to 2.3 ml (dashed curves)..... 48
Figure 3.4 - NMR T_2 relaxation distribution during immersion in D_2O-brine after 2 weeks (a) and 5 weeks (b) exposure of cement plugs to $scCO_2$ showing 40% vs 27% D_2O-brine intrusion after 5 weeks and 2 weeks, respectively..... 48
Figure 3.5 - Comparison between the untreated and 5 weeks $scCO_2$ exposed cement after 100% saturation with H_2O-brine showed a reduction in a pore volume between 0.3 -10 ms, resulting in an overall 10 % loss of pore volume after exposure..... 49
Figure 3.6 - D_2O-brine intrusion profile on the cement plugs after 2 and 5 weeks- of exposure to $scCO_2$ at 65°C and 20.7 MPa, showing D_2O-brine flow reduction after $scCO_2$ exposure. 50
Figure 3.7 - (a) MICP pore throats and (b) DFT pore body size distribution after 2- and 5-weeks exposure to $scCO_2$ at 65°C and 20.7 MPa. MICP data shows a decrease in pore throat size (ie: connectivity) of the cement after carbonation. N_2 isothermal adsorption shows initial dissolution and later precipitation of $CaCO_3$ in large pores (>30nm), while only dissolution in small pores (2-30 nm). 51
Figure 3.8 - XCT images of the 3 different cement samples showing the $scCO_2$ invaded (yellow arrow) and the non-invaded (white arrow) after 2 weeks (B) and 5 weeks (C) exposure to $scCO_2$ at 65°C and 20.7 MPa. A deeper invasion is observed after 5 weeks. Note: Each cross section was taken 0.25 inches from the top of the plugs to capture the $scCO_2$ front. 53
Figure 3.9 - FTIR mineralogy of the cement (A) untreated, (B) after 2 weeks, and (C) 5 weeks exposure to $scCO_2$, showing calcite absorbance bands around 1400 cm^{-1}, and 875 cm^{-1}. 53
Figure 3.10 - Backscattered electron image after 5 weeks of exposure to $scCO_2$ at 65°C and 20.7 MPa. Clear textural demarcation can be observed between the invaded and non-invaded zones. The area invaded by $scCO_2$ appears darker, and the cement grain and matrix appear altered, with less $CaOH_2$ and C-S-H. Note: The cement was imaged without coating. 53

Figure 3.11 - EDS maps at the boundary between carbonated and non-carbonated zones after 5 weeks of $scCO_2$ exposure at 65°C and 20.7 MPa. The dashed line represents the $scCO_2$ front. After exposure, the unhydrated cement grains have been decalcified in the $scCO_2$-invaded zone. The invaded zone matrix appears to have less Si but more magnesium and carbon. Note magnesium seems to be localized near the $scCO_2$ front only. 54
Figure 3.12 - 9 scan lines were used to determine the elemental profiles (Ca, Si, Mg, and C) over the altered region shown in Figure 3.10 and Figure 3.11. Each line is 45 µm wide (20 pixels) and 500µm long. Elemental composition was measured by averaging the grayscale intensity of the lines for each component. 54
Figure 3.13 - Elemental profiles generated from the X-ray map (Figure 3.12) of cement exposed to $scCO_2$ at 65°C and 20.7 MPa for 5 weeks. This data corresponds to an average elemental composition of 9 vertical scans. Position 10 µm corresponds to the top of the SEM image ($scCO_2$-invaded zone), while position 510 µm corresponds to the bottom section of the SEM image (the non-invaded zone) of the cement. The $scCO_2$ invaded zone appears richer in calcium and carbon mostly. Mg is also present near the carbonation front (≈200 µm) 55
Figure 4.1 - The diagram illustrates the flow of hydrogen gas from the hydrogen cylinder (left) through an ISCO pump, which compresses the gas and injects it into the NMR-compatible core holder (center) containing the fluid sample. The core holder, made of NMR-transparent ZrO_2, is positioned inside the NMR spectrometer probe, and glass beads with no NMR signal were placed at the bottom to ensure that the sample is centered in the uniform magnetic field section for optimal measurements. Note: A Lexan shield is placed around the apparatus for safety purposes. 63
Figure 4.2- T_2 relaxation during hydrogen injection into D_2O is shown as a function of pressure, highlighting the free gaseous hydrogen signal in machine units (m.u), relaxing within 1–20 ms over the experimental pressure range. 65
Figure 4.3 - T_2 relaxation during hydrogen injection into DI water is shown as a function of pressure, highlighting the presence of free hydrogen with relaxation times between 1–10 ms and bulk DI water at 3000 ms. The water signal decreases slightly due to compressibility but remains constant with pressure, with limited interaction with DI water. 65
Figure 4.4 - T_2 relaxation data during H_2 injection into the fluorinert after baseline subtraction, showing free hydrogen (1–20 ms), an intermediate signal (100–300 ms) attributed to potentially dissolved hydrogen, and a slow relaxation signal (>1000 ms) corresponding to trace water. Note: The scale in this figure is smaller than in Figures 4.1 and 4.2 to improve visualization. 66
Figure 4.5 - HI for different injection pressure points at room temperature (NIST handbook). .. 67
Figure 4.6 - Fluorinert post hydrogen injection showing hydrogen bubbles (red arrows) in solution. The image was taken post-experiment at ambient pressure. 68
Figure 4.7 - T_2 relaxation data before (A) and after (B) dodecane subtraction is shown as a function of H_2 injection pressure. After subtracting the baseline dodecane signal in blue (1000–2000 ms), only the free H_2 signal remains between 1–10 ms, suggesting that no H_2 interaction with dodecane. 69

Figure 4.8 - Dead oil composition measured by gas chromatography showing a wide range of alkanes from C_9-C_{17}. 69
Figure 4.9 - T_2 relaxation data before (A) and after (B) Eagle Ford dead oil baseline subtraction are shown as a function of H_2 injection pressure. After subtracting the dead oil signal (35–4000 ms), only the free H_2 signal remains, indicating no interaction of H_2 with the oil. 70
Figure 4.10 - Dead oil post hydrogen injection showing hydrogen bubbles (red arrows) coming out of the solution. 70
Figure 4.11 - T_2 relaxation data before (A) and after (B) subtraction of the ozokerite wax signal (0.1–300 ms) are shown as a function of H_2 injection pressure, indicating only free H_2 with no interaction with the wax. 71
Figure 4.12 - Summary of hydrogen interaction in our study as a function of pressure after baseline subtraction. Only free hydrogen signals are detected, appearing within the 1–20 ms relaxation time window. While the NMR peak shapes vary across fluids, the total hydrogen signal remains relatively consistent. For example, at 1500 psi, the cumulative signal for all fluids ranges between 2.45 and 2.49 cc. 73
Figure 5.1 - Experimental schematic illustrating the vaporization and dissolution experiments with cyclohexane. The ZrO_2 cell, filled with cyclohexane, is positioned inside the NMR instrument. In the first experiment, the free gaseous hydrogen signal is monitored to determine vaporization of cyclohexane, while in the second experiment, the bulk liquid cyclohexane is monitored to assess hydrogen dissolution. 77
Figure 5.2 - T_2 relaxation data during hydrogen injection at 1500 psi in cyclohexane showing minimal change in free hydrogen signal (10 ms) after 3 days. 78
Figure 6.1 - General NMR experimental apparatus. The plug sample is placed inside an NMR transparent ZrO_2 pressure cell, placed within a 2 MHz NMR spectrometer. Hydrogen is compressed using a Teledyne Isco pump filled with water inside an accumulator. Fluorinert is used in a second pump to supply confining pressure. 86
Figure 6.2 - Jacketed Berea sandstone positioned between two PEEK (Polyether Ether Ketone) core holders. The sample is wrapped in shrink-fit Polytetrafluoroethylene (PTFE) before assembly inside the ZrO_2 cell. 86
Figure 6.3 - NMR T_2 relaxation of free hydrogen at room temperature at different pressures up to 1500 psi (Ho et al. 2024). 88
Figure 6.4 - NMR T_2 distribution of H_2 in Eagle Ford, Duvernay and Marcellus. The Eagle Ford and Duvernay show similar responses to bulk hydrogen, however, for the Marcellus, from the gas window, relaxation distribution split into 2 peaks, which could be due to the presence of sub-nanometer pores. 89
Figure 6.5 - H_2 porosity measured by NMR (5000 psi) comparison with helium porosity. Good agreement is observed between the H_2 occupied porosity and helium porosity, showing that hydrogen can fill all empty pore space. 90
Figure 6.6 - H_2 intake during loading and unloading in Eagle Ford, Duvernay, and Marcellus shales up to 5000 psi. The results show minimal to no hysteresis. 90

Figure 6.7 - NMR T_2 relaxation for the Berea sandstone at dried and partially saturated conditions. 91
Figure 6.8 - NMR T_2 distribution of H_2 in Berea at different saturations (dry, sw=30% and Sw=80%). 92
Figure 6.9 - Comparison between H_2 NMR measured porosity (at 5000 psi) with calculated helium porosity. NMR-measured porosity matches helium porosity. Note: Helium porosity was measured on the sample in a dried state only. 92
Figure 6.10 - H_2 intake between loading and unloading H_2 into dried and partially saturated (Sw = 80%) Berea sandstone. Insignificant hysteresis is observed regardless of water saturation. 93

Abstract

The global energy transition demands innovative technologies to address growing energy needs while mitigating environmental impact. Nuclear Magnetic Resonance (NMR) relaxometry has emerged as a powerful tool for characterizing reservoir properties and fluid behavior, offering significant potential for applications in enhanced oil recovery (EOR), carbon capture and storage (CCS), and underground hydrogen storage (UHS). This study explores the capabilities of NMR in addressing the critical challenges associated with these energy transition technologies.

First, NMR was applied to evaluate fluid recovery during Huff-n-Puff (HnP) EOR in shale reservoirs on preserved samples from the Eagle Ford and Wolfcamp using a mixture of C_1:C_2 (72:28) gas. Pressure stepped saturation using 2.5% KCl brine and dodecane was used to understand organic versus inorganic pore throats connectivity. Results show that oil production in Eagle Ford and Wolfcamp formations using C_1:C_2 (72:28) is primarily driven by the vaporization of lighter hydrocarbons (below C_{13}), while free water production is controlled by wettability and pore connectivity. The Eagle Ford formation exhibited continuous oil production (25% recovery) and moderate water recovery (15%), attributed to its well-connected organic pore network (pseudo parallel connectivity). In contrast, the Wolfcamp formation, characterized by high clay content (serial flow connectivity), showed limited oil recovery (10%) and higher water recovery (27%), with episodic water breakthrough after early oil production. These findings highlight the critical role of pore structure and connectivity in governing recovery behavior during EOR.

For CCS applications, NMR was employed to assess the integrity of Class G cement exposed to supercritical CO_2 ($scCO_2$). The results showed that $scCO_2$ exposure led to precipitation and dissolution of calcium carbonate, leading to a reduction of porosity from 37% to 33% over five weeks. Notably, diffusional tortuosity increased sixfold after two weeks but later decreased to

threefold after five weeks, suggesting an initial sealing stage followed by a dissolution phase. The extent of reaction was found to be pore-size dependent: in smaller pores (<30 nm), carbonate dissolution dominated, while in larger pores (30–200 nm), both precipitation and dissolution were observed. These findings indicate that $scCO_2$ exposure can alter the flow path in cement, potentially limiting CO_2 migration and leakage over time.

In the UHS study, NMR was used to investigate hydrogen solubility in organic and inorganic bulk fluids. Experiments revealed that hydrogen remains primarily in the free phase in water and hydrocarbons, with negligible solubility observed in dodecane, dead oil, and ozokerite wax. However, fluorinert HT-230 (used as confining fluid for NMR plug measurement) exhibited measurable hydrogen solubility (4–6 cc of H_2 per 100 cc of fluorinert at 1800 psi). Additionally, long-term experiments in cyclohexane demonstrated progressive hydrogen dissolution over 32 days, increasing the hydrogen index (HI) by 3.42%, confirming slow but measurable uptake. These results highlight caution during signal processing and interpretation using hydrogen gas.

Further, NMR was applied to assess hydrogen storage in rocks, including organic-rich shales (Eagle Ford, Duvernay, Marcellus) and partially brine-saturated Berea sandstone. Results indicated that hydrogen occupied the entire pore network in shales, with minimal interaction with the organics and clays, regardless of maturity. In sandstones, hydrogen storage capacity was also directly proportional to available pore space, with no significant hysteresis observed, confirming full recovery potential.

Overall, this study demonstrates that NMR provides critical insights into fluid transport, phase behavior, and storage mechanisms relevant to EOR, CCS, and UHS. By quantifying fluid-rock interactions with high precision, NMR enhances our ability to optimize energy storage and

recovery strategies in the subsurface, contributing to the development of sustainable energy solutions.

Chapter 1: Introduction

1.1 Motivation

Nuclear Magnetic Resonance logging is a powerful tool for characterizing subsurface formations by directly measuring porosity, fluid distribution, and permeability. Unlike conventional well-logging techniques, which rely on indirect interpretations of rock and fluid properties, NMR measures the relaxation times of hydrogen nuclei, offering a precise understanding of pore structure and fluid behavior (Kenyon 1997). One of its key advantages is that it provides a lithology-independent measurement of total porosity, overcoming the limitations of conventional porosity estimations from neutron/density and sonic tools (Coates et al. 1999). This capability has made NMR logging essential for reservoir evaluation, particularly in complex or low-permeability formations (Freedman 2006).

Key research contributions have driven the development and refinement of NMR logging. Timur (1968, 1969) established empirical relationships between NMR relaxation times and permeability, forming the foundation for permeability estimation in sandstones. Daigle and Dugan (2011, 2009) further improved these models, particularly for unconsolidated sediments, enhancing the applicability of NMR in fine-grained and unconventional reservoirs. Schlumberger-Doll Research (SDR) played a pivotal role in commercializing NMR logging technology, developing the widely used SDR permeability model that links relaxation time distributions to petrophysical properties (Kleinberg 2001, 1996). Kenyon et al. (1988) expanded the interpretation of NMR signals, improving the understanding of pore-size-dependent relaxation mechanisms. Coates et al. (1999) introduced a permeability model incorporating a free-fluid and bound-fluid index, making NMR more applicable in complex lithologies, including carbonates.

1.2 NMR Theory

NMR relaxometry measures the magnetic properties of hydrogen nuclei in pore fluids under the influence of an external magnetic field and radiofrequency (RF) pulses. The behavior of these nuclei is characterized by two key parameters: T_1 relaxation (longitudinal relaxation time) and T_2 relaxation (transverse relaxation time). These parameters reflect the rate of magnetization recovery and decay, respectively, and are influenced by fluid properties, pore size, and pore-fluid interactions (Coates et al. 1999).

In well logging, NMR tools typically operate at low frequencies (ranging from 200 kHz to 2 MHz) due to limitations imposed by borehole conditions and tool design (Kleinberg and Jackson 2001). This low-frequency operation enhances sensitivity to bulk fluid properties and larger pore sizes but limits resolution for detecting fine-scale variations (Coates et al. 1999). Conversely, laboratory NMR instruments function at significantly higher frequencies (tens to hundreds of MHz), providing greater precision in relaxation time measurements and better differentiation of fluid types and pore structures (Mitchell et al. 2014). The increased signal-to-noise ratio in laboratory settings allows for detailed T_1 and T_2 spectra analysis, making it possible to distinguish between bound and free fluids with higher accuracy (Kenyon 1997, Dunn et al. 2002).

In the laboratory, T_1 is typically measured using an inversion recovery pulse sequence, which involves a 180° RF pulse followed by a 90° RF pulse, with increasing time intervals between them **(Figure 1.1)**. T_2 is typically measured using the Carr-Purcell-Meiboom-Gill (CPMG) sequence, consisting of a 90° RF pulse followed by a series of 180° RF pulses **(Figure 1.2**). The data from these sequences are processed based on an exponential decay to generate T_1 and T_2 spectra **(Figure 1.3),** which represent pore fluid distribution in the sample. Furthermore, T_1-T_2 mapping combines these parameters to differentiate fluid types, particularly when viscosity contrasts are significant,

with low-viscosity fluids showing $T_1 \approx T_2$ and high-viscosity fluids displaying $T_1 >> T_2$ (Bloembergen et al. 1948).

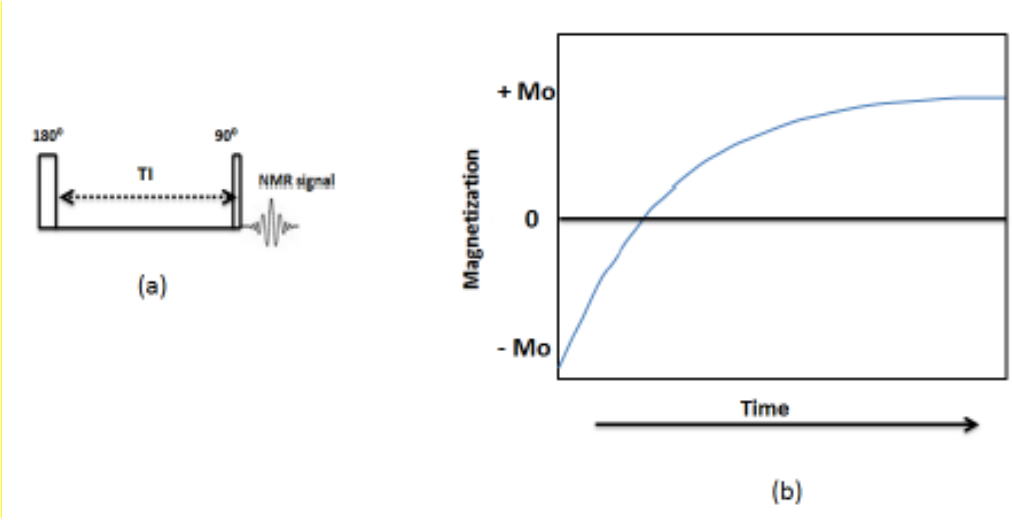


Figure 1.1 - Diagram illustrating an inversion recovery pulse sequence (a) alongside the raw data obtained after inversion from the sequence (b). The detected NMR signal is referred to as the echo (Tinni 2015).

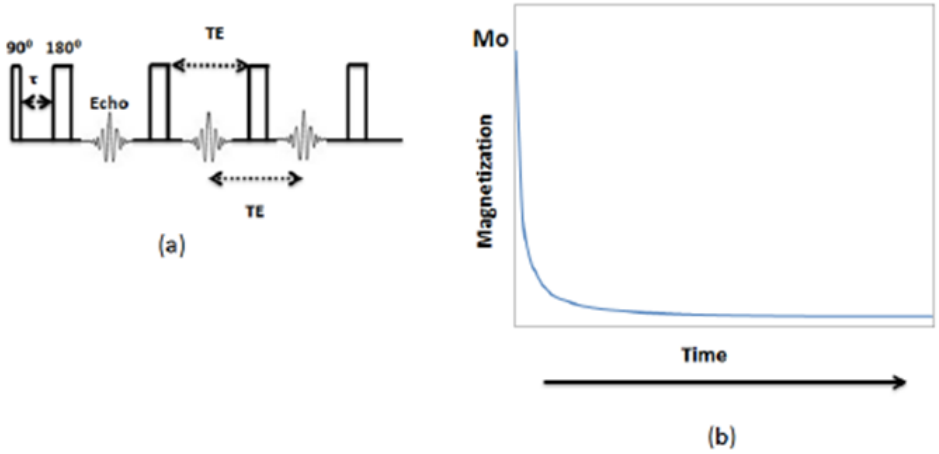


Figure 1.2 - Diagram depicting a CPMG sequence (a) and the raw data obtained following the inversion sequence. Here, τ corresponds to TE/2. Lower TE values result in shorter observable relaxation times (Tinni 2015).

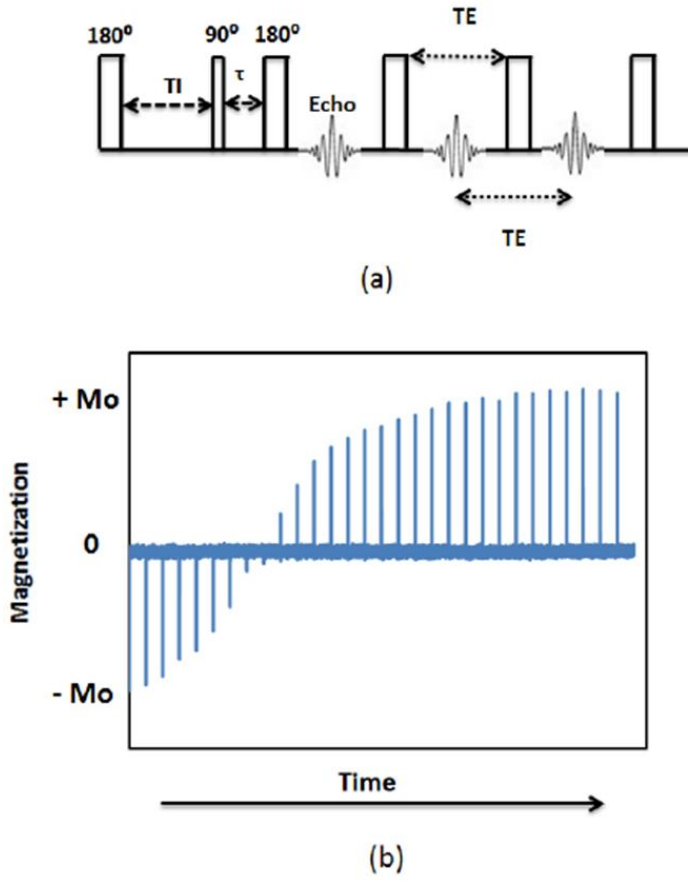


Figure 1.3 - Diagram showing a T_1-T_2 sequence (a) and the raw data obtained from the sequence (b). The observed spikes represent the first echoes recorded at each time interval (Tinni 2015).

The relaxation mechanisms governing T_1 and T_2 in porous media can be described in **Equation 1.1** and **Equation 1.2** (Coates et al. 1999):

$$\frac{1}{T_2} = \frac{1}{T_{2\,bulk}} + \frac{1}{T_{2\,Surf}} + \frac{1}{T_{2\,Diff}} \qquad 1.1$$

$$\frac{1}{T_1} = \frac{1}{T_{1\,bulk}} + \frac{1}{T_{1\,Surf}} \qquad 1.2$$

1. Bulk Relaxation (T_{bulk}): Determined by the inherent properties of the fluid, such as viscosity and composition. Bulk relaxation dominates in larger pores, where fluid interactions with pore walls are minimal.

2. Surface Relaxation (T_{surf}): Arises from interactions between fluid molecules and solid pore surfaces. It depends on the pore surface-to-volume ratio (S/V) and is influenced by the mineralogy and surface chemistry of the rock.

3. Diffusion Relaxation (T_{diff}): Occurs due to molecular diffusion in the presence of magnetic field gradients, leading to dephasing of the magnetic signal. This effect is particularly significant in fine-grained rocks with strong field gradients. In a homogeneous magnetic field, this term drops.

In addition, for rocks, the internal diffusion distances are short and surface relaxivity ($T_{2\ surf}$) dominates; therefore diffusion ($T_{2\ diff}$) is typically negligible and dropped. This allows for simpler T_2 models based primarily on bulk and surface relaxation**.** For T_1 relaxation, the diffusion component drops as well because T_1 relaxation is controlled by energy exchange between nuclear spins and their molecular environment. Therefore, T_1 can be modeled based on bulk fluid properties (Bloembergen et al. 1948, Coates et al. 1999).

NMR measurements also provide quantitative porosity estimates based on the hydrogen content of fluids in the rock. The raw data are processed using a single or multi-exponential fitting algorithm, and the area under the NMR spectra corresponds to the hydrogen-based fluid content. In applications involving mixed fluids, such as water and hydrocarbons, the hydrogen index (HI) of each fluid is used to calibrate porosity measurements. For water and light hydrocarbons, the HI = 1 (Dunn et al. 2002) and can be computed using **Equation 1.3:**

$$\emptyset_f = \frac{\emptyset_w}{HI} \qquad 1.3$$

Where $\emptyset_f$ is the fluid porosity (fraction or %), $\emptyset_w$ is the water-based porosity (fraction or %), and HI is the hydrogen index of the fluid.

For gases, the hydrogen index depends on the gas density and molecular structure, with lower densities and fewer hydrogen atoms resulting in significantly lower HI values compared to liquids, and can be computed using **Equation 1.4** (Hirasaki and Mohanty 2007):

$$HI = \frac{\rho N_H M}{0.111} \qquad 1.4$$

Where ρ is the gas density (g/cm^3), N_H is the number of hydrogen atoms contained in the gas molecule, and M is the molecular weight (g/mol).

NMR theory also extends to T_1-T_2 correlation mapping, enabling the identification of fluid types for a given sample based on viscosity contrasts (Bloembergen et al. 1948). For example, highly viscous fluids exhibit shorter T_2 and longer T_1 relaxation times, while movable fluids show $T_1 \approx T_2$. Therefore T_1/T_2 ratio can be used for fluid typing in shales (Fleury and Romero-Sarmiento 2016, Tinni et al. 2014) **(Figure 1.4).**

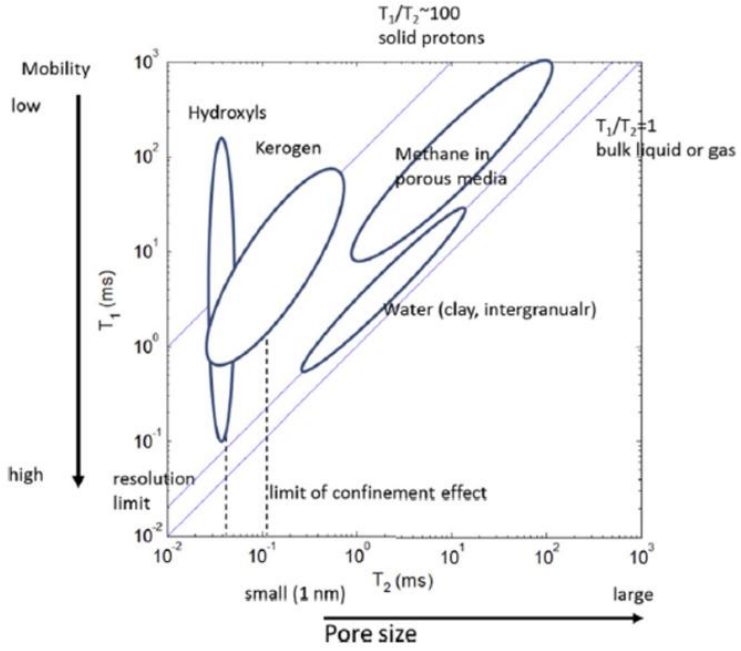


Figure 1.4 - Expected T_1-T_2 response for hydrocarbons in shales (Fleury and Romero-Sarmiento 2016).

1.3 Laboratory NMR Application in Oil and Gas.

Laboratory NMR has been extensively used for petrophysical evaluations to study reservoir fluid properties, rock wettability, pore connectivity, hydrocarbon storage mechanisms, and performance during enhanced oil recovery.

Hirasaki et al. (2003) established a correlation between NMR relaxation times and fluid viscosity, highlighting that the T_2 relaxation time is strongly dependent on crude oil viscosity. Kausik et al. (2011) studied NMR relaxation and diffusion properties of natural gas in shale nanopores, demonstrating that the NMR response in nanopores differs from that of bulk gas (methane) due to restricted diffusion, adsorption, and enhanced surface relaxation.

Sulurcarnain et al. (2012) and Odusina et al. (2011) demonstrated NMR's capability to identify mixed wettability in organic-rich shales by monitoring sequential brine and oil imbibition. The study found that surface relaxivity dominated the NMR signal, correlating with fluid distributions and wettability states, while Total Organic Carbon (TOC) and organic pore volume significantly influenced oil imbibition.

Building on these insights, Tinni (2015) expanded NMR applications to assess pore connectivity and hydrocarbon storage mechanisms. Through pressure saturation experiments, Tinni quantified the conditions required for continuous water-wet and hydrocarbon-wet pore networks, identifying clay content (20 wt%) and TOC (3–4 wt%) as critical thresholds for connectivity **(Figure 1.5)**. Additionally, Tinni et al. (2014) utilized T_1-T_2 maps to differentiate movable and non-movable fluids in conventional and unconventional rocks. T_1-T_2 ratios revealed fluid types and viscosity contrasts, such as the T_1/T_2 ratio of 1.5 for brine and 2.5–3.0 for movable hydrocarbons. Non-

movable hydrocarbons, such as bitumen, exhibited significantly higher T_1/T_2 ratios (e.g., 20–400), further showcasing NMR's capability to characterize fluid behavior in shales.

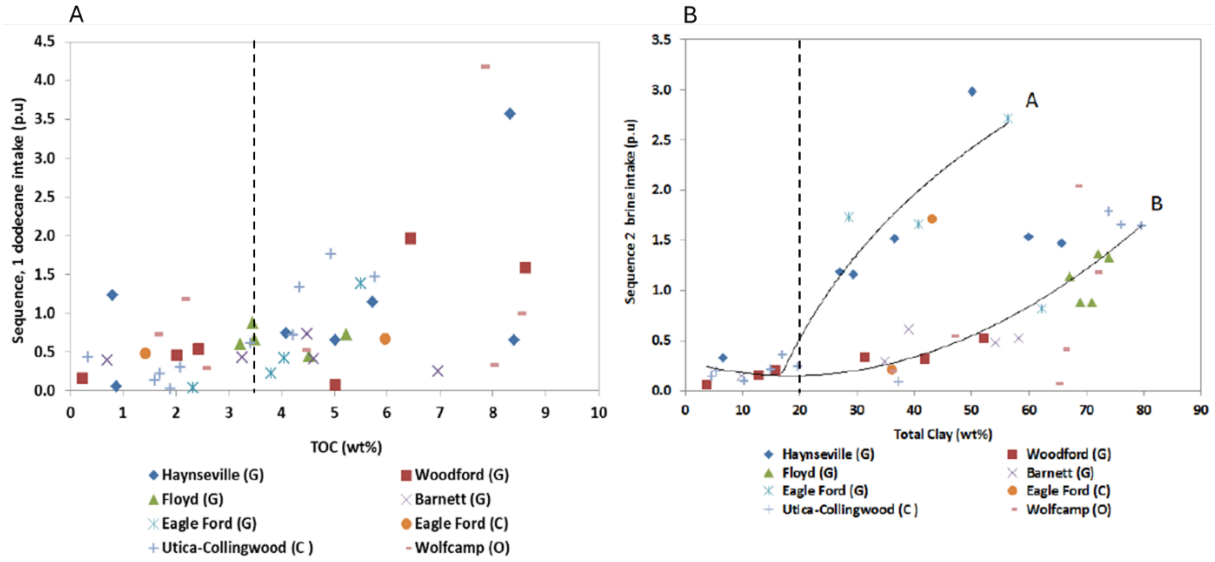


Figure 1.5 - NMR uptake of dodecane (A) and brine (B) as a function of TOC and clay content in shales. Results indicate that a minimum of 2-3 wt% TOC and 20% clay content is required to establish connectivity between organic and inorganic pores (Tinni 2015).

In parallel, Gannaway (2014) study leveraged NMR to investigate porosity partitioning among different pore systems in gas shales, emphasizing the contrasts between organic and inorganic pore spaces **(Figure 1.6)**. By using manganese chloride ($MnCl_2$) solutions to suppress the NMR signal of water in inorganic pores, the study isolated and quantified organic porosity. Gannaway highlighted a positive correlation between TOC and organic pore volume and demonstrated NMR's potential for differentiating porosity at the organic-inorganic interface. This work validated NMR as a powerful tool for characterizing the complex dual-porosity systems in shales, including the assessment of bound water and effective porosity.

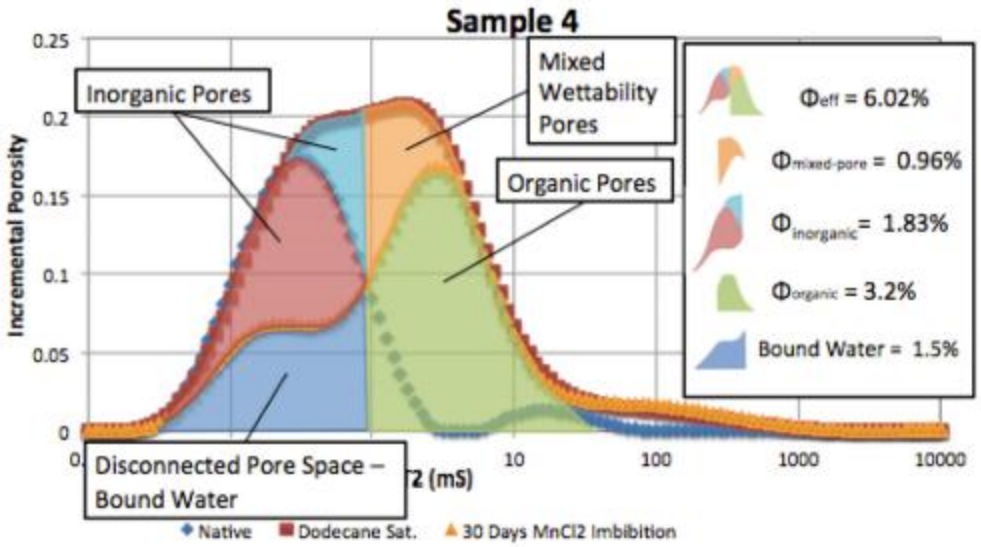


Figure 1.6 - Example of visual representation of pore partitioning in Barnet shale sample after brine, dodecane saturation and $MnCl_2$ imbibition using NMR (Gannaway 2014)

Huff-n-Puff Enhanced Oil Recovery (HnP-EOR) has also benefited significantly from NMR applications, which have been pivotal in evaluating fluid recovery performance. HnP involves injecting gas (e.g., CO_2 or natural gas) into a well, allowing it to diffuse into the tight rock matrix during a soaking phase, and then reopening the well for production. Over the past decade, CO_2 and natural gas HnP EOR methods have shown notable success in liquid-rich shale reservoirs, such as the Eagle Ford, achieving incremental recovery factors of 30–70% beyond primary production (Rassenfoss 2017).

Studies by Min et al. (2020) revealed that recovery increased substantially when injection pressures exceeded the minimum miscibility pressure (MMP), with NMR T_2 spectra showing the preferential mobilization of lighter hydrocarbons and superior performance of ethane-rich gas mixtures **(Figure 1.7**). The study also demonstrated that rocks with higher surface area-to-volume ratios achieve greater recovery. Mamoudou et al. (2020) showed that soaking time alone does not

control recovery; rather, the residence time (a combination of injection, soaking, and production phases) is a factor that must be optimized to improve recovery.

Later, Dang (2019) work using real-time NMR identified diffusion as a dominant recovery mechanism. He observed that fluid recovery follows the same trend during injection, soaking (no differential pressure), and the production phases. **(Figure 1.8).**

Together, these findings underscore the versatility and critical importance of NMR in advancing our understanding of fluid transport and storage processes in unconventional reservoirs.

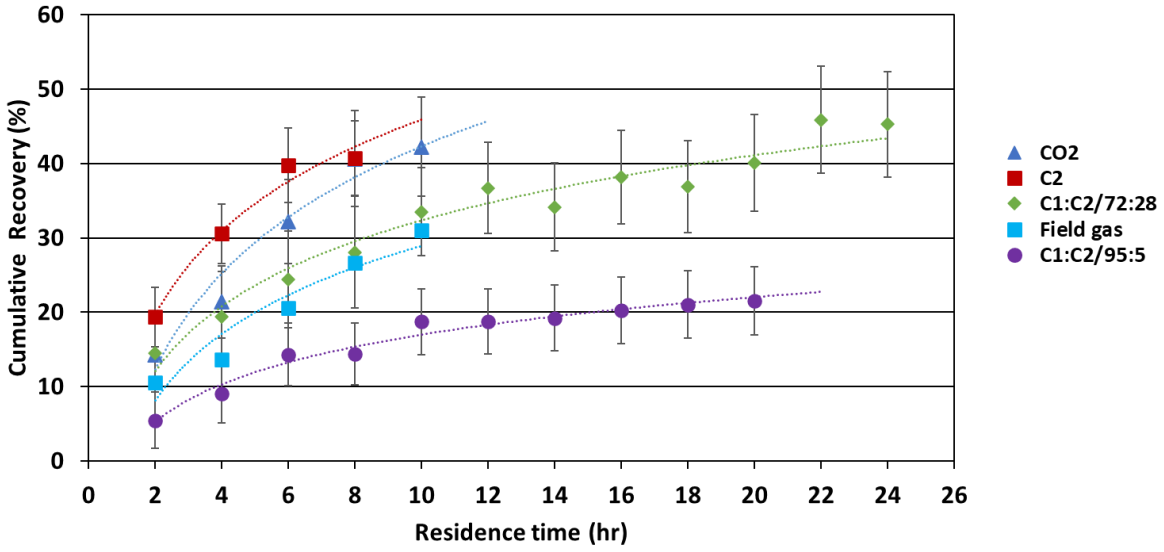


Figure 1.7 - NMR application in EOR Huff-n-Puff optimization highlighting the impact of gas composition in Eagle Ford shale. The study demonstrates solvent performance, with ethane and CO_2 identified as the most effective solvents for this shale (Min et al. 2020).

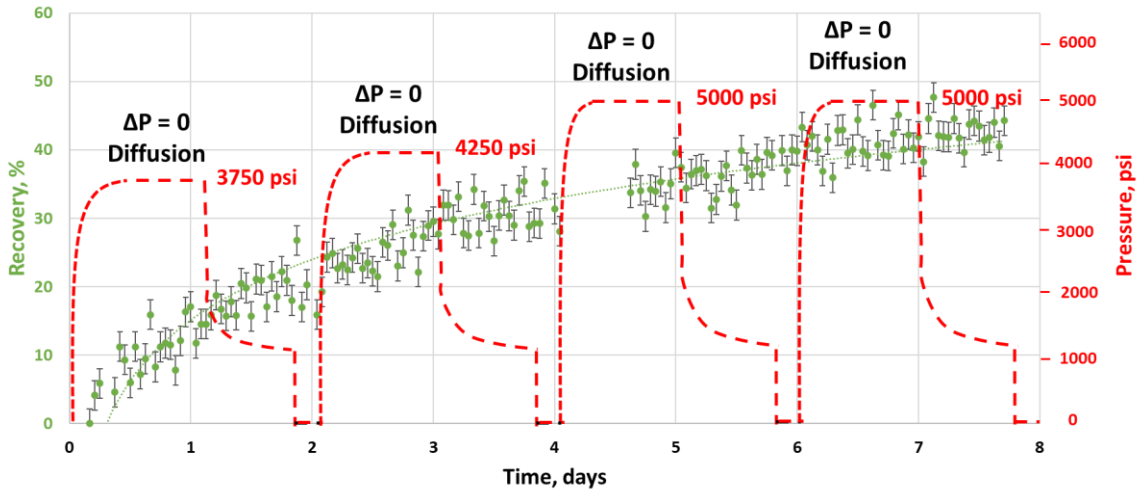


Figure 1.8 - Real-time NMR recovery in a shale plug highlighting the impact of diffusion. The recovery during injection phases follows a similar trend to recovery during production phases, suggesting that diffusion plays a dominant role in Huff-n-Puff recovery, as opposed to convective flows (Dang 2019).

1.4 Energy transition a new NMR opportunity

Carbon capture and storage is a crucial technology for mitigating greenhouse gas emissions, a primary driver of global warming (NASA 2023). Potential CO_2 geostorage sites include deep saline aquifers, depleted oil and gas reservoirs, unmineable coal seams, basalt formations, and salt caverns (NETL 2023). Among these, deep saline reservoirs—porous formations saturated with brine beneath a shale caprock—are considered one of the most viable options due to their abundance, high storage capacity, and injectivity (Miocic et al. 2023). However, uncertainties remain regarding long-term reservoir and caprock stability (Luo et al. 2022). Recent studies (Adriao Cruz 2023) highlighted the potential of NMR in evaluating caprock integrity by analyzing changes in diffusional tortuosity of shale caprock before and after exposure to supercritical CO_2. After two weeks of contact, only minor alterations in tortuosity were observed, demonstrating NMR's capability for CCS application.

Ensuring CCS safety and efficiency requires addressing challenges such as induced seismicity, containment stability, and chemical interactions between CO_2, reservoir rocks, caprock, and cement (Al Hameli et al. 2022).

Underground hydrogen storage (UHS) is another emerging strategy to balance renewable energy intermittency and meet peak demand (Gabrielli et al. 2020). While extensive research exists on CO_2 geosequestration (van der Meer et al. 2009, Bachu 2015, Al Hameli et al. 2022), studies specifically investigating H_2-brine-rock interactions and their impact on reservoir integrity remain limited (Heinemann et al. 2021). Hydrogen's low density and viscosity increase buoyancy and migration risks, while its high diffusion coefficient increases potential leakage (Hassanpouryouzband et al. 2020). Additionally, interactions between injected hydrogen and formation brine can trigger physicochemical and microbial reactions, altering key petrophysical properties such as permeability, porosity, and wettability (Flesch et al. 2018, Amigáň et al. 1990, Hemme and Van Berk 2018, Panfilov 2010). These changes, along with the potential for microfracture reactivation or propagation, significantly influence the long-term stability of hydrogen storage (Henkel et al. 2014, Zivar et al. 2021, Heinemann et al. 2021, Hassanpouryouzband et al. 2022)

Recent work from Ho et al (2024) has shown that NMR can also be used to study the hydrogen storage mechanism in dried sandstone. Adding a new application for NMR.

1.5 Objectives of this study.

NMR has proven to be a powerful tool for characterizing reservoir properties and fluid behavior, with significant applications in EOR, and potential in CCS, and UHS. This study builds on previous research to further leverage NMR's capabilities. In EOR applications, NMR is utilized to

enhance fluid (water/oil) quantification during production on preserved samples and later cleaned samples for pressure stepped saturation, providing insights into the impact of pore connectivity on overall recovery. For CCS, NMR is employed to assess the effects of supercritical CO_2 impact on Class G cement integrity, specifically for repurposing legacy oil and gas wells for CO_2 storage, with a focus on potential changes in tortuosity under storage conditions. Finally, NMR is used to investigate hydrogen storage mechanisms in bulk fluids and porous media, including partially saturated sandstones and shales at high pressure.

1.6 Outline of the dissertation

This dissertation consists of 6 chapters, each leveraging the capabilities of NMR in EOR, CCS, and UHS. Each chapter corresponds to a standalone publication or a manuscript under review:

Chapter 2: NMR Application for Improved Recovery Characterization During EOR Huff-n-Puff.

Chapter 3: Experimental Evaluation of Cement Integrity on Exposure to Supercritical CO_2 Using NMR: Application to Geostorage. (Mamoudou et al. 2024) https://www.cell.com/heliyon/fulltext/S2405-8440(24)00175-0

Chapter 4: Hydrogen Interaction in Bulk Fluids for Geological Storage Applications Using NMR.

Chapter 5: Hydrogen Interaction in Cyclohexane Using NMR for Geostorage Application

Chapter 6: Evaluation of Hydrogen Storage in Partially Saturated Sandstone and Shales. (Mamoudou et al. 2025) https://www.sciencedirect.com/science/article/pii/S2949821X25000614

Chapter 2: NMR Application for Improved Recovery Characterization During EOR Huff-n-Puff.

2.1 Abstract

This study presents an integrated NMR-based approach for quantifying oil and water recovery during EOR by gas huff-n-Puff in tight shale formations. Low-field NMR, employing both T_2 relaxation and T_1-T_2 mapping, was used to separately monitor oil and water production and to characterize fluid mobilization within the rock matrix. Pressure-stepped saturation experiments with brine and dodecane provided additional insight into pore accessibility and predicted production profiles. Experiments were conducted on preserved Eagle Ford and Wolfcamp shale core samples using a C_1:C_2 (72:28) gas mixture at 4000 psi and 150°F. Results show that oil production in both formations is primarily driven by the vaporization of lighter hydrocarbons (below C_{13}), while water production is controlled by wettability and pore connectivity. The Eagle Ford formation exhibited continuous oil production (25% recovery) and moderate water recovery (15%), attributed to its well-connected organic pore network (Type 2 connectivity). In contrast, the Wolfcamp formation, characterized by high clay content and Type 3 serial flow connectivity, showed limited oil recovery (10%) and higher water recovery (27%), with episodic water breakthrough after early oil production. These findings highlight the critical role of pore structure and connectivity in governing recovery behavior and underscore the need to tailor EOR strategies to specific reservoir characteristics. The results also suggest that C_1:C_2 gas mixtures are best suited for liquid-rich shales with lighter hydrocarbons and lower clay content (<15wt%), where vaporization-driven recovery is favored.

2.2 Introduction

EOR techniques, such as gas HnP, offer significant potential for increasing shale oil recovery, with reported improvements ranging from 30 to 70% (Thomas et al. 2016, Hoffman 2018). The HnP process involves injecting miscible gas into a formation to release hydrocarbons. The gas diffuses into the rock matrix at the matrix-fracture interface (Fragoso et al. 2015, Sheng 2017). This diffusion causes the oil to swell and reduces its viscosity, mobilizing it from the rock pores into the fractures (Hawthorne et al. 2017).

Extensive laboratory and simulation studies have investigated the impact of various factors on recovery in conventional rocks, such as soaking time and the number of cycles (Yu et al. 2016, Wang et al. 2010), solvent composition (Hawthorne et al. 2017, Li et al. 2017), sample size (Li and Sheng 2016), injection pressure (Qazvini and Torabi 2012), and other variables. However, tight rock samples pose unique challenges due to their small pore volumes, which make recovery measurements from effluent collection impractical. Monitoring the fluid remaining within the rock matrix provides a viable alternative.

Laboratory NMR has been extensively used to evaluate HnP performance in shale formations, typically using preserved samples (Min et al. 2020, Mamoudou et al. 2020, Mamoudou et al. 2021, Sondergeld et al. 2022, Dang, Mamoudou, et al. 2023). However, most studies have relied on oil re-saturated samples to measure cumulative recovery, failing to account for the effects of in-situ formation brine. This limitation often results in overestimating oil recovery.

To address these challenges, we propose using low-field NMR techniques, including T_2 relaxation distribution, T_1-T_2 mapping, and a subtraction method, to separately quantify oil and water recovery during each HnP cycle in preserved tight formations. This approach enables direct

monitoring of fluid behavior within the rock matrix, providing a more accurate assessment of incremental oil and water recovery. Sequential pressure saturation in brine and dodecane on twin samples was also used to determine organic and inorganic pores connectivity of the samples.

Our study focuses on the Eagle Ford and Wolfcamp shales as a case study to evaluate the effectiveness of this methodology and its potential to improve recovery characterization during HnP processes.

2.2 Methods

2.2.1 Sample description

Preserved 1.5-inch-long core plugs from the Eagle Ford and Wolfcamp formations were used, with their petrophysical properties detailed in **Table 2.1**. Mercury injection capillary pressure (MICP) and isothermal nitrogen adsorption were used to determine pore throat and pore body size distribution on the dried samples, as seen in **Figure 2.1**. MICP results show pore sizes below 10 nm for both samples, indicating tight formations, with Wolfcamp exhibiting a higher proportion of smaller pore throats. Nitrogen adsorption further confirms a greater volume of nanopores in the Wolfcamp sample compared to Eagle Ford.

Table 2.1 - Eagle Ford and Wolfcamp sample description. Liquid-filled porosity and the oil saturation were measured with NMR (T_2 and T_1-T_2 maps) on the samples in the "as-received state." TOC was measured using a LECO instrument, and the mineralogy was based on transmission Fourier transform infrared spectroscopy (FTIR) (Sondergeld and Rai 1994).

	Liquid Filled Porosity (%)	As Received Oil Sat (%)	TOC (wt.%)	Total Clays (wt.%)	Total Carbonates (wt.%)	Quartz+Feldspar (wt.%)	Others (wt.%)
Eagle Ford	5	70	6	16	63	13	8
Wolfcamp	4	45	7	43	0	42	15

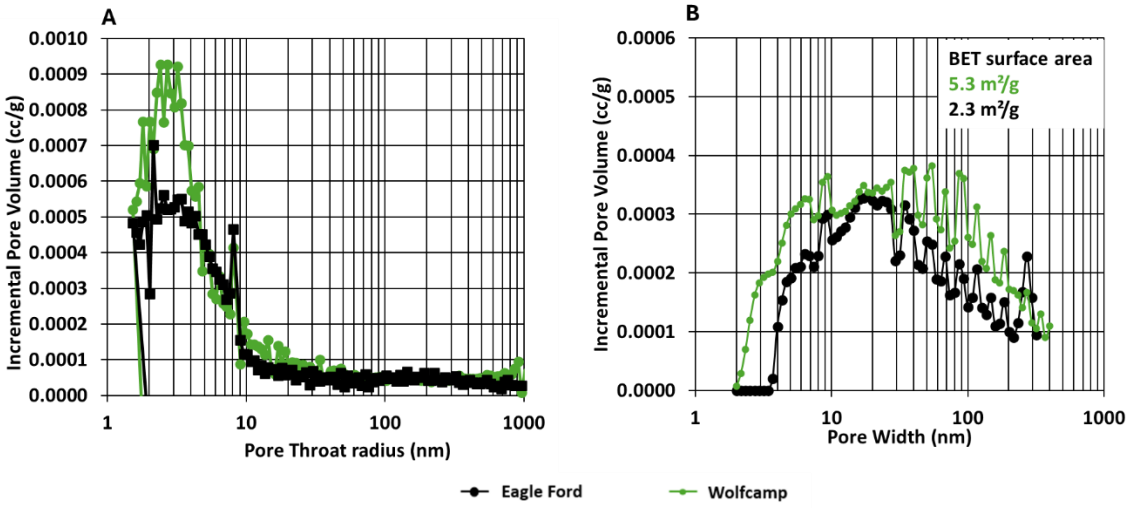


Figure 2.1 - Pore throat (A) and pore body (B) size distributions of dry Eagle Ford and Wolfcamp samples. Pore throat sizes were determined using MICP, while pore body sizes were derived from nitrogen adsorption data analyzed via density functional theory with a slit-shaped pore model. The surface area was calculated using the Brunauer-Emmett-Teller (BET) theory (Brunauer et al. 1938). MICP results show pore sizes below 10 nm for both samples, indicating tight formations. Nitrogen adsorption further confirms a greater volume of nanopores in the Wolfcamp sample compared to Eagle Ford.

HAWK® pyrolysis was also used to assess the hydrocarbon fractions present in rock samples in as-received state **(Figure 2.2).** Hydrocarbon analyzer with kinetic (HAWK) consists of breaking down the traditional S1 peak in dry pyrolysis into 4 distinct peaks through a controlled stepwise temperature increase. These sub-peaks S11-S14 represent various in-situ fractions of oil present in the shale rock, spanning from lighter, more mobile components below C_{13} (S11) to heavier components ranging from C_{21} to C_{30} (S14) (Abrams et al. 2017). The result indicates that the Eagle Ford sample is richer in hydrocarbons, particularly in lighter components S11, than the Wolfcamp sample. Earlier work on crushed shales has shown that C_1:C_2 (72:28) is efficient at vaporizing lighter components S11 but inefficient for heavier hydrocarbons such as S13 and S14 (Min et al. 2020, Mamoudou et al. 2020).

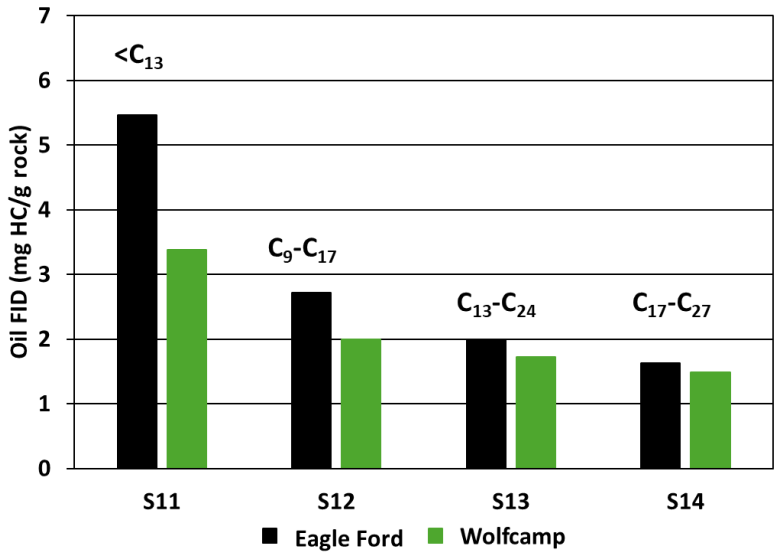


Figure 2.2 - HAWK® modified dry pyrolysis technique for hydrocarbon potential assessment. S1 dry pyrolysis is broken down into 4 peaks (S11-S14). The results indicate that the Eagle Ford sample has higher hydrocarbon content (particularly in light hydrocarbons, $<C_{13}$) compared to Wolfcamp.

2.2.2 Experimental procedure

A series of injections, soaking, and production cycles were conducted to simulate field HnP in the laboratory. The experiments used a methane-ethane mixture (72:28 %) at 4000 psi and 150°F. Each cycle consisted of a 5-hour soaking period, followed by 3 hours of production (drawdown to ambient pressure).

The experimental setup **(Figure 2.3)** included a high-pressure/high-temperature cell, rated for up to 6000 psi at 200°F (93°C) and housed inside an oven. A Teledyne ISCO model 100DM syringe pump (rated to 10000 psi), controlled by a Teledyne ISCO D-Series pump controller supplied pressure.

The experiments were conducted on wax-preserved samples, so no re-saturation with crude oil was done. A 12 MHz Oxford GeoSpec™ spectrometer (TE = 114 µs), equipped with Green Imaging Technology acquisition and processing software, was used to monitor the hydrocarbon

and water content in the core plugs before and after each cycle. For each sample, the signal-to-noise ratio (SNR) before injection was greater than 50, ensuring reliable signal detection and resolution. The minimum miscibility pressure (MMP) for the gas mixture and the associated dead oil were determined using the vanishing interfacial tension technique (Hawthorne et al. 2016). The experiments were conducted at 150°F and 4000 psi, exceeding MMP by 1000 psi.

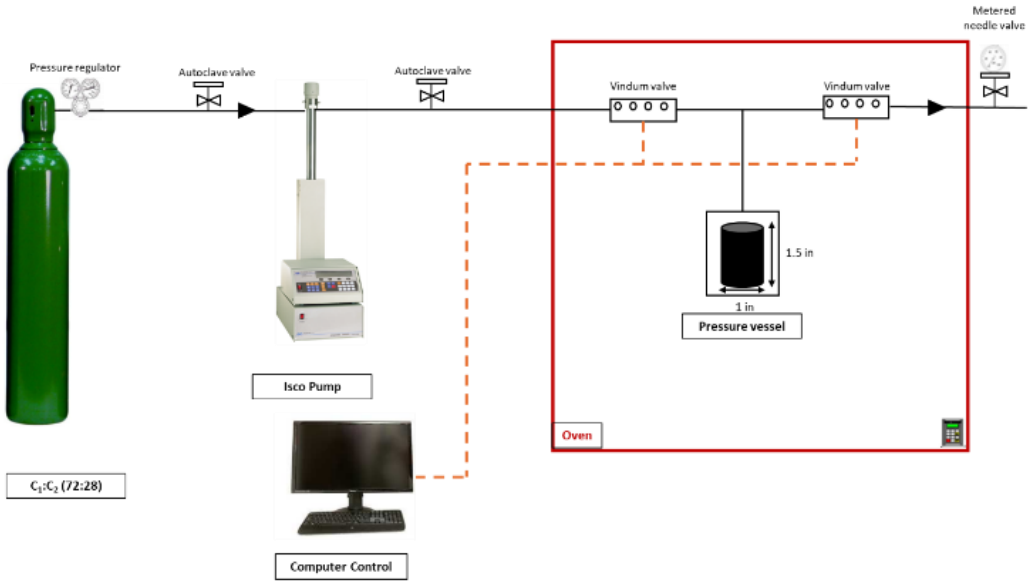


Figure 2.3 - Huff-n-Puff experimental schematic. The sample is placed inside a high-pressure cell located within an oven. A mixture of C_1:C_2 (72:28) is injected into the high-pressure cell via a pump station with precise pressure control; the pressure vessel outlet has a production choke to control the production rate and time.

2.2.3 NMR methods

T_2 relaxation was used to monitor the total pore fluid volume expelled (produced) by comparing pre-and post-NMR distributions of the remaining fluid in an Eagle Ford shale sample after one HnP cycle (5-hour soak, 3-hour production) with the C_1:C_2 (72:28) mixture. The pre- and post-EOR NMR decay curves were subtracted, and the resulting decay curve was inverted using Green Imaging Software to obtain the T_2 distribution and determine the total fluid produced volume. For each subtraction, the resultant decay data was checked to ensure no negative value of the free induction decay.

Figure 2.4 shows the results of NMR T_2 relaxation measurements, which quantify total produced fluid (water and oil) in the Eagle Ford sample after a single cycle. The fluid volume produced, calculated as the difference between pre- and post-injection NMR measurements, is approximately 0.23 cc. Following gas injection, the signal amplitude decreased significantly at two distinct peaks, below and above 1 ms. This bimodal distribution suggests that gas-displaced fluids originated from two different pore sizes or from pores having different surface relaxivities (Tinni 2015).

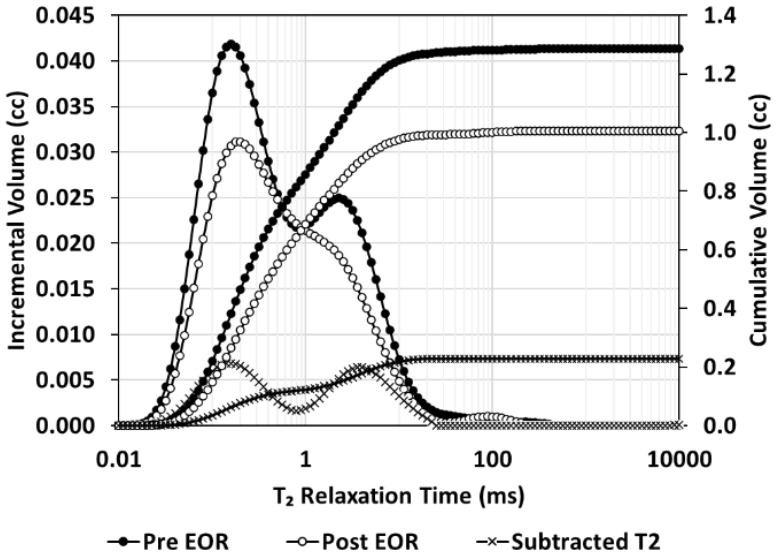


Figure 2.4 - NMR T_2 distribution of an Eagle Ford sample before and after a single injection cycle (5-hour soak, 3-hour production) with a C_1:C_2 (72:28) gas mixture at 150°F and 4000 psi. The results show a 0.23 cc fluid volume reduction after injection. The pre- and post-EOR decay curves were subtracted, and the resulting decay curve was inverted using Green Imaging Software to obtain the T_2 distribution and determine the total fluid produced volume.

To quantify the amount of oil and water produced separately, 2D T_1-T_2 maps were generated by subtracting the pre-injection map from the post-injection map, as shown in **Figure 2.5.** T_1-T_2 maps are used to differentiate fluid types based on T_1/T_2 ratios (Tinni et al. 2015, Fleury and Romero-Sarmiento 2016, Kausik et al. 2016). Earlier studies by Tinni et al (2014) showed that saturated shales with 2.5% brine have T_1/T_2 ratios between 1-1.5, while dodecane oil-saturated shales have

a higher T_1/T_2 ratio close to 2-6, and heavier hydrocarbons (e.g., waxes) can have $T_1/T_2 > 15$ in shales.

More recently, Dang (2023), showed that in clays such as Na-Montmorillonite, tested at higher NMR frequency of 23 MHz, the water signal located near 1:1 line includes contributions from both interlayer water and structural hydroxyls. In this thesis, this signal will be referred to as bound water.

Following this classification, Figure 2.5A and Figure 2.5B present the T_1-T_2 maps before and after gas injection, respectively, revealing three distinct signals based on T_1/T_2 ratios: bound water ($T_1/T_2 \approx 1$), free water ($T_1/T_2 \approx 10$), and hydrocarbons, which exhibit an elongated shape due to the presence of various alkanes ($T_1/T_2 \geq 10$). After subtraction (Figure 2.5C), only the free water and hydrocarbon signals remain, confirming that these fluids were produced during the single injection cycle.

By integrating the results of T_2 relaxation and T_1-T_2 maps in Figure 2.4 and Figure 2.5C, the individual contributions of water and oil production can be quantified using the T_1/T_2 cut-off (Tinni et al. 2014), as illustrated in **Figure 2.6**. The analysis indicates that approximately 0.12 ± 0.02 cc of oil and 0.11± 0.02 cc of water were produced during this cycle.

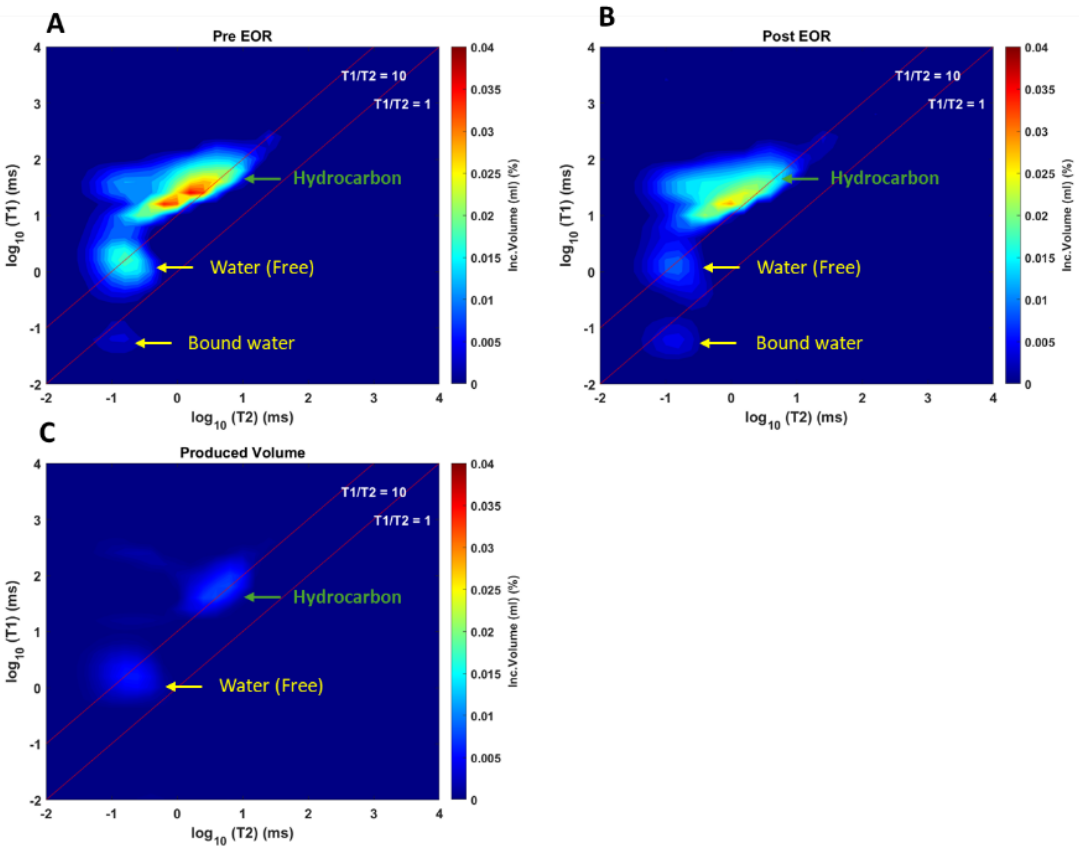


Figure 2.5 - 2D T_1-T_2 maps used for fluid characterization of the data in Figure 2.4. After subtraction of the pre (A) and post (B) injection maps, the amplitude of both the water and hydrocarbon signals was reduced, but the bound water signal (interlayer water and structural hydroxyl) stays the same. (C). Note: All three figures are plotted on the same scale, and SNR>45 was achieved pre- and post-EOR. However, the produced volume (i.e., subtracted) SNR ranged from 10-15 due to the small amount of fluid produced.

The pore sizes associated with fluid production provide further insight into displacement behavior. In the Eagle Ford, water was primarily produced from smaller pores (T_2<1 ms), while oil originated from larger pores (T_2 >1 ms), aligning with the bimodal T_2 distribution observed in Figure 2.4.

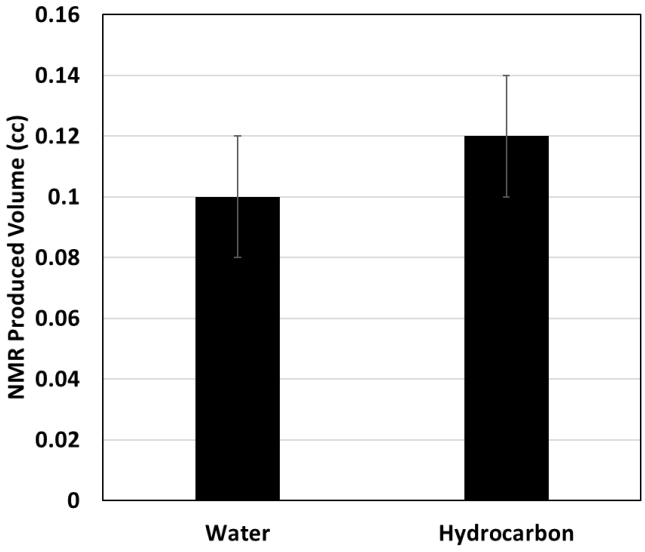


Figure 2.6 - NMR produced volumes of water and hydrocarbon calculated by integrating T_1-T_2 maps and T_2 relaxation data after one gas injection cycle with a mixture of C_1:C_2 (72:28).

2.3 Results

2.3.1 Fluid Recovery

Following the methodology outlined earlier and the classification proposed by Tinni et al. (2014), the cumulative recovery of water and oil for the Eagle Ford and Wolfcamp samples is plotted in **Figure 2.7** and **Figure 2.8**. For Eagle Ford shale, the oil recovery is higher than water recovery. After three cycles, water recovery plateaus at approximately 15%, while oil recovery continues to increase, reaching 25% after six cycles. In contrast, the Wolfcamp sample, characterized by high initial water saturation and significant clay content (Table 2.1), exhibits the opposite trend. After seven cycles, oil recovery is only 10%, whereas water recovery reaches 27%. Oil production in Wolfcamp progresses gradually and monotonically, while water production is intermittent. Notably, most water production occurs during cycles 3 and 6. Finally, under our test conditions, only free water was produced in both samples.

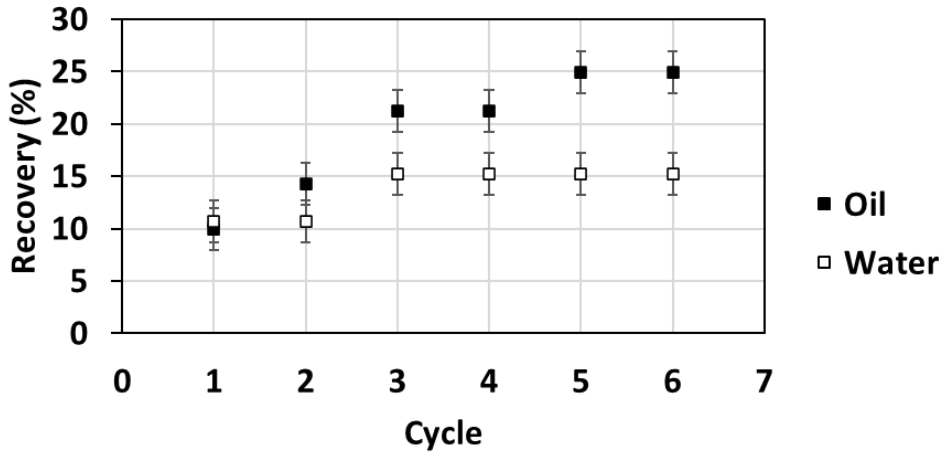


Figure 2.7 - Oil and water recovery for the Eagle Ford sample, shows oil recovery increasing to 25% after six cycles, while water recovery plateaus at 15% after three cycles.

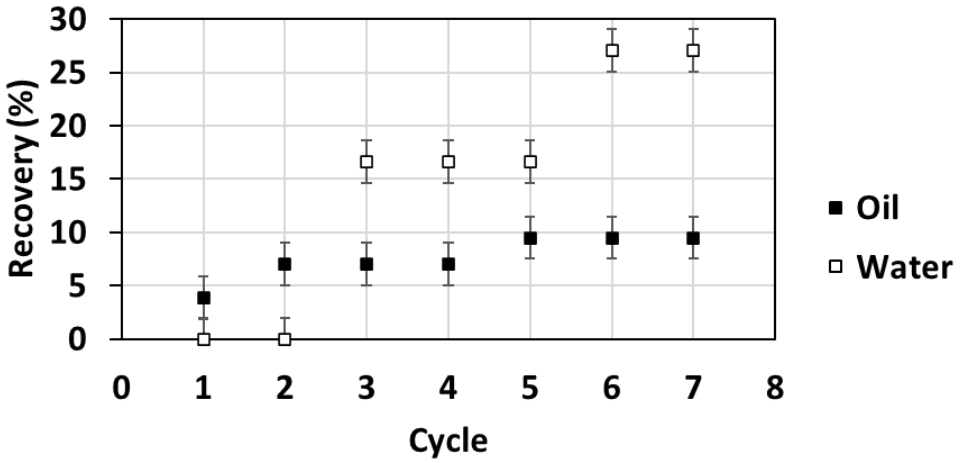


Figure 2.8 - Oil and water recovery for the Wolfcamp sample, with water recovery reaching 27% and oil recovery limited to 10% after seven cycles, reflecting its high-water saturation and clay content.

To further interpret the cumulative recovery trends shown in the previous graphs, the data were also expressed in terms of a Water–Oil Ratio (WOR), a metric commonly used in field operations to evaluate the relative contribution of water and oil in produced fluids.

Figure 2.9 shows the WOR derived from the cumulative NMR recovery measurements for both samples. In the Eagle Ford experiments, the WOR begins at approximately 0.94 during the first cycle and increases progressively to around 1.6 by the sixth cycle. This progression indicates that

although water production increases over successive cycles, oil remains a substantial component of the total produced fluids throughout the test. In the Wolfcamp experiments, the WOR is zero for the first two cycles, indicating no measurable water production, and then increases sharply to approximately 2.4 by the third cycle. Thereafter, WOR remains elevated, ranging between 2.4 and 2.9 through the subsequent cycles. These data demonstrate a transition toward water-dominated production in the Wolfcamp sample after the initial cycles.

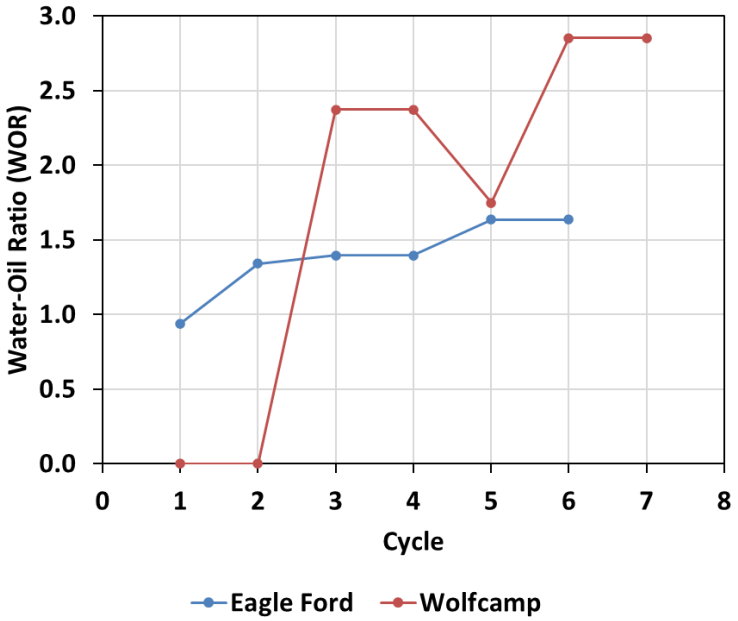


Figure 2.9 - Water–Oil Ratio (WOR) versus Huff-n-Puff cycle for Eagle Ford and Wolfcamp samples. Eagle Ford shows a gradual increase in WOR, while Wolfcamp transitions rapidly to water-dominated production after cycle 2.

These recovery profiles highlight the contrasting production behavior between the two formations under identical solvent and pressure conditions. To place these results in the context of previous work, the cumulative recovery from this study was compared with published recovery factors obtained using similar solvents on Eagle Ford samples.

The cumulative recovery obtained in this study on preserved Eagle Ford plugs after three cycles (approximately 24 hours of residence time) was 36% (oil recovery of 15% and water recovery of

21%). This total recovery is approximately 10% lower than the 45% reported by Min et al (2020) for Eagle Ford samples subjected to the same solvent composition under comparable pressure and temperature conditions. The difference can be attributed to sample preparation and accessible surface area, as Min et al.'s (2020) experiments were conducted on crushed material, which offers significantly greater surface area and shorter diffusion paths than intact plugs. In contrast, plug samples preserve pore connectivity and tortuosity, leading to slower fluid exchange and reduced recovery despite the same solvent. Furthermore, previous work by Dang (2023) has shown that confinement itself can reduce recovery in shales, from 30% to 5%, by closing microfractures and reducing the effective surface-area-to-volume ratio available to the injected gas. These observations highlight not only the influence of sample geometry but also the importance of conducting recovery measurements on plug samples under reservoir-representative stress conditions to accurately capture the effects of pore structure and confinement on EOR performance.

Building on these recovery comparisons, further insight into the fluid behavior and rock properties can be obtained by examining the hydrocarbon characterization, pore size distribution, and connectivity, as discussed in the following sections.

2.3.2 Hydrocarbon Characterization

Hawk® analysis was conducted on separate crushed Eagle Ford and Wolfcamp samples (6-7 mm particle sizes) to characterize the hydrocarbons produced during EOR, as shown in **Figures 2.10** and **2.11**. The results indicate preferential vaporization of lighter hydrocarbons (S11 and S12) in both samples. Similar observations were reported by Min et al. (2020) and Mamoudou et al. (2022) in other formations using the same solvent gas. Molecular simulations by Perez and Devegowda (2020) on black oil using a C_1:C_2 (72:28) mixture at the same injection pressure and temperature,

as shown in **Figure 2.12**, further confirm the preferential vaporization of lighter components, such as methane and intermediate hydrocarbons. Additionally, the same figure demonstrates that there is no observed reactivity with heavier hydrocarbons, such as asphaltenes and aromatic species.

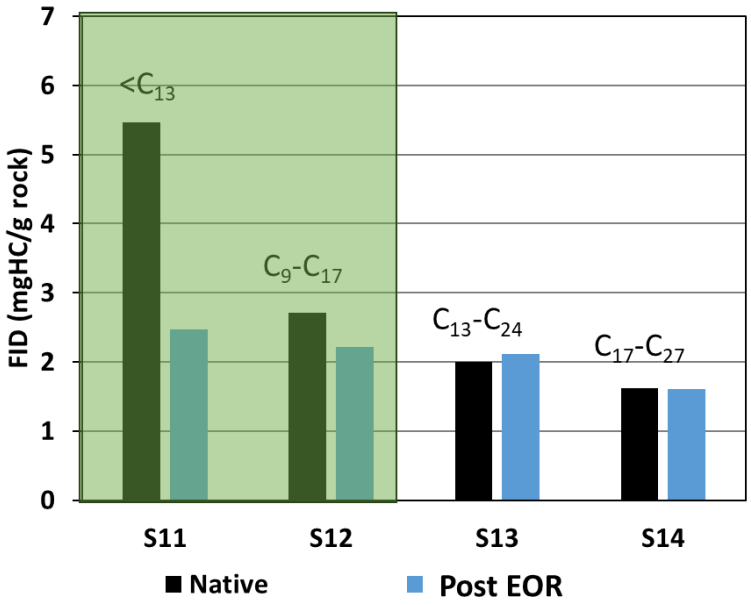


Figure 2.10 - HAWK® analysis on Eagle Ford crushed sample pre and post EOR showing preferential vaporization of lighter hydrocarbons S11 and S12.

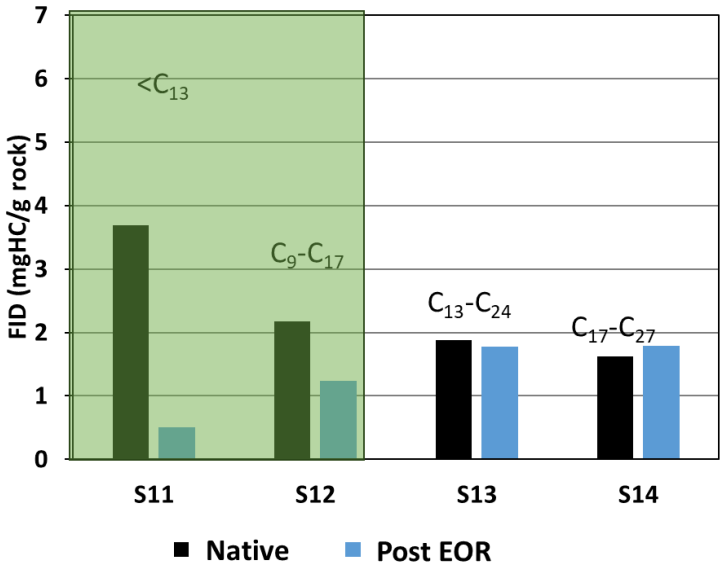


Figure 2.11 - HAWK® analysis on Wolfcamp crushed sample pre and post EOR showing preferential vaporization of lighter hydrocarbons S11 and S12.

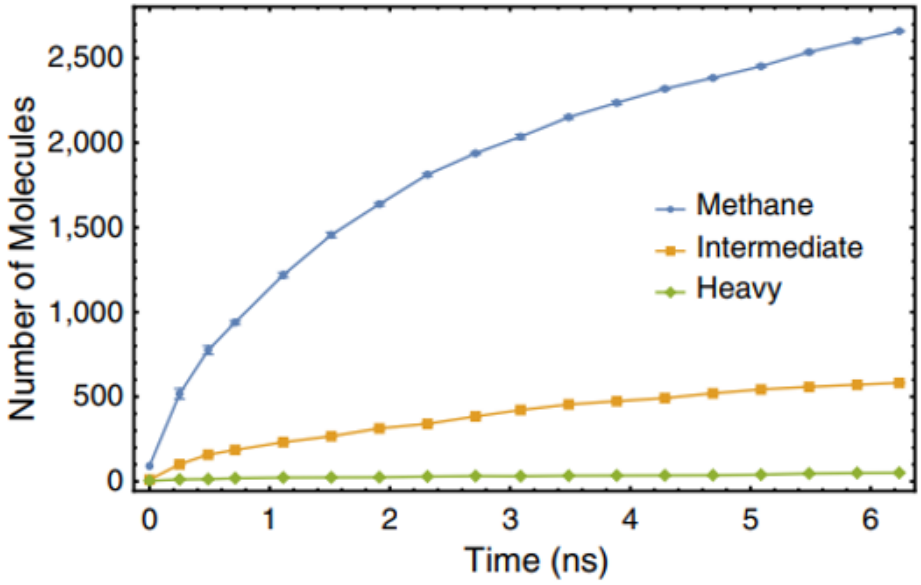


Figure 2.12 - Evolution of the produced fluids over time using molecular simulation after 6ns using C_1:C_2 (72:28) in black oil nanopores showing preferential vaporization of the methane and intermediate species (Perez and Devegowda 2020)

2.3.3 Pore Size

Following the previous methodology, **Figure 2.13** and **Figure 2.14** show the produced T_2 distribution as a function of cycles. Figure 2.13 presents the Eagle Ford sample data. The results indicate that most production occurs from pores with $T_2 > 1$ ms, except for cycle 1, suggesting that fluid primarily originates from larger pores. For the Wolfcamp sample (Figure 2.14), fluid production is predominantly from small pores ($T_2 < 1$ ms). This is especially evident during cycles 3 and 6, where significant volumes of water were produced: 17% and 10%, respectively.

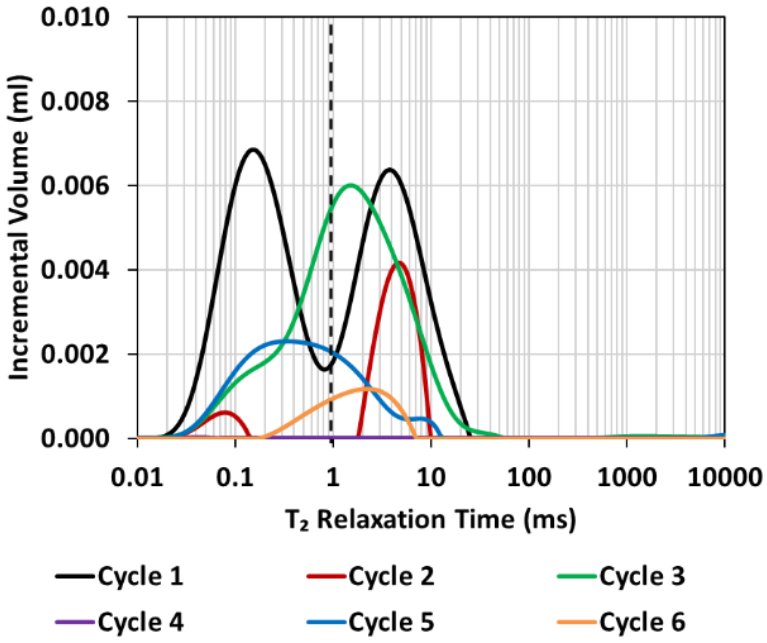


Figure 2.13 - NMR T_2 relaxation obtained from the subtracted signal showing the produced volume as a function of cycles in Eagle Ford. Most fluid production originates from T_2 >1 ms (i.e., large pores).

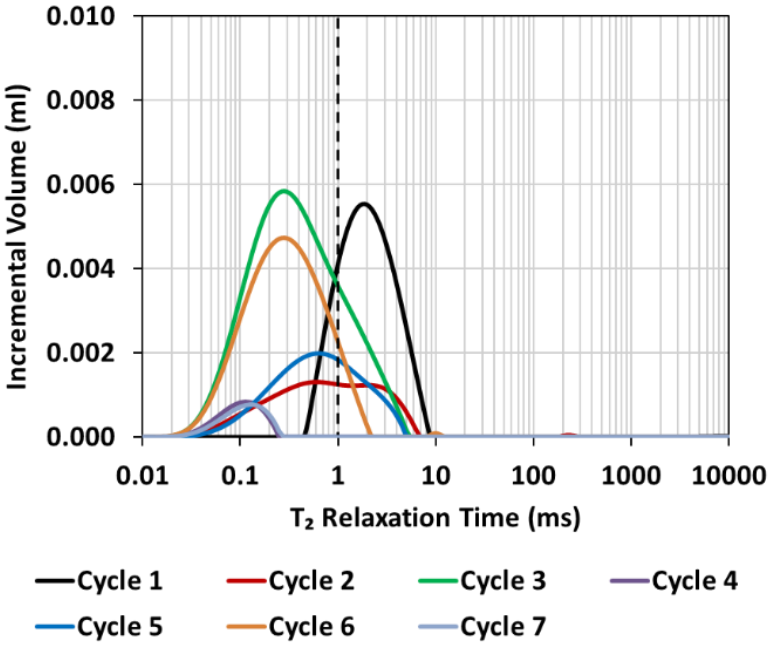


Figure 2.14 - NMR T_2 relaxation obtained from the subtracted signal showing the produced volume as a function of cycles in Wolfcamp. The results indicate that most fluid production originates from T_2 <1 ms pores (i.e., small pores) except for cycle 1.

2.3.4 Pore Connectivity

After EOR, it was important to assess the pore connectivity of the samples, particularly in relation to the water displacement mechanism. In shale formations, the pore network is typically composed of water-wet, oil-wet, and mixed-wet pores (Loucks et al. 2011, Curtis et al. 2012). While MICP is commonly used to estimate pore throat sizes and infer connectivity, it cannot distinguish between organic and inorganic pore types (Curtis et al. 2011).

Pressure-stepped saturation experiments up to 5000 psi were conducted to better evaluate organic and inorganic pore throat connectivity using 2.5% KCl brine and dodecane on twin samples from the same formations.

Analogue samples from the Eagle Ford and Wolfcamp formations (labelled Eagle Ford 2 and Wolfcamp 2) were used for these tests; they shared similar mineralogy with the EOR preserved samples, but Wolfcamp 2 had a lower TOC of 3.3 wt% (**Table 2.2**).

Table 2.2 - Eagle Ford and Wolfcamp samples used for EOR (white color) and pressure stepped saturation (yellow color). Note: For the Eagle Ford samples the dominant clay was Illite, while for the Wolfcamp samples the total clays were a combination of Illite and mixed clays.

Sample	Total Porosity (%)	TOC (wt.%)	Total Clays (wt.%)	Total Carbonates (wt.%)	Quartz+Feldspar (wt.%)	Others (wt.%)
Eagle Ford 1 (Preserved)	5.5	4.9	16	63	13	8
Wolfcamp 1 (Preserved)	5.2	4.0	43	0	42	15
Eagle Ford 2	7.6	5.3	13	75	12	0
Wolfcamp 2	5.5	3.3	47	19	33	1

The twin samples were imbibed in fluids (brine or dodecane for a week at ambient pressure, then saturated for 24 hours at increasing pressure, and NMR T_2 relaxation was used to monitor fluid

intrusion. The detailed methodology is presented by Tinni (2015). All samples were Soxhlet-cleaned using a toluene and methanol mixture (80:20) before saturation.

Figures 2.15 and **2.16** present NMR measurements as a function of pressure for brine and dodecane saturation in the Eagle Ford 2 sample.

Figure 2.15 shows a bimodal T_2 distribution during injection, similar to Figure 2.4, with signal contributions from pores below and above 1 ms. During imbibition (1–14 psi), brine invades inorganic and mixed-wet pores with relaxation times below 1 ms. As pressure increases up to 750 psi, brine continues to fill inorganic pores (T_2 < 1 ms). However, beyond 1000 psi, brine begins to invade larger organic pores with T_2 > 1 ms. Figure 2.15 indicates that organic pores account for approximately 2.4% of the pore network, while inorganic and mixed-wet pores represent about 3.6%. A pressure of around 850 psi is required for brine to connect the organic pore network.

For the Wolfcamp 2 sample shown in **Figure 2.17**, organic pores represent only about 1% of the pore network, while inorganic and mixed-wet pores make up around 3.2%. The pressure required for brine to access the organic pores is about 300 psi, which is nearly three times lower than the pressure required in Eagle Ford 2. This suggests that the entry pore throat in the organic network of Wolfcamp 2 is larger than those in Eagle Ford 2. Using the Washburn **Equation 2.1** and water as the displacing fluid, an organic pore throat radius of 70 nm can be estimated for Wolfcamp 2, against 25 nm for the Eagle Ford 2.

$$r = \frac{2\gamma cos(\theta)}{\Delta P} \qquad 2.1$$

Where r is pore radius (cm or m), γ is the interfacial tension of the displacing fluid, here water (0.072 N/m), θ is the contact angle between water and solid surface (degrees), assuming water is wetting θ=0°, and ΔP is the capillary pressure required to displace water (Pa or psi).

Additionally, the MICP data (Figure 2.1A) showed that the average pore throat size for the preserved samples was around 3 nm, which corresponds to a capillary pressure of approximately 6030 psi (assuming air–water γ and a water-wet rock θ=30°). This means that during EOR injection at 4000 psi, certain pores remain inaccessible to the gas in our test conditions.

Finally, during dodecane intrusion in both samples, the porosity remains relatively flat (**Figure 2.18**). This indicates that dodecane accesses the full pore volume during imbibition, suggesting there is no significant volume of purely inorganic water-wet pores.

Overall, pore connectivity in Eagle Ford 2 seems to be influenced by a combination of inorganic/mixed-wet and organic pores, whereas in the Wolfcamp 2 sample, connectivity seems to be primarily governed by inorganic and mixed-wet pores.

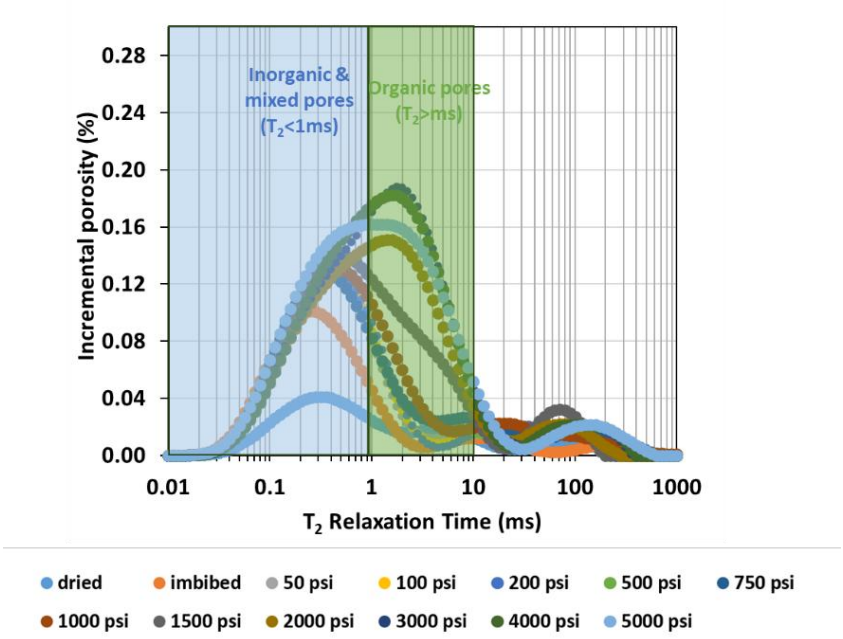


Figure 2.15 - NMR T_2 relaxation during pressure stepped saturation in Eagle Ford 2 with 2.5% KCl brine, shows initial intrusion in inorganic pores (T_2< 1 ms) up to 750 psi. After 1000 psi injection, brine starts to invade organic pores (T_2 = 1-10 ms). Note: Relaxation time around 100 ms is attributed to brine present in larger pores or cracks in the sample.

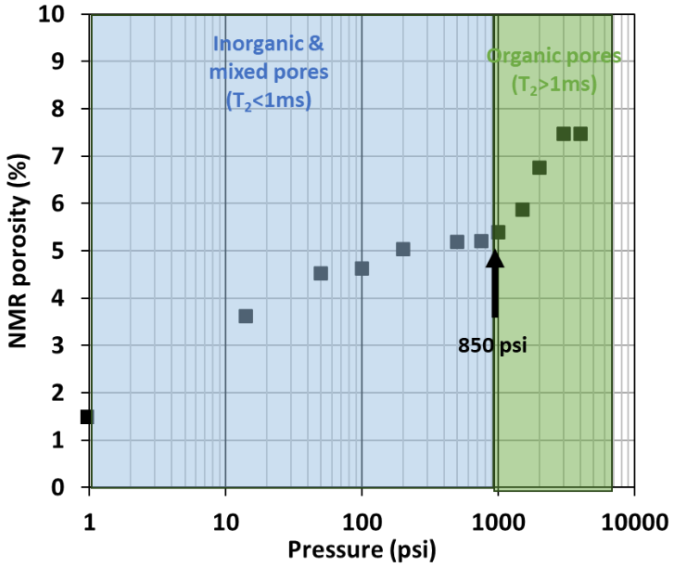


Figure 2.16 - NMR porosity of Eagle Ford 2 during pressure-stepped saturation in 2.5% KCl brine shows an inflection around 850 psi, where connection is established with organic pores. The organic porosity represents 2.4 %. Note: 1 psi corresponds to the dried state, and 14 psi corresponds to the porosity after imbibition.

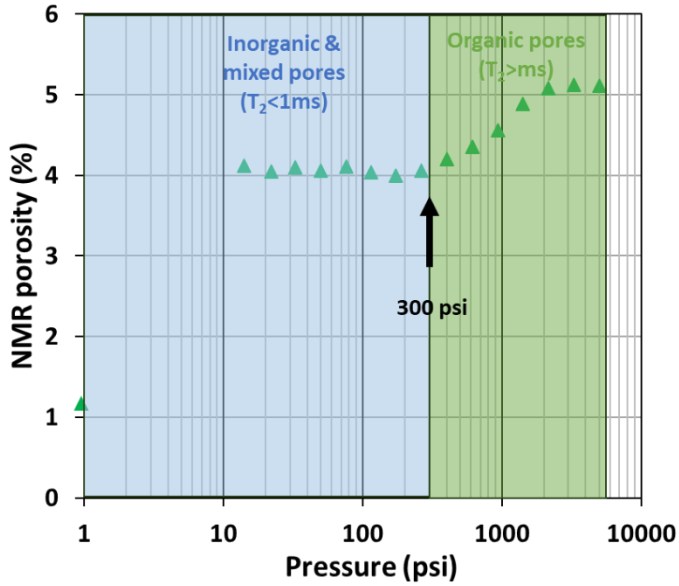


Figure 2.17 - NMR porosity of Wolfcamp 2 during pressure-stepped saturation in 2.5% KCl brine shows an inflection at 300 psi where the connection is established between inorganic and organic pores. Most connectivity is established during imbibition as brine enters inorganic and mixed wet pores.

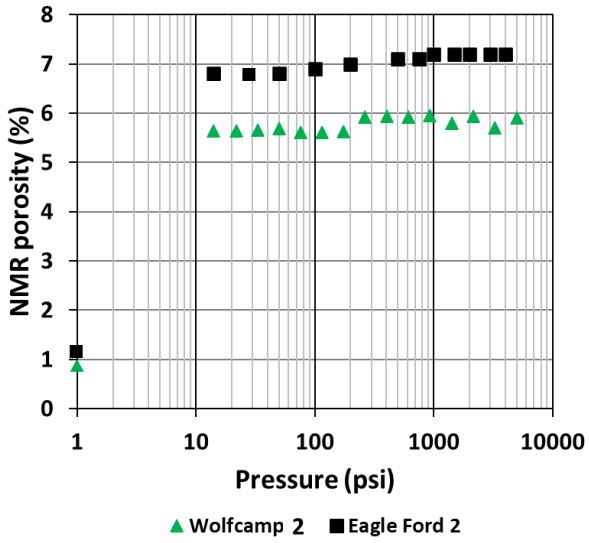


Figure 2.18 - NMR porosity as a function of pressure during dodecane saturation for Eagle Ford and Wolfcamp samples, shows flat profiles indicative of full pore access during imbibition and minimal pure inorganic wet porosity.

From an EOR perspective, the minimum pressure required to displace water is 850 psi for the Eagle Ford 2 and 300 psi for the Wolfcamp 2. This suggests that the water displacement in the Eagle Ford 2 is significantly more challenging than in Wolfcamp 2 under single-fluid conditions. In preserved samples containing dual fluids, these pressures may be even higher, and the presence of heavier hydrocarbons (Figures 2.10 and 2.11) could add additional capillary resistance.

2.4 Discussion

The results on preserved core plugs highlight significant differences in recovery behavior between the Eagle Ford and Wolfcamp formations. In both samples, oil recovery is governed by the preferential vaporization of lighter hydrocarbons (below C_{13}), leaving behind heavier species. However, water displacement is primarily influenced by the wettability characteristics and pore network of each formation. In the Eagle Ford, oil recovery originates from organic pores, resulting in 25% oil recovery after six cycles and a plateau in water recovery at 15%. In contrast, the Wolfcamp formation, with its higher clay content (40%), exhibits a different recovery profile: high

water recovery of 27% but lower oil recovery at only 10%, with most production originating from inorganic pores. NMR pressure stepped saturation data further underscore differences in pore connectivity: pore connectivity in Eagle Ford seems to be influenced by a combination of mixed-wet and organic pore throats, whereas in the Wolfcamp sample, connectivity seems to be primarily governed by mixed-wet pores. Tinni (2015) observed 3 different flow models following brine and dodecane uptake on various shales as function of TOC (**Figure 2.19**). When compared to his pore connectivity model, our results confirm that the Eagle Ford sample conforms to a Type 2 connectivity model, characterized by a well-developed pseudo-parallel organic pore network with a good parallel organic pore network, and a mixed wet pore network. Conversely, the Wolfcamp sample aligns with a Type 3 flow system, where fluid migration is dominantly controlled by the inorganic clay matrix, reflecting a serial flow connectivity.

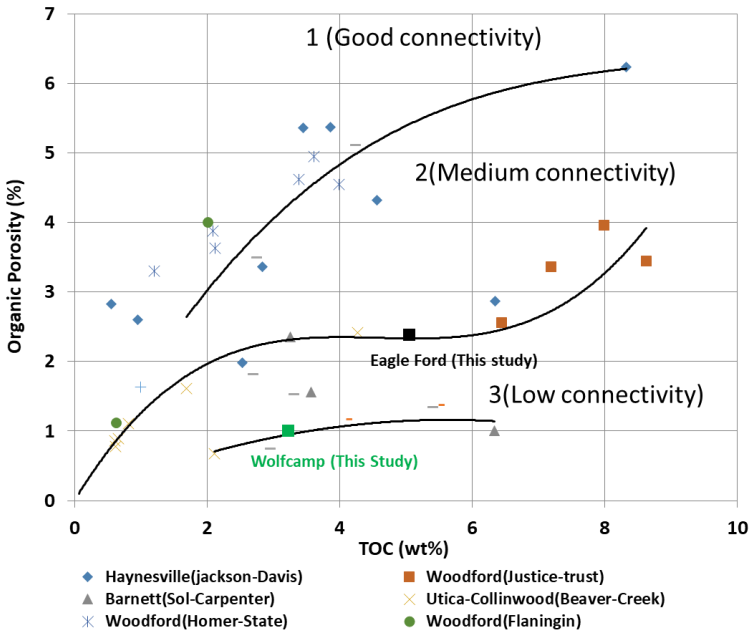


Figure 2.19 - Pore connectivity model in shales based on NMR saturation uptake using 2.5% KCl brine at 7000 psi (Tinni 2015). The Eagle Ford sample corresponds to Type 2 connectivity, characterized by an organic network with some mixed wet pore network, organized in a pseudo-parallel flow network. In contrast, the Wolfcamp aligns with Type 3 connectivity, where fluid flow is entirely controlled by the clay matrix in a serial flow configuration.

These findings highlight the need for tailored recovery strategies for each formation, with an expectation of higher water cuts in clay-rich systems like Wolfcamp. Furthermore, the incomplete recovery of fluids using the C_1:C_2 (72:28) gas mixture in both formations underscores the importance of investigating richer solvent compositions to enhance recovery efficiency and optimize production.

We propose the following model for Eagle Ford depletion during EOR (**Figure 2.20**). The rock consists of three types of pores arranged in a pseudo-parallel configuration: organic pores (black), mixed-wet pores (gray), and unconnected pores (yellow). The pore system includes large mixed-wet pore throats and small organic pore throats (Figure 2.20a). Before EOR, the organic pores were largely saturated with hydrocarbons (green), while the mixed-wet pores contained both oil and water (Figure 2.20b). During EOR, the injected gas solvent preferentially vaporizes hydrocarbons from the organic pores and incrementally displaces water. This process is facilitated by the larger pore throat size of the mixed-wet pores, resulting in a gradual and sustained production of oil and water over time (Figure 2.20 c–d). After depletion, some oil and water remain trapped in the mixed-wet and unconnected pores (Figure 2.20e).

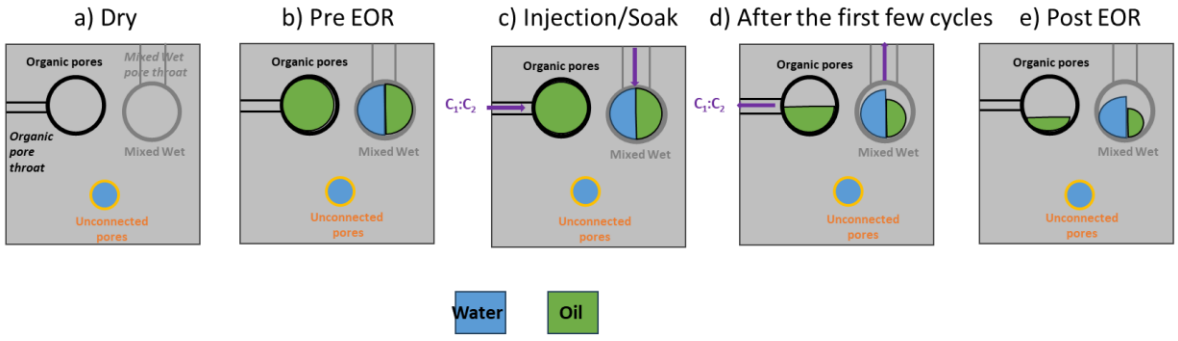


Figure 2.20 - Proposed pore connectivity and depletion model for the Eagle Ford shale during EOR. (a) The formation is characterized by a Type 2 connectivity structure with pores organized in pseudo-parallel: organic pores (black), mixed-wet pores (gray), and unconnected pores (yellow). (a)The sample is made of

large mixed wet and small organic pore throats. (b) Before EOR, hydrocarbons fill the organic pores (green), and mixed-wet pores host both fluids. (c) During early solvent injection (C_1:C_2 72:28), hydrocarbons are preferentially vaporized from the organic pores. (d) With continued injection, water is incrementally displaced from mixed wet pores, leading to sustained oil and water production over multiple cycles. (e) Following depletion, some water and oil remain trapped within mixed wet pores and unconnected pores.

In contrast, the Wolfcamp formation follows a Type 3 model, organized in series (**Figure 2.21**), where flow connectivity is dominated by mixed wet pores (Figure 2.21a). Before EOR, hydrocarbons were primarily located in large mixed-wet pores, while water was also present in smaller mixed-wet pores (Figure 2.21b). During solvent injections, vaporization of lighter hydrocarbons occurs preferentially (Figure 2.21c). However, following depletion of most hydrocarbon content after a few cycles, water is mobilized intermittently due to capillarity from mixed wet pore throats, resulting in intermittent aqueous production (Figure 2.21d). Post-EOR, most hydrocarbons have been vaporized, while some water and oil remain confined within the mixed wet pores network (Figure 2.21e).

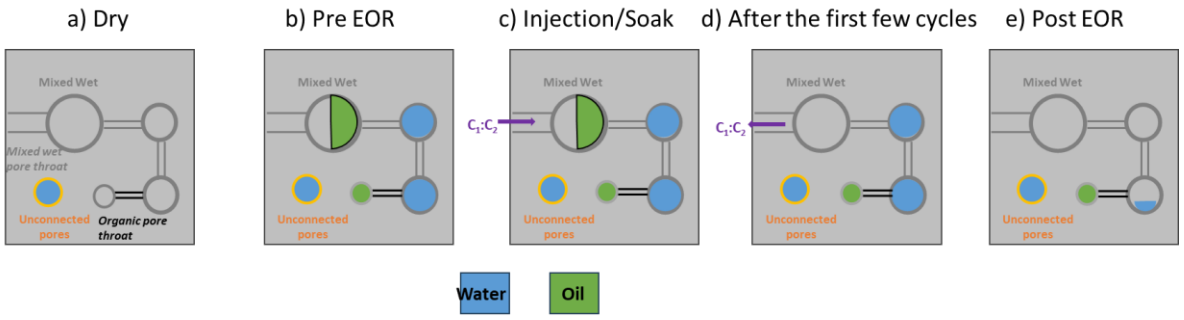


Figure 2.21 - Proposed pore connectivity and depletion model for the Wolfcamp shale during EOR. (a) This formation follows a Type 3 connectivity model with serial flow dominated by mixed wet pores (a). (b) Before EOR, larger mixed-wet pores contain hydrocarbons while smaller mixed-wet pores are water saturated c) During early solvent injection, lighter hydrocarbons are vaporized preferentially. (d) After depletion of most hydrocarbons, water is mobilized intermittently due to capillary-driven displacement from clay-bound pore throats, leading to episodic water production. (e) Post-EOR, most hydrocarbons are depleted, while some hydrocarbons remain confined within the mixed wet pore network.

2.5 Conclusion

Low-field NMR provides an effective method for quantifying oil and water recovery during the EOR process, offering detailed insights into fluid mobilization in tight shale formations. By employing T_2 relaxation and T_1-T_2 mapping on preserved plug samples, this study achieved precise separation and quantification of oil and water phases at each cycle.

Our results also show that during HnP EOR with a C_1:C_2 (72:28) gas mixture, oil recovery is primarily driven by vaporization of lighter hydrocarbons (below C_{13}), while water recovery is governed by wettability and pore connectivity. Under our test conditions, water production was limited to free water (i.e., no bound water), and with an injection pressure of 4000 psi during EOR, certain pores remain inaccessible to gas.

Additionally, pressure-stepped saturation experiments on brine-saturated samples revealed that, in both formations, pressures below 1000 psi were sufficient to establish a continuous water phase and displace water.

The Eagle Ford formation demonstrates that reservoir connectivity is primarily controlled by two networks: organic and mixed-wet pores. This dual network results in continuous oil production and moderate water recovery. In contrast, the Wolfcamp formation is dominated by mixed-wet pore connectivity. This leads to episodic water production and water breakthroughs after the initial oil release.

These contrasting behaviors emphasize the need to tailor EOR strategies to the specific characteristics of each reservoir. In particular, the C_1:C_2 solvent system appears best suited for organic-rich liquid shales with lighter hydrocarbons and lower clay content (<15 wt%), where pore connectivity promotes efficient, vaporization-driven recovery.

Chapter 3: Experimental Evaluation of Cement Integrity on Exposure to Supercritical CO_2 using NMR: Application to Geostorage.

3.1 Abstract

Carbon sequestration is one approach to achieve carbon dioxide reduction in the atmosphere. Underground storage of CO_2 requires an understanding of geochemical and geomechanical alteration on the integrity of the injection wellbore. In this study, we investigate the reactivity of supercritical CO_2 ($scCO_2$) at 65°C and 20.7 MPa on Portland class G cement plugs used for oil and gas well completion, for exposure of up to 5 weeks.

For nanoporous media, such as cement, diffusion is believed to be the major mass transport mechanism (Perkins and Johnston 1963). To quantify the extent of the alteration (mineralization/dissolution) on fluid diffusivity through the cement matrix, a novel approach based on NMR is employed to derive diffusional tortuosity. Comparison of pre- and post-$scCO_2$ exposure, deuterium oxide (D_2O) intrusion profiles allow us to determine flow path alteration in the cement plugs. Additional characterizations include Fourier Transform Infrared Spectroscopy (FTIR) to observe the change in cement composition, micro–X-ray Computed Tomography (μXCT), along with Scanning Electron Microscopy (SEM) and Energy Dispersive Spectroscopy (EDS) to determine invasion extent and microstructure modifications, Mercury Injection Capillary Pressure (MICP) for pore throat size distribution and BET N_2 isothermal adsorption for surface area and pore size distribution.

The results show that exposure to $scCO_2$ promotes both calcium carbonate precipitation and dissolution simultaneously. However, the alteration is pore size dependent. After 5 weeks of exposure, there is evidence of carbonate dissolution in smaller pores (<30 nm) and both precipitation and dissolution in larger pores (30-200 nm). The alteration of the cement plugs leads

to a decrease in the storage and connectivity of the cement. The porosity decreased from 37 to 33% in 5 weeks, while the matrix tortuosity increased by 6 and 3 times after 2 and 5 weeks of exposure, respectively. The experimental results imply that the cement carbonate precipitation can limit the migration of $scCO_2$ through the cement matrix.

This work also highlights an alternative laboratory approach to quantify the risk associated with $scCO_2$ exposure to Portland cement using NMR-derived tortuosity.

3.2 Introduction

Carbon capture and storage (CCS) in the subsurface offers a viable option for reducing atmospheric CO_2 levels. However, for long-term geologic storage of CO_2, it is crucial to assess the risk of leakage along the wellbore components. In oil and gas wells, class G or H Portland cement is commonly utilized to seal the wellbore annulus and the reservoir formation. Under storage conditions, CO_2 in a supercritical state can react with cement components, namely calcium hydroxide ($Ca(OH)_2$) and calcium silicate hydrates (C-S-H), resulting in the formation of calcium carbonate ($CaCO_3$) (Kutchko et al. 2007, 2008, 2009, 2011); (Carey et al. 2007, Duguid and Scherer 2010, Gherardi et al. 2012, Walsh et al. 2014b, Carroll et al. 2016, Um et al. 2017, Duguid et al. 2019). The carbonation reaction can be divided into three phases: (i) CO_2 dissolution in the brine, forming carbonic acid (H_2CO_3), (ii) degradation of $Ca(OH)_2$ and/or calcium silicate hydrates, leading to the formation of calcium carbonates and amorphous silica, and (iii) conversion of calcium carbonate into calcium bicarbonate (Ahmed et al. 2015).

$$H_2CO_3 + Ca(OH)_2 \rightarrow CaCO_3 + 2H_2O$$

$$C\text{-}S\text{-}H + H_2CO_3 \rightarrow CaCO_3 + \text{amorphous silica} + H_2O$$

$$CaCO_3 + H_2CO_3 \rightarrow Ca(HCO_3)_2$$

Several studies have investigated the degradation of Portland cement by CO_2 using either batch exposure or flow-through experiments.

Barlet-Gouedard et al. (2006) and Rimmelé et al. (2008) conducted static batch measurements at 90°C and 27 MPa on cement exposed to $scCO_2$ and CO_2-saturated brine. They observed that carbonation follows a sealing stage related to calcium carbonate precipitation, plugging the pores, followed by a dissolution stage marked by a significant increase in porosity. (Kutchko et al. 2007, Kutchko et al. 2008) focused on the microstructure of cement during carbonation, revealing three distinctive zones: the unaltered cement, a zone depleted in portlandite, a calcium carbonated zone, and a residual amorphous silica zone. They also observed limited invasion of the carbonated front, estimated to progress around a few millimeters after 20-30 years.

Later, flow-through experiments were carried out to observe the dynamic impact of carbonation. Wigand et al. (2009) focused on fractured cement (cement-caprock interface) at 54°C and 19.9 MPa under $scCO_2$ injection, observing an increase in fracture aperture. Huerta et al. (2013) observed the self-healing of fractures with the injection of brine-saturated CO_2 at room temperature, postulating that fracture aperture and CO_2 residence time control mineralization inside the fracture. However, Luquot et al. (2013) reported that the fracture aperture after carbonation was related to the injection flow rate. Mason et al. (2013) investigated mechanical property changes near the carbonated zone, finding that Young's modulus in the depleted, carbonate, and amorphous layers decreased to approximately 75%, 64%, and 34% respectively of the unaltered cement after 8 days of exposure. Finally, Walsh et al. (2014a, 2014b), Walsh et al. (2013) investigated the impact of fracture geometry between the cement and the caprock, finding that changes in permeability depended on the initial fracture geometry.

Most of the highlighted studies, whether batch or flooding, have focused on measuring transport alterations (porosity and permeability) on dried samples. However, drying cement induced damage such as microcracking, fine pore collapse, and mineralogical transformation (Galle 2001).

To evaluate the flow quality of porous media, permeability is usually considered as the controlling transport parameter. Perkins and Johnston (1963) defined the general convective coefficient in porous media, including both the advective term (governed by permeability, pore throat size, and displacing velocity) and the diffusion term (governed by bulk fluid diffusivity and matrix tortuosity) in **Equation 3.1**.

$$K_l = \frac{D_o}{F\emptyset} + 0.5 U d_p \sigma \qquad 3.1$$

In which K_l (m^2/s) is the overall dispersion coefficient, the first term is associated with the dispersion by diffusion: D_o (m^2/s) is the mutual fluid diffusivity, $F\emptyset$ represent tortuosity, the second term is associated with the dispersion by advection/mechanical mixing: U (m/s) is viscous flow velocity (controlled by permeability), d_p (m) is characteristic pore throat diameter, and σ is porous heterogeneity. Previous studies have shown that in nanoscale porous media such as cement, the contribution of advection is relatively small, which makes diffusion the dominant drive mechanism (Perkins and Johnston 1963, Fleury and Brosse 2018).

In our study, we measure tortuosity, instead of permeability, by observing the effective diffusion of a doping agent using NMR on pre- and post-exposed samples of cement. This method allows evaluation of any changes while keeping the cement wet throughout the entire experiment and thus removing potential drying artifacts.

3.3 Theory and/or Methods

3.3.1 Sample Description and Exposure

Class G cement typically used for oil/gas wells completion was used in this study. A total of 3 cement samples (1x1in) were used; one intact and 2 exposed to $scCO_2$ for 2 and 5 weeks, respectively. The plugs were used for D_2O diffusivity, while companion disks (0.25x1in) were used to measure SEM, μXCT, MICP, and BET. The cement plugs were cured at 65°C for 30 days. These plugs had a total porosity of 37±2%. The X-ray fluorescence mineralogy of the untreated sample is given in **Table 3.1**.

Figure 3.1 shows the experimental workflow used in this study. The samples were vacuum imbibed for a week in a H_2O-brine solution (1.2% KCl, 1.2% NaCl, and 3.6% $CaCl_2$) to match the salinity and resistivity of the solution used to cure the cement samples and ensure 100% saturation. A D_2O-brine solution with similar salt concentration was prepared to monitor the diffusivity of D_2O-brine into the cement matrix pre- and post-exposure.

After imbibition for 48 hours, all samples except the control samples were exposed to $scCO_2$ at 65°C and 20.7 MPa for 2 and 5 weeks inside a Parr reactor, as shown in **Figure 3.2**, and intrusion of D_2O-brine into the cement plug was monitored as a function of time using NMR. This data allowed us to calculate the diffusivity of D_2O-brine in the cement plugs.

Table 3.1- X-ray fluorescence-derived mineralogy measured on the untreated cement, showing mostly CaO and SiO_2 components.

	MgO	CaO	K_2O	Fe_2O_3	SiO_2	Al_2O_3
Composition (wt%)	2	64	1	8	19	6

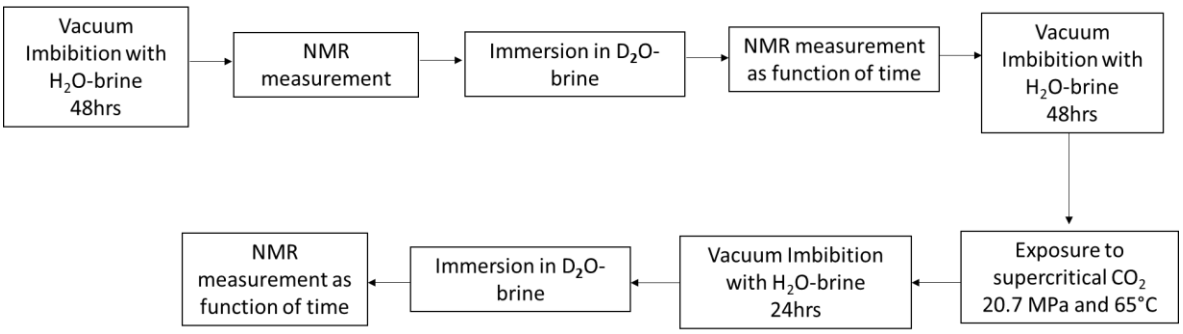


Figure 3.1 - Experimental workflow used in the present study. Flow path alteration was determined by comparing D_2O-brine diffusivity before and after exposure to $scCO_2$.

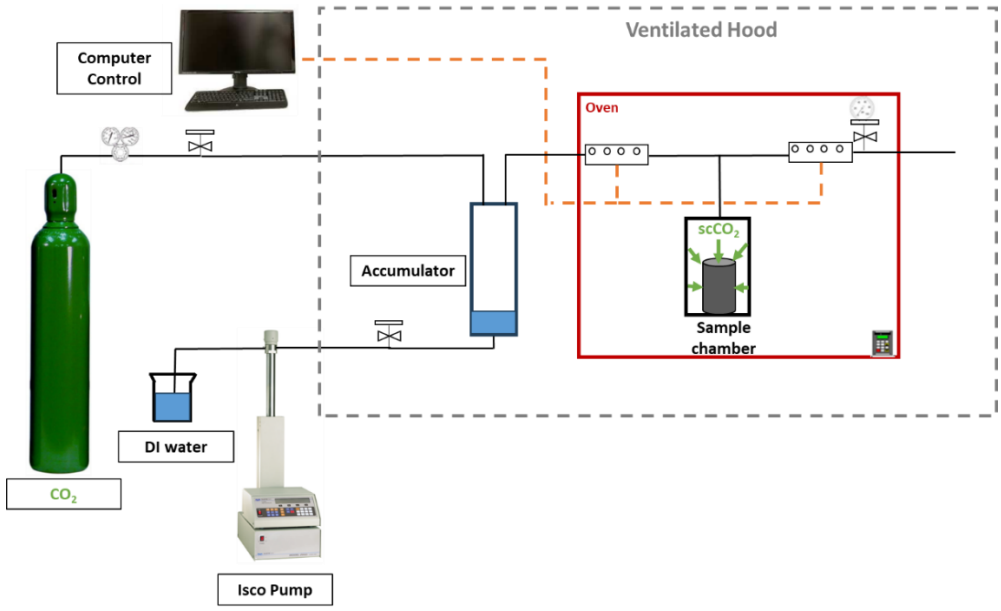


Figure 3.2 - Schematic of CO_2 exposure apparatus. Exposure was carried out at 20.7 MPa and 65°C, conditions at which CO_2 is in a supercritical state.

3.3.2 Diffusional Tortuosity

A 12 MHz Oxford Geospec™ spectrometer (TE=114 µsec) with a Green Imaging Technology acquisition and processing software was used to acquire the total T_2 signal, which is calibrated to determine H_2O volume within the cement matrix. The T_2 relaxation represents the relaxation or decay of hydrogen protons in the pore fluid after exposure to a magnetic field. The area under a T_2 distribution is directly proportional to the amount of hydrogen-based fluid present in the sample. NMR T_2 is governed by **Equation 3.2**:

$$\frac{1}{T_2} = \frac{1}{T_{2\,bulk}} + \rho_2 \frac{S}{V} + D\frac{(\gamma\, G\, TE)^2}{12} \qquad 3.2$$

T_2 : Transverse relaxation time (ms)

$T_{2\,bulk}$: Bulk fluid relaxation time (ms)

ρ_2 : The surface relaxivity (μm/s or m/s)

$\frac{S}{V}$: Surface-to-volume ratio (m^{-1})

D : Bulk diffusion coefficient of the in-situ pore fluid (m^2/s)

γ : Gyromagnetic ratio (Hz/T)

G : Magnetic field gradient (T/m)

TE : Echo spacing time (s)

For our experiment the 1st term and 3rd term can be dropped, thus the T_2 relaxation time is related to surface relaxivity and the pore surface-to-volume ratio. Equation 3.2 can be simplified to:

$$\frac{1}{T_2} = \rho \frac{2}{r} \qquad 3.3$$

Where r is the radius of the pore in m, and ρ is the surface relaxivity of cement assuming carbonates, 5μs/s (Chang et al. 1994, Matteson et al. 2000, Dunn et al. 2002). Knowing the surface relaxivity of the minerals (Kleinberg 1996), T_2 distribution can also be converted to pore sizes.

Tortuosity measures the obstruction that fluid molecules must overcome to move through a porous medium. It is calculated as the ratio of the square root of the effective diffusivity of the fluid in the porous medium to the bulk fluid diffusivity **(Equation 3.4**). The effective diffusivity of the cement samples was calculated by measuring the reduction in NMR T_2 relaxation response during D_2O-brine immersion pre- and post-exposure. The effective diffusivity of D_2O-brine in the cement was

derived by matching 1-D Fick's law of diffusion (**Equation 3.5**), assuming radial diffusion and the D_2O-brine NMR intrusion profile. A detailed explanation is presented by Dang et al. (2021) and Odiachi et al. (2022).

The following equation is used to estimate sample tortuosity from diffusivities:

$$\tau^{1/2} = \frac{D_{bulk}}{D_{eff}} \quad 3.4$$

D_{eff}**:** Effective diffusivity of D_2O-brine in cement (m^2/s)

D_{bulk}: Bulk fluid diffusivity of H_2O in D_2O, 2.3 x 10^{-9} m^2/s at 25ºC (Baur et al. 1959)

$$\frac{\partial C_a}{\partial t} = D\frac{\partial^2 C_a}{\partial x^2} \quad 3.5$$

C_a : Concentration of solute (kg/m^3)

D : Diffusion coefficient (m^2/s)

x : Distance (m)

3.3.3 Chemical and Microstructural Analysis

An FEI Helios Nanolab 600 Dualbeam FIB/SEM with a backscattered electron (BSE) detector and an Oxford X-MAX energy-dispersive spectrometer were used to determine microstructure and elemental changes on the surface of cement plugs pre- and post-exposure to $scCO_2$. The brightness of the BSE image reflects the average atomic number of a given phase composition. The depth of the altered zone was observed using μx-ray computed tomography in an Xradia XCT-400. Finally, transmission Fourier transforms infrared spectroscopy (Sondergeld and Rai 1993) was used to observe the change in different functional groups, reflecting the alteration in cement composition after gas exposure.

3.3.3 Pore Structure Alteration

Isothermal N_2 adsorption and mercury injection capillary pressure measurements on dried samples were used to characterize the change in surface area and pore throat size, respectively. BET surface area was measured using a Micrometrics Tristar 2 apparatus. Density Functional Theory (DFT) assuming slit pore type (Sinha 2017) was used to convert surface area to pore size. For MICP, a Micrometrics AutoPores IV apparatus was used to capture pore throat size distribution, from 2 nm up to 20 μm with a maximum intrusion pressure of up to 415 MPa.

3.4 Results

3.4.1 Diffusional Tortuosity

Figure 3.3 shows the NMR T_2 relaxation of the control sample during immersion into D_2O-brine. Over time the NMR signal amplitude decreases as D_2O-brine is gradually replaced by H_2O-brine inside the cement, from 6.7 to 2.3 ml. **Figure 3.4a** and **Figure 3.4b** show the impact of $scCO_2$ on the T_2 relaxation after 2- and 5-week exposure. Both samples exhibited a decrease in signal amplitude over time, indicating an intrusion of D_2O-brine. However, both $scCO_2$-exposed samples showed a slower intrusion rate as compared to the unreacted cement. After 168 hours of immersion in D_2O-brine 4.3 ml and 3.5 ml of H_2O-brine remain in the 2- and 5-weeks exposed samples, as opposed to 2.3 ml in the untreated sample. This implies an impediment in the flow path due to the alteration in the matrix by $scCO_2$. When comparing both exposed samples, D_2O-brine intrusion is the highest after 5 weeks of exposure, with 40% intrusion versus 27% after 2 weeks of exposure to $scCO_2$. Finally, comparing the T_2 distribution of the untreated and 5 weeks exposed $scCO_2$ cement after 100% saturation with H_2O-brine (**Figure 3.5)** shows that there is a 10% reduction in pore volume between 0.3-10 ms. Assuming carbonate is the main component of the cement and spherical pores (Equation 3.3). Most volume reduction occurs in pore bodies between 3-100 nm.

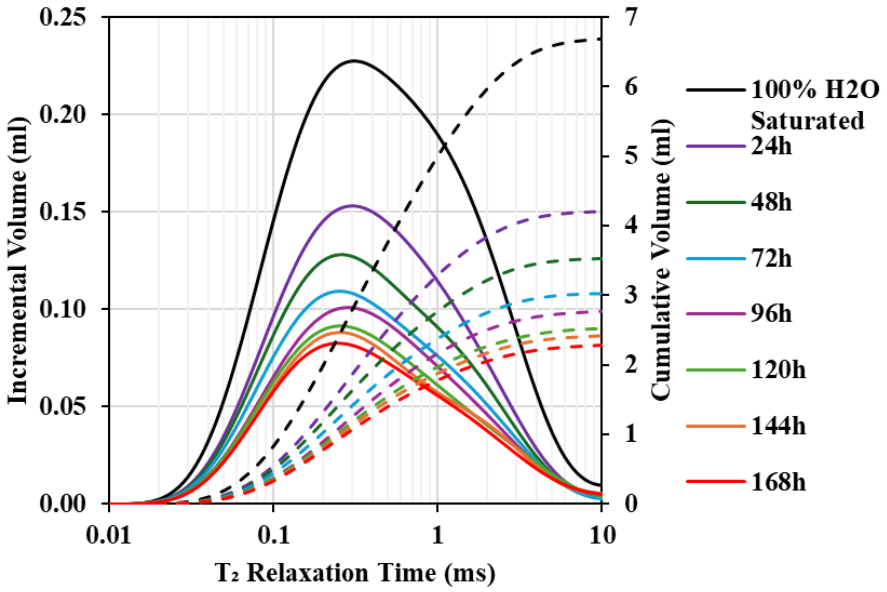


Figure 3.3 - NMR T_2 relaxation distribution of the controlled cement plug immersed in D_2O-brine showing a gradual decrease in volume of the H_2O-brine as D_2O-brine replaces H_2O-brine inside the plug. Over 168 hours, the volume of H_2O-brine decreased from 6.7 to 2.3 ml (dashed curves).

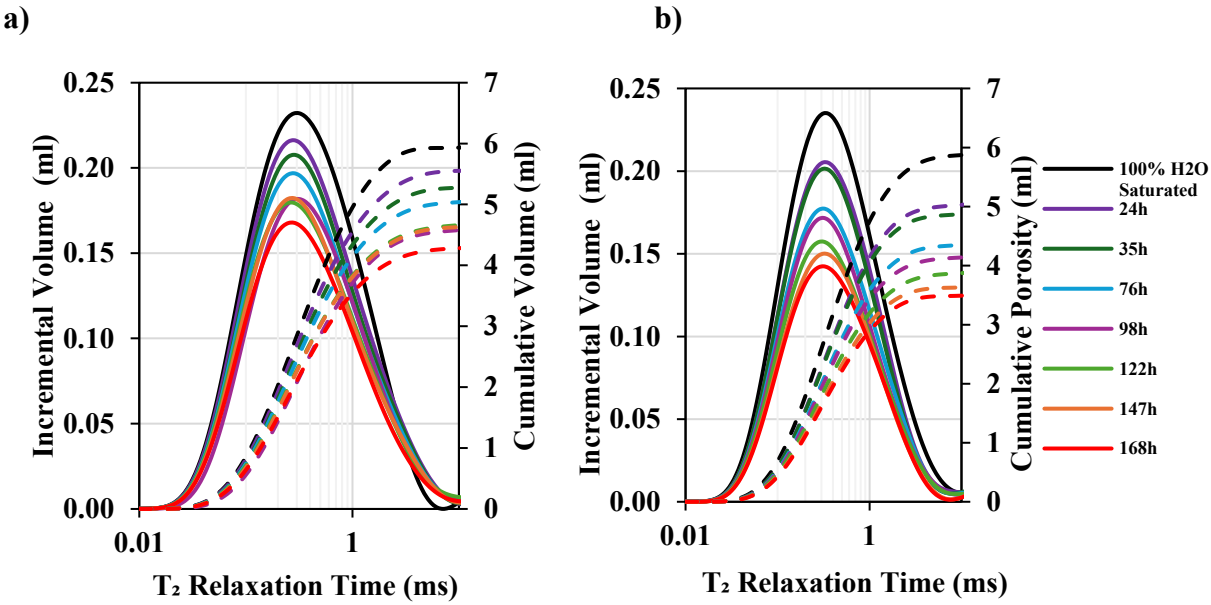


Figure 3.4 - NMR T_2 relaxation distribution during immersion in D_2O-brine after 2 weeks (a) and 5 weeks (b) exposure of cement plugs to $scCO_2$ showing 40% vs 27% D_2O-brine intrusion after 5 weeks and 2 weeks, respectively.

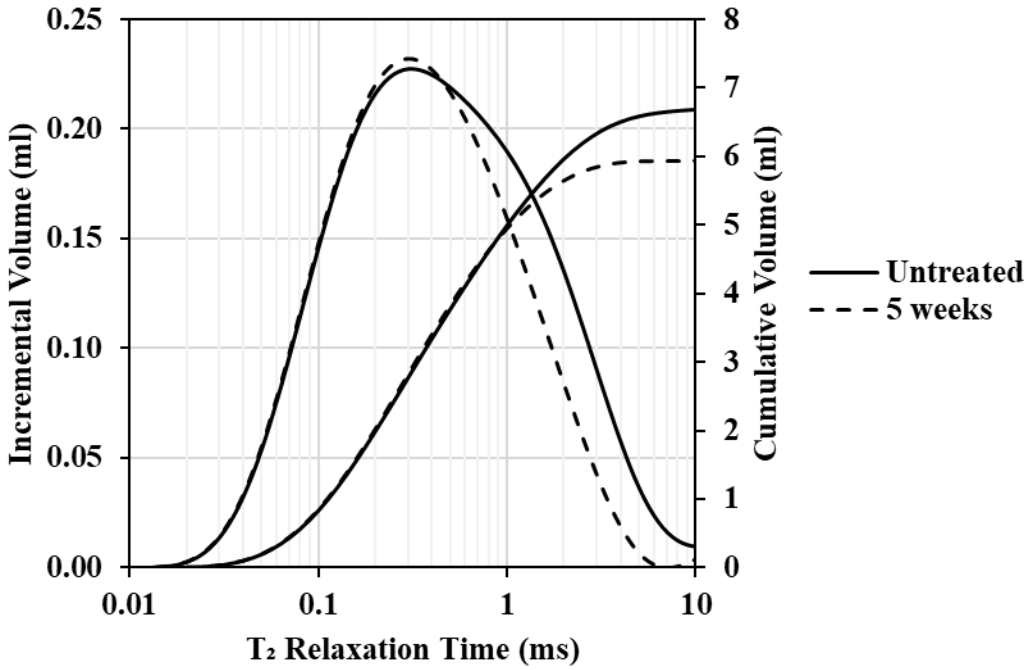


Figure 3.5 - Comparison between the untreated and 5 weeks $scCO_2$ exposed cement after 100% saturation with H_2O-brine showed a reduction in a pore volume between 0.3 -10 ms, resulting in an overall 10 % loss of pore volume after exposure.

Figure 3.6 and **Table 3.2** show the D_2O-brine intrusion profile and the derived tortuosity (Equation 3.4). Knowing the effective D_2O-brine diffusivity of the untreated cement, the exposed cement effective diffusivity was calculated by using the slope of the intrusion profile (Figure 3.6) after 2 days of D_2O-brine imbibition. After 2 weeks of exposure, the cement tortuosity increased by a factor of 6, indicating pore blockage. However, the tortuosity increased by only a factor of 3 after 5 weeks compared to the untreated sample, this suggests precipitation of carbonate earlier on and dissolution at a later stage. This observation is consistent with Rimmelé et al. (2006) model with an initial sealing stage related to calcium carbonate precipitation plugging the porosity, followed by a dissolution stage marked by a significant increase of porosity.

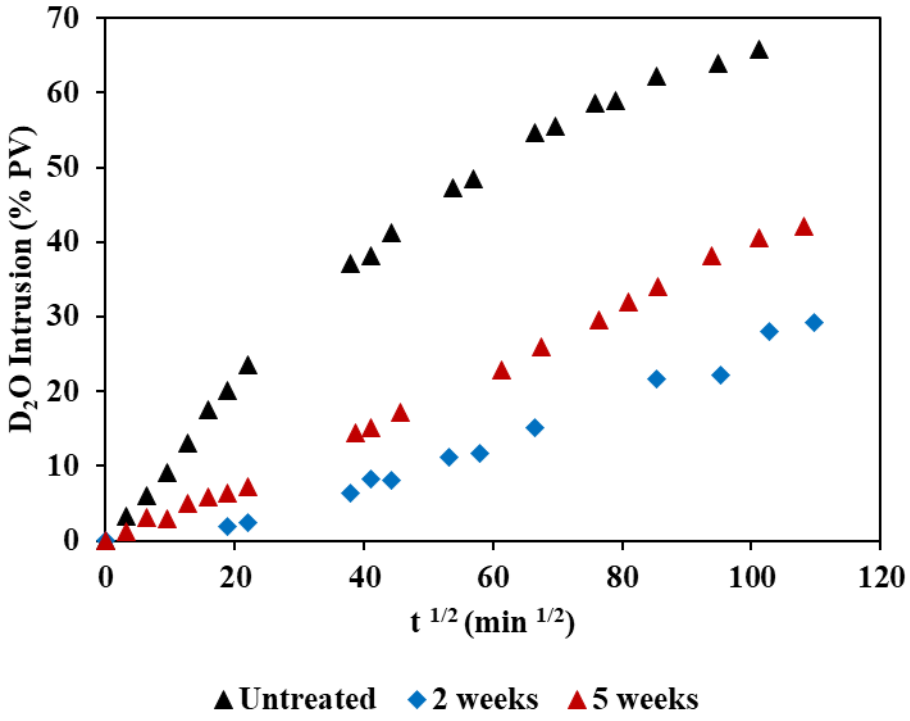


Figure 3.6 - D_2O-brine intrusion profile on the cement plugs after 2 and 5 weeks- of exposure to $scCO_2$ at 65°C and 20.7 MPa, showing D_2O-brine flow reduction after $scCO_2$ exposure.

Table 3.2 - Derived tortuosity from Figure 3.6. The tortuosity increased by 6 and only by 3 after 2 and 5 weeks, respectively. This suggests an initial precipitation of calcium carbonate and a later dissolution.

Cement	Effective D_2O-brine diffusion (m^2/s)	Tortuosity
Untreated	1.20×10^{-10}	4.4
2 weeks	3.09×10^{-12}	27.3
5 weeks	1.45×10^{-11}	12.6

3.4.2 Pore Structure Alteration

MICP (**Figure 3.7a**) and N_2 isothermal adsorption (**Figure 3.7b**) measurements on the dried specimens after 5 weeks of exposure confirm that there has been a significant alteration in the flow paths. Figure 3.7a shows the reduction in pore throat size peak from 50 nm to 30 nm after 2 weeks, indicating a decrease in pore throat size, which suggests that the carbonation process reduces the effective pore volume of the cement. However, after 5 weeks, the average 30 nm pore throat size

has significantly decreased, resulting in the generation of smaller pore throats between 2-30 nm. The N_2 isothermal adsorption in Figure 3.7b shows that the large pores (>30 nm) volume increased after 2 weeks and subsequently decreased after 5 weeks, while only an increase in pore volume is observed in small pores (<30 nm) after 2 and 5 weeks. This implies both dissolution and precipitation in large pores and dissolution only in small pores.

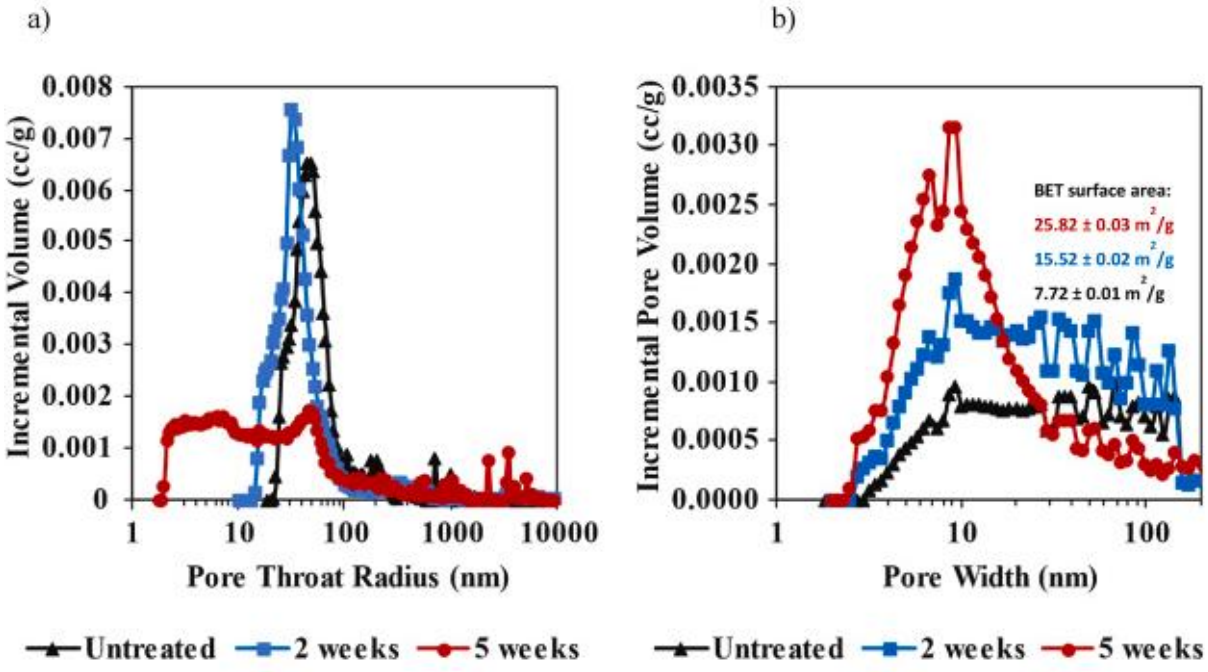


Figure 3.7 - (a) MICP pore throats and (b) DFT pore body size distribution after 2- and 5-weeks exposure to $scCO_2$ at 65°C and 20.7 MPa. MICP data shows a decrease in pore throat size (i.e., connectivity) of the cement after carbonation. N_2 isothermal adsorption shows initial dissolution and later precipitation of $CaCO_3$ in large pores (>30nm), while only dissolution occurs in small pores (2-30 nm).

3.4.3 Chemical and Microstructural Analysis

Cross-sectional imaging of the cement plug using XCT showed a clear textural distinction between the altered and unaltered portions in the cement plugs (**Figure 3.8**). After 5 weeks of exposure to $scCO_2$, the plug showed deeper invasion around 10 mm, while after 2 weeks, the invasion depth was only 3 mm. The FTIR analysis (**Figure 3.9**) of the invaded zone revealed the presence of calcite (absorbance peak around 1400 and 875 cm^{-1})

After 5 weeks of exposure, the BSE image presented in **Figure 3.10** also shows a clear demarcation between the two zones, based on brightness (i.e. proportional to average atomic number). The invaded zone appears to be darker with a well-defined boundary. The cement matrix ($Ca(OH)_2$ and C-S-H) seems to have been altered after $scCO_2$ exposure. The alteration is visible on the unhydrated grain turning dark in the $scCO_2$-invaded zone. The EDS maps (**Figure 3.11**) performed at the same location confirm that the unhydrated cement grain underwent decalcification and the cement matrix has been enriched in calcium and carbon after $scCO_2$ exposure **(Figure 3.12 & 3.13)**. This finding aligns with the observations made by Kravanja and Knez (2023) regarding the disparity in mineral composition, specifically calcium, and carbon, between the CO_2-affected and non-affected zones.

Interestingly, magnesium also precipitated (Figure 3.11), however, it seems to be located around the carbonated front, suggesting the potential formation of magnesium carbonates. MgO was also present in our cement (Table 3.1). MgO is often added to cement to improve the mechanical properties and durability of the cement under harsh downhole conditions (Buntoro and Rubiandini 2000). $Mg(OH)_2$ can react with $scCO_2$ and form $MgCO_3$ (Gardeh et al. 2022). $MgCO_3$ crystals are insoluble in water and, hence do not easily leach out from the cement (Frimmel 1996, Ahmed et al. 2015)

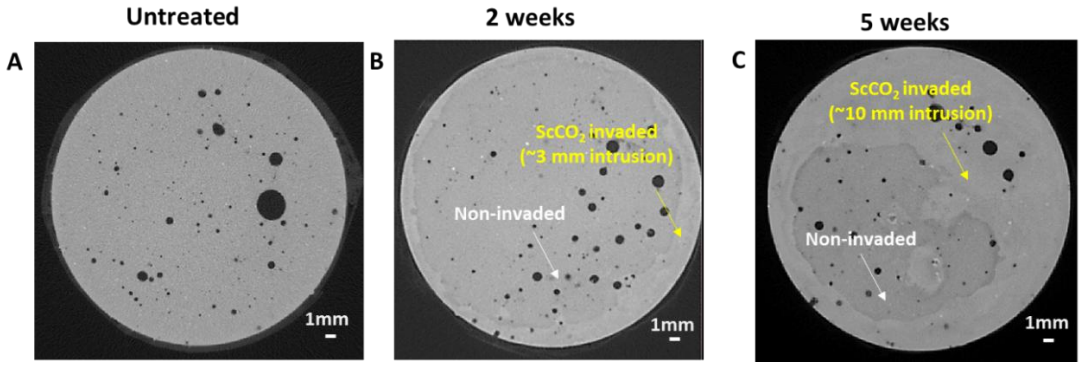


Figure 3.8 - XCT images of the 3 different cement samples showing the $scCO_2$ invaded (yellow arrow) and the non-invaded (white arrow) after 2 weeks (B) and 5 weeks (C) exposure to $scCO_2$ at 65°C and 20.7 MPa. A deeper invasion is observed after 5 weeks. Note: Each cross section was taken 0.25 inches from the top of the plugs to capture the $scCO_2$ front.

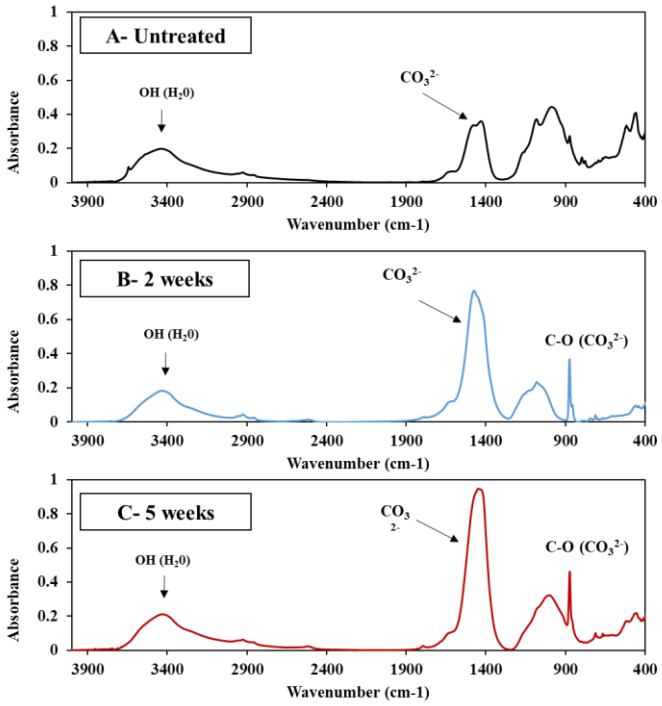


Figure 3.9 - FTIR mineralogy of the cement (A) untreated, (B) after 2 weeks, and (C) 5 weeks exposure to $scCO_2$, showing calcite absorbance bands around 1400 cm^{-1}, and 875 cm^{-1}.

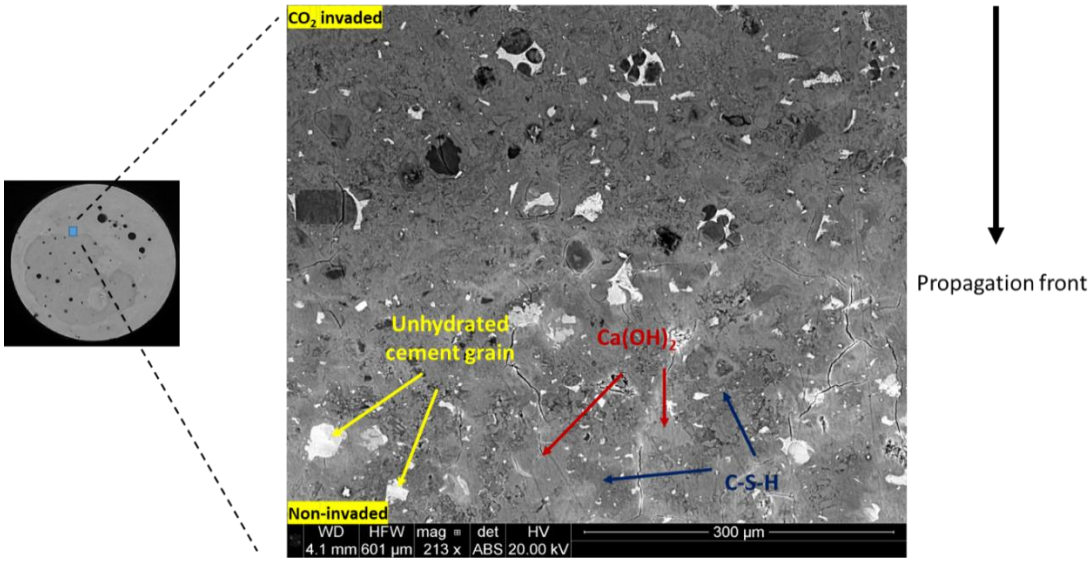


Figure 3.10 - Backscattered electron image after 5 weeks of exposure to $scCO_2$ at 65°C and 20.7 MPa. Clear textural demarcation can be observed between the invaded and non-invaded zones. The area invaded by $scCO_2$ appears darker, and the cement grain and matrix appear altered, with less $CaOH_2$ and C-S-H. Note: The cement was imaged without coating.

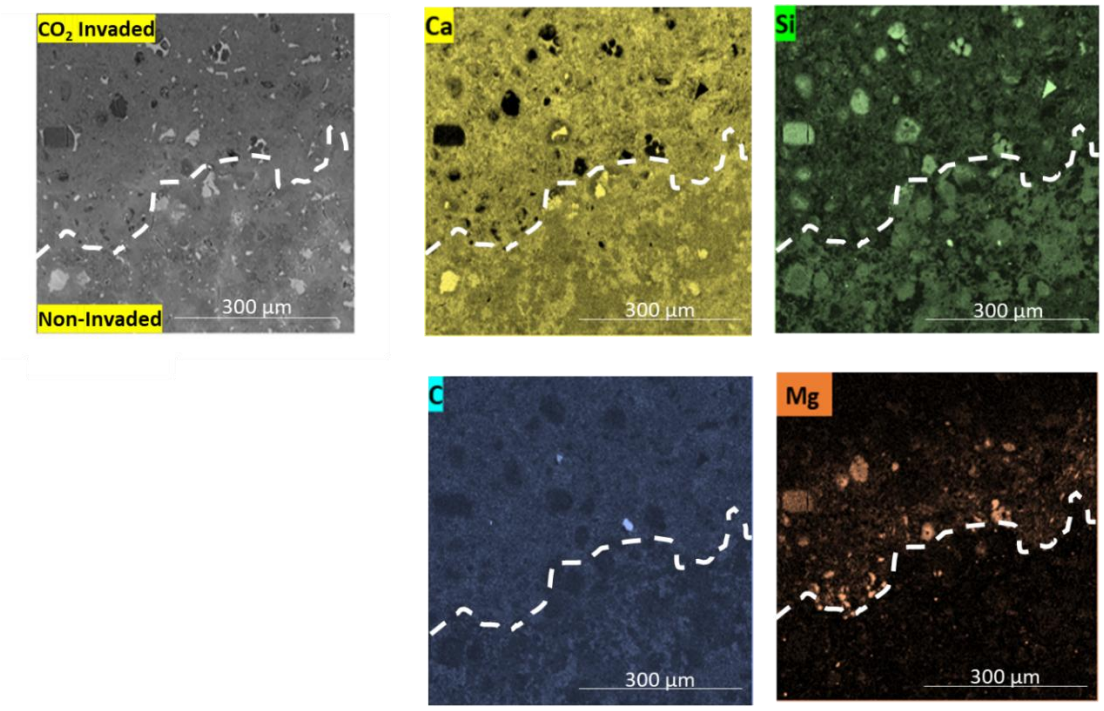


Figure 3.11 - EDS maps at the boundary between carbonated and non-carbonated zones after 5 weeks of $scCO_2$ exposure at 65°C and 20.7 MPa. The dashed line represents the $scCO_2$ front. After exposure, the unhydrated cement grains have been decalcified in the $scCO_2$-invaded zone. The invaded zone matrix appears to have less Si but more magnesium and carbon. Note magnesium seems to be localized near the $scCO_2$ front only.

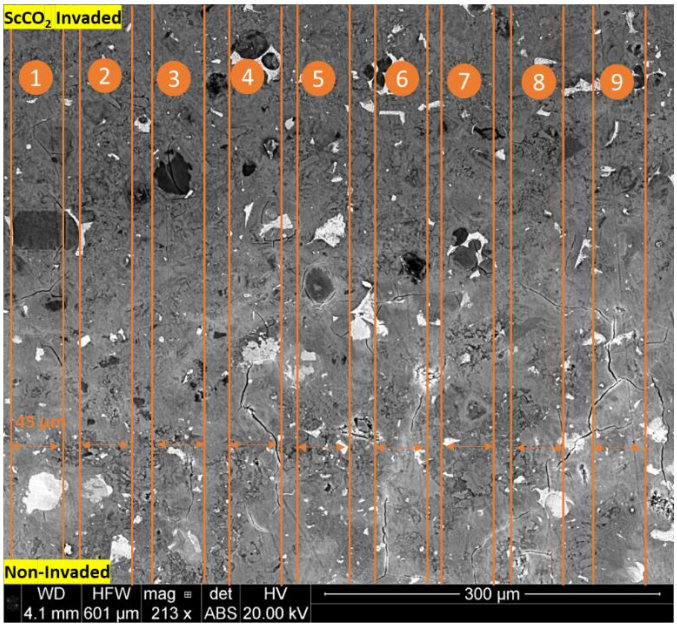


Figure 3.12 - 9 scan lines were used to determine the elemental profiles (Ca, Si, Mg, and C) over the altered region shown in Figure 3.10 and Figure 3.11. Each line is 45 µm wide (20 pixels) and 500µm long. Elemental composition was measured by averaging the grayscale intensity of the lines for each component.

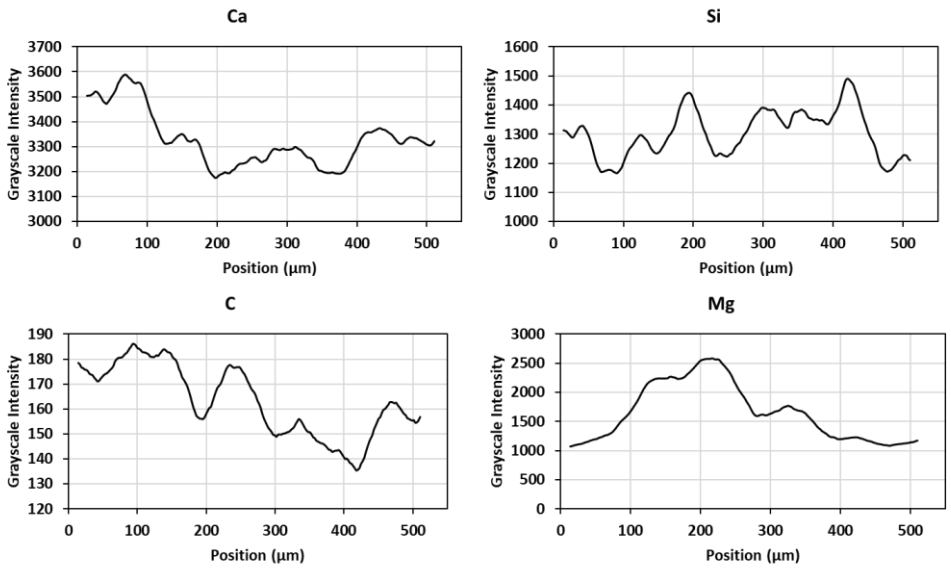


Figure 3.13 - Elemental profiles generated from the X-ray map (Figure 3.12) of cement exposed to $scCO_2$ at 65°C and 20.7 MPa for 5 weeks. This data corresponds to an average elemental composition of 9 vertical scans. Position 10 µm corresponds to the top of the SEM image ($scCO_2$-invaded zone), while position 510 µm corresponds to the bottom section of the SEM image (the non-invaded zone) of the cement. The $scCO_2$ invaded zone appears richer in calcium and carbon mostly. Mg is also present near the carbonation front (≈200 µm)

3.5 Discussion

The results show that the interaction between $scCO_2$ and brine-saturated Class G Portland cement leads to significant changes in the pore structure due to mineralization. Analysis of D_2O-brine and tortuosity data indicates that the cement network undergoes calcium carbonate precipitation after 2 weeks, resulting in an increase in cement tortuosity from 4 to 27 ±2. However, after 5 weeks, the cement tortuosity decreases to 12 ±2, suggesting a dissolution process. This observation aligns well with the two-stage connectivity evolution proposed by Rimmelé et al. (2008), where an initial sealing stage occurs, associated with porosity plugging caused by calcium carbonate precipitation, followed by a reopening of pore entrances during the dissolution phase. The 2-stage porosity could also be pore size dependent, as shown in the BET data. The small pores (2-30nm) seem to have

undergone precipitation and dissolution of $CaCO_3$, while the larger pores (>30nm) are in the initial phase of precipitation of $CaCO_3$.

The D_2O-brine diffusivity-based approach also confirms a permeability reduction as shown by the increase in tortuosity by a factor of 6 after 2 weeks and by 3 after 5 weeks of $scCO_2$ exposure (Figure 3.6), MICP data also shows a reduction of the main pore throat size (50 nm), which would decrease the connectivity of the cement and decrease the accessible pore volume for $scCO_2$ over time.

The tortuosity results (Table 3.1) and Eq. 3.4 can also be used to calculate the diffusion coefficient of $scCO_2$ following exposure. In storage conditions, the effective $scCO_2$ diffusion coefficient with pure water ranges between $4\text{-}8x10^{-9} m^2/s$ (Cadogan et al. 2014, Zarghami et al. 2017). Assuming a value of $6x10^{-9}$ m^2/s. the diffusion coefficient is projected to fall within the range of $8.0x10^{-12}$ to $3.8x10^{-11} m^2/s$ after 2 and 5 weeks of exposure. This estimation appears one order of magnitude lower than the diffusion coefficient of CO_2 of tight sedimentary rocks documented by Fleury and Brosse (2017), which ranges from $5x10^{-11}$ to $5x10^{-10}$ m^2/s, confirming limited diffusion over time.

The observation, although limited to one type of cement, shows a rapid decrease in D_2O effective diffusion from 1.20×10^{-10} m^2/s to 3.09×10^{-12} m^2/s after 2 weeks, followed by a gradual increase to 1.45×10^{-11} m^2/s after 5 weeks. This trend suggests that the mineralization reaction is stabilizing, potentially limiting CO_2 leakage through the cement matrix. However, long-term exposure needs to be tested to verify whether this stabilization persists.

These short-term findings are consistent with field and modeling studies by Kutchko et al. (2007, 2008), who estimated minimal CO_2-saturated brine diffusion to 1 mm over 20–30 years. Similarly, Carey et al. (2006) observed limited CO_2 migration in cement from a 30-year-old EOR project in the SACROC field, West Texas.

3.6 Conclusions

In the context of carbon capture and storage, the findings of this study lead to the following conclusions:

- The use of NMR-derived tortuosity proves to be a valuable tool in quantifying the integrity of wellbore cement material for carbon storage.
- Exposure to $scCO_2$ resulted in a decrease in porosity from 37-33%.
- The decrease in average pore throat size confirms a reduction in pore connectivity of the cement.
- The cement tortuosity increased by a factor of 3-6 after 2- and 5 weeks of exposure, confirming pore blockage and slower migration over time.
- The carbonation process was not only time but also pore-size dependent. In smaller pores (<30 nm), only dissolution of calcium carbonate was observed, whereas, in larger pores (30-200 nm), both precipitation and dissolution took place.
- After exposure, the invaded zone of the cement matrix appears to be richer in calcium and carbon while only along the invasion front, magnesium concentration seems to increase.

Our proposed methodology for assessing flow path alteration using tortuosity lays the groundwork for future research. Subsequent studies will focus on evaluating changes in mechanical property and dependence of flow path alteration on cement composition under $scCO_2$ conditions.

Chapter 4: Hydrogen Interaction in Bulk Fluids for Geological Storage Application Using NMR

4.1 Abstract

Hydrogen geostorage is a crucial component of decarbonization, enabling large-scale energy storage and supporting the transition to a low-carbon economy. By allowing long-term hydrogen storage in subsurface formations such as depleted oil and gas reservoirs, geostorage enhances energy security and stabilizes energy supply.

This study serves as a preliminary step before investigating H_2 interactions in saturated porous rocks, focusing on hydrogen behavior in reservoir fluids using NMR. The tested fluids include water, dodecane oil (light oil), dead oil, and ozokerite wax (heavy hydrocarbon) under pressures up to 1800 psi. Additionally, deuterated water (D_2O) and fluorinert HT-230 were used as control fluids due to their negligible NMR signals. Fluorinert HT-230, commonly used as a confining fluid in core plug measurements, also provides a baseline for comparison.

T_2 relaxation times served as a proxy for distinguishing free hydrogen from dissolved hydrogen in bulk liquid based on molecular interactions. Since T_2 time is sensitive to hydrogen protons in fluids, it was used to assess changes in bulk fluid properties.

The results indicate that hydrogen predominantly remains in the free phase when interacting with water. This supported by the fast relaxation times (1–20 ms) and no observed changes in T_2 with pressure, confirming limited dissolution. Similarly, hydrocarbons such as dodecane, dead oil, and wax showed no evidence of hydrogen dissolution, as only free-phase hydrogen signals (1–20 ms) were detected by NMR. However, visual observations of gas bubbles in dead oil suggest physical hydrogen trapping rather than true molecular dissolution, indicating hydrogen retention in a discrete gas phase without full integration into the liquid phase.

In fluorinert, an intermediate T_2 relaxation signal (100–300 ms) suggests possible hydrogen dissolution, with an estimated volume of 4–6 cc of H_2 per 100 cc of fluorinert at 1800 psi and room temperature. This finding indicates that while fluorinert is generally inert, some level of hydrogen interaction may occur. Therefore, caution is advised when using fluorinert as a confining fluid in core plug tests with H_2 under stress, or this signal should be excluded from analysis.

Although this study was conducted at relatively low temperatures and over short experimental durations, the results show hydrogen can be physically trapped in dead oil within our test conditions. These results provide a baseline understanding of H_2 interactions in bulk fluids, informing future core plug measurements of hydrogen retention, diffusion, and mobility in depleted oil and gas reservoirs.

4.2 Introduction

The subsurface storage of hydrogen in geological formations is emerging as a key solution for large-scale energy storage, especially in the context of renewable energy integration (Heinemann et al. 2021).

The technical and economic feasibility of hydrogen geostorage depends on factors such as gas storage volume, reservoir and caprock integrity, and potential geochemical interactions (Zivar et al. 2021, Heinemann et al. 2021). Hydrogen can interact with geological formations through various mechanisms, including changes in mineral wettability (Iglauer et al. 2021, Zeng et al. 2022, Higgs et al. 2022, Hosseini, Ali, et al. 2022, Hosseini, Fahimpour, et al. 2022) and mineral dissolution (Bensing et al. 2022, Al-Yaseri et al. 2023). In deep radioactive repository, redox reactions in shales, such as Fe^{3+} reduction to Fe^{2+}, can lead to the transformation of pyrite into pyrrhotite (Truche et al. 2010, Truche et al. 2013). These processes may affect hydrogen storage

volume, induce H_2S production, and alter pore fluid composition, potentially compromising reservoir integrity (Flesch et al. 2018). However, some studies suggest that abiotic geochemical reactions in sandstone reservoirs pose a lower risk to hydrogen storage (Yekta et al. 2018, Hassanpouryouzband et al. 2022).

Another critical factor in evaluating the feasibility and efficiency of this process is understanding hydrogen's interaction with reservoir fluids, particularly its interaction with hydrocarbons, such as oil, in depleted oil and gas reservoirs at high pressure and temperature to prevent H_2 loss. Previous work using 1D NMR has shown that T_2 relaxation can be used to separate hydrogen in free gas and hydrogen in bulk water in sandstone (Ho et al. 2024, Dang et al. 2025). Free gaseous hydrogen relaxes at T_2 <50ms, while bulk water relaxes T_2>1000ms.

NMR T_2 relaxation (transverse relaxation) is based on the excitation and subsequent relaxation of hydrogen nuclei in the pore fluid, with the governing mechanisms in porous media **Equation 4.1**.

$$\frac{1}{T_2} = \frac{1}{T_{2\,bulk}} + \frac{1}{T_{2\,Surf}} + \frac{1}{T_{2\,Diff}} \qquad 4.1$$

Where bulk relaxation (T_{bulk}) is governed by the inherent properties of the fluid, such as viscosity and composition, surface relaxation (T_{surf}) arises from interactions between fluid molecules and solid pore surfaces. The latter depends on the pore surface-to-volume ratio (S/V) and is influenced by the mineralogy and surface chemistry of rocks. Finally, diffusion relaxation (T_{diff}) occurs due to molecular diffusion in the presence of magnetic field gradients, leading to dephasing of the magnetic signal.

In our experiment, the third and fourth terms can be disregarded as there is no porous media and no applied magnetic field gradient. Consequently, the T_2 relaxation time is influenced solely by

the fluid's properties (viscosity, density, and composition, Hirasaki et al. 2003). Therefore, T_2 can be modeled purely by bulk properties, allowing Equation 4.1 to be simplified to:

$$\frac{1}{T_2} = \frac{1}{T_{2\,bulk}} \tag{4.2}$$

Therefore, in low-viscosity fluids, T_2 relaxation is inversely proportional to viscosity (Hirasaki et al. 2003, Hirasaki and Mohanty 2007). However, factors such as paramagnetic impurities and temperature variations must be carefully accounted for to ensure accurate interpretations (Coates et al. 1999, Chakravarty et al. 2018, Kausik et al. 2016).

In this preliminary study, we demonstrate the capabilities of low-field NMR to characterize hydrogen interactions by monitoring changes in T_2 relaxation as a proxy for bulk property variations, with pressure in deionized water and hydrocarbon fluids (dodecane, dead oil, and wax). Additionally, non-organic fluids, including deuterated heavy water and fluorinert, were tested. Deuterated heavy water, which lacks an NMR signal from hydrogen (^1H), is commonly used as a doping agent to suppress the water signal in plug NMR measurements of dual-phase systems (oil and water) (Zainuddin et al. 2019, Kelly et al. 2021). The fluorinert, which contains no hydrogen protons, serves as a confined fluid for NMR core plug measurements under stress conditions.

4.3 Theory and/or Methods

4.3.1 Sample Selection

For these experiments, six fluids were used: DI water, deuterated water (D_2O), fluorinert HT-230, dodecane oil (C_{12}), dead oil from the Eagle Ford formation, and ozokerite wax. D_2O and fluorinert were chosen as control fluids for their negligible NMR signals. Therefore, potential contamination of these 2 fluids by H_2 needs to be investigated before core testing.

4.3.2 Experimental Procedure

For each experiment, 20 mL of fluid was placed inside a glass vial. Hydrogen gas with 99% purity was used for testing. NMR T_2 relaxation distributions were measured using a Carr-Purcell-Meiboom-Gill (CPMG) pulse sequence at a frequency of 2 MHz with a Magritek Rock Core Analyzer (RCA) instrument at room temperature. Measurements were conducted at an echo spacing of 100 μs to capture the fast relaxation of free hydrogen, with a T_2 max of 300 ms. For each T_2 relaxation experiment, an SNR>100 was achieved on the bulk fluid pre-hydrogen injection.

The tests were performed using a Daedalus® core holder made of NMR-transparent ZrO_2, capable of operating at pressures up to 10,000 psi. The core holder was positioned inside the NMR spectrometer, ensuring the samples were centered within the uniform magnetic field section **(Figure 4.1**). The experimental setup included an ISCO syringe pump, which compressed hydrogen through an accumulator and injected it into the sample at target pressures of 500, 1,000, and 1,500 psi, maintaining each pressure for one hour. Before each experiment, the system was purged with nitrogen gas to ensure a clean and controlled environment.

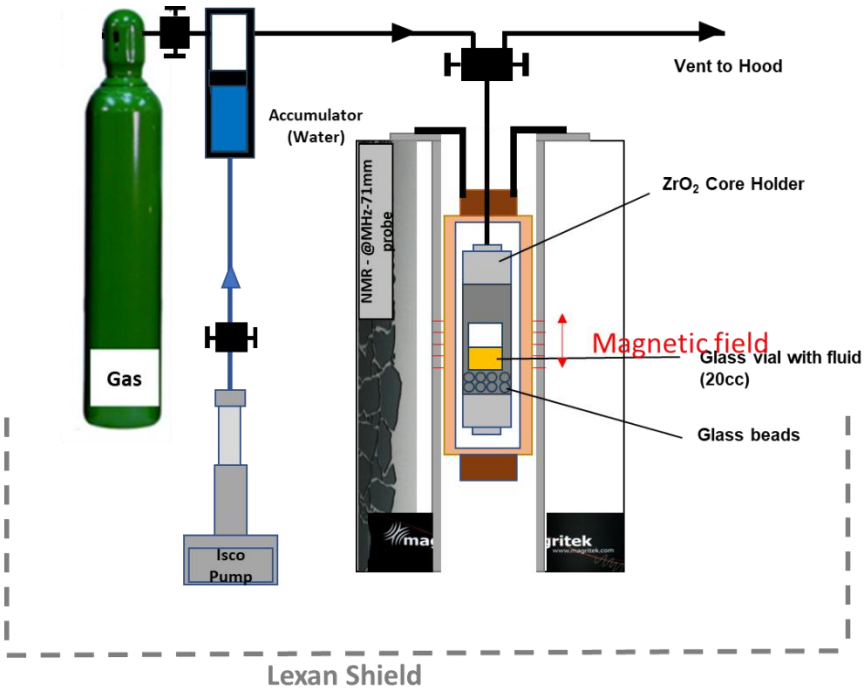


Figure 4.1 - The diagram illustrates the flow of hydrogen gas from the hydrogen cylinder (left) through an ISCO pump, which compresses the gas and injects it into the NMR-compatible core holder (center) containing the fluid sample. The core holder, made of NMR-transparent ZrO_2, is positioned inside the NMR spectrometer probe, and glass beads with no NMR signal were placed at the bottom to ensure that the sample is centered in the uniform magnetic field section for optimal measurements. Note: A Lexan shield is placed around the apparatus for safety purposes.

4.3.3 T_2 Subtraction and Hydrogen Signal Analysis

Finally, to quantify hydrogen interaction in the fluids, the Magritek Instrument processing software was used to subtract the raw NMR decay curve at each injection pressure from the baseline signal of the fluid without hydrogen. The software then processed the resulting difference into a T_2 distribution using an exponential decay fitting approach, providing hydrogen uptake as a function of pressure. The fit was checked to ensure the decay followed the expected exponential behavior, ensuring reliable results.

4.4 Results

4.4.1 Deuterated and DI water

Figure 4.2 presents NMR T_2 relaxation data of hydrogen in D_2O at various injection pressures. Since D_2O does not produce an NMR signal, only hydrogen in the gaseous phase (free phase) is detected. The free hydrogen phase exhibits T_2 relaxation times between 1 and 20 ms, with increasing pressure leading to a higher signal amplitude due to the greater hydrogen concentration. Additionally, a shift toward longer relaxation times is observed, suggesting enhanced intermolecular interactions at higher pressures. This linear behavior with pressure aligns with previously reported behavior for hydrogen (Ho et al. 2024, Dang et al. 2025, Mamoudou, Dang, et al. 2024) and other gases, such as bulk methane (Kausik et al. 2011, Gerritsma et al. 1971).

In contrast, **Figure 4.3** shows T_2 relaxation data for hydrogen in DI water, which exhibits significantly longer relaxation times (~3000 ms) compared to the free gas phase. Upon hydrogen injection at 500 psi, the water signal amplitude decreases slightly due to compressibility effects but remains relatively stable with increasing pressure up to 1500 psi. The mean T_2 values remain unchanged at ~3000 ms, indicating that the bulk properties of DI water, such as density and viscosity, are not significantly affected by hydrogen injection. This stability suggests minimal interaction between hydrogen and water molecules and confirms the limited solubility of hydrogen under these conditions.

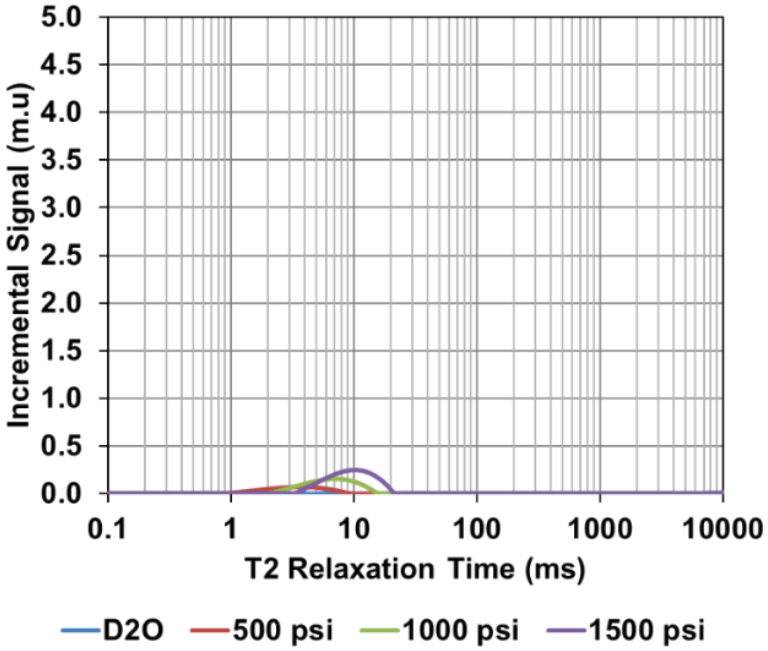


Figure 4.2 - T_2 relaxation during hydrogen injection into D_2O is shown as a function of pressure, highlighting the free gaseous hydrogen signal in machine units (m.u), relaxing within 1–20 ms over the experimental pressure range.

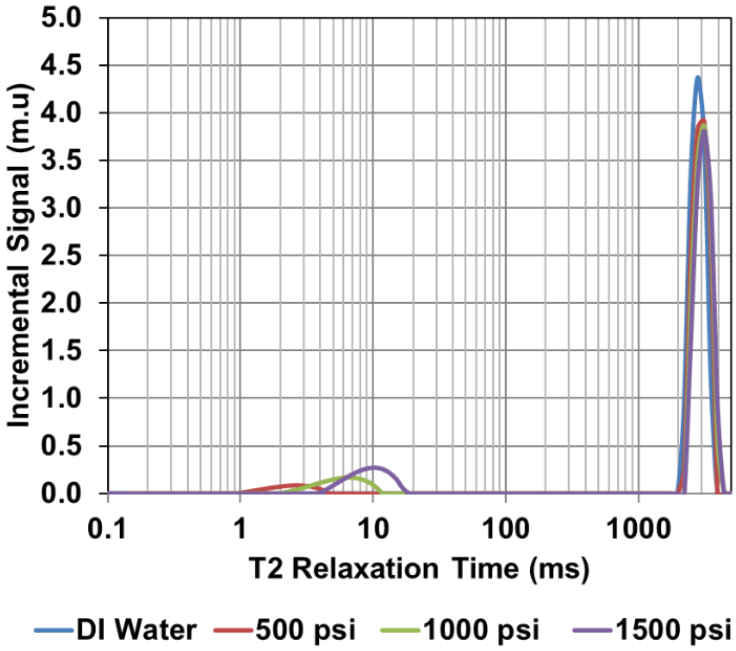


Figure 4.3 - T_2 relaxation during hydrogen injection into DI water is shown as a function of pressure, highlighting the presence of free hydrogen with relaxation times between 1–10 ms and bulk DI water at 3000 ms. The water signal decreases slightly due to compressibility but remains constant with pressure, with limited interaction with DI water.

4.4.2 Fluorinert

Figure 4.4 presents NMR data during H_2 injection into the fluorinert after background signal subtraction (i.e., the fluorinert without H_2), measured up to 1800 psi. The results reveal three distinct relaxation behaviors: a fast-relaxing signal (1–20 ms), attributed to free-phase hydrogen as observed in D_2O; a slow relaxation signal (2000–3000 ms), likely due to residual water in the system lines; and an intermediate relaxation signal (100–200 ms). This intermediate signal increases in amplitude and shifts slightly with pressure, similar to free hydrogen. However, its reduced mobility and relaxation time, 10 times slower than free H_2, suggest that it may correspond to hydrogen that is dissolved in the fluorinert.

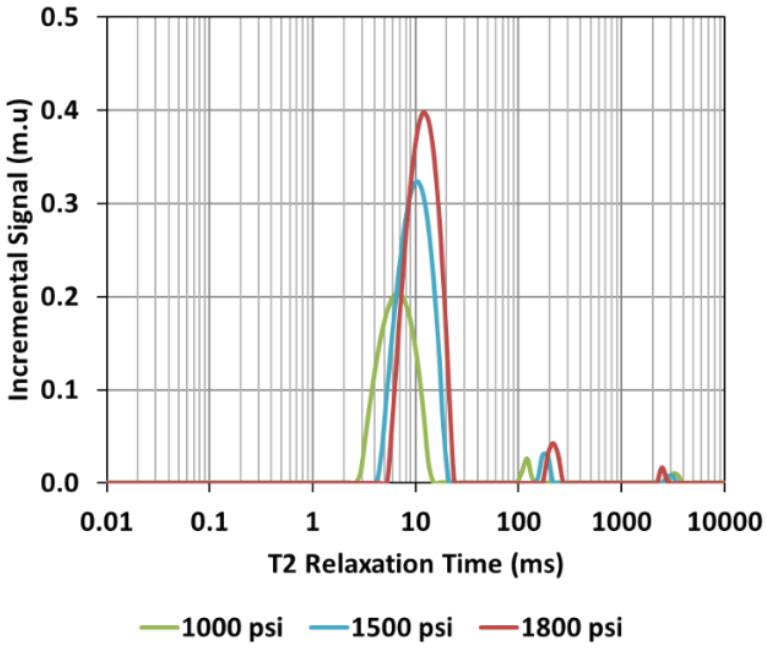


Figure 4.4 - T_2 relaxation data during H_2 injection into the fluorinert after baseline subtraction, showing free hydrogen (1–20 ms), an intermediate signal (100–300 ms) attributed to potentially dissolved hydrogen, and a slow relaxation signal (>1000 ms) corresponding to trace water. Note: The scale in this figure is smaller than in Figures 4.1 and 4.2 to improve visualization.

The intermediate signal, with values of 0.04, 0.06, and 0.1 m.u. at 1000, 1500, and 1800 psi, respectively, was converted to volume using the hydrogen index (HI) as a function of pressure

(**Figure 4.4**) and applying **Equation 4.3**. The HI was obtained from the National Institute of Standards and Technology (NIST) Handbook.

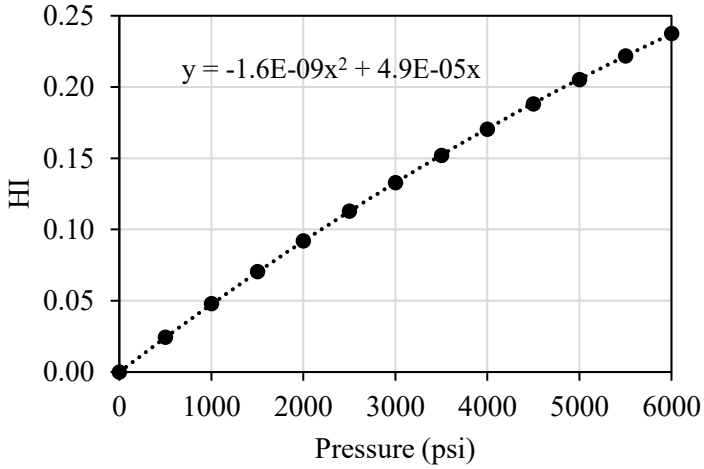


Figure 4.5 - HI for different injection pressure points at room temperature (NIST handbook).

$$V_{H_2} = \frac{NMR_{Signal}}{HI} * C \qquad 4.3$$

V_{H2} : H_2 volume (cc or mL)

C : calibration constant (cc/m.u)

NMR_{Signal} : signal amplitude (machine units)

HI: Hydrogen index (dimensionless)

The data indicate that this signal corresponds to 0.8–1.2 cc of H_2 per 20 cc of fluorinert dissolved between 500-1800 psi (or 4-6 cc of H_2 per 100 cc of fluorinert). Finally, visual observation (**Figure 4.6**) shows evidence of H_2 bubbles coming out of the solution post-injection, indicative that hydrogen could also be trapped rather than fully dissolved.

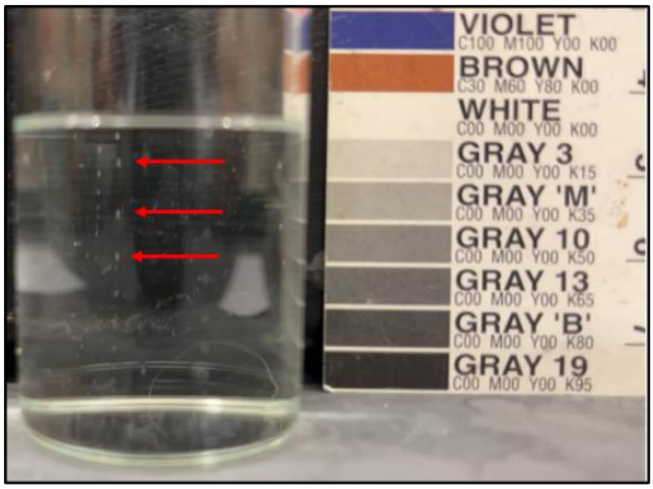


Figure 4.6 - Fluorinert post hydrogen injection showing hydrogen bubbles (red arrows) in solution. The image was taken post-experiment at ambient pressure.

4.4.3 Hydrocarbons

Dodecane oil was tested first to evaluate hydrogen interaction before analyzing the dead oil, as shown in **Figure 4.7A**. Being a single alkane, the T_2 relaxation distribution of C_{12} exhibits a sharp curve centered around 1000–2000 ms. In **Figure 4.7B,** after subtracting the C_{12} signal, only the free-phase hydrogen signal remains, with no intermediate T_2 signal such as in the fluorinert, suggesting minimal to no solubility of hydrogen in dodecane.

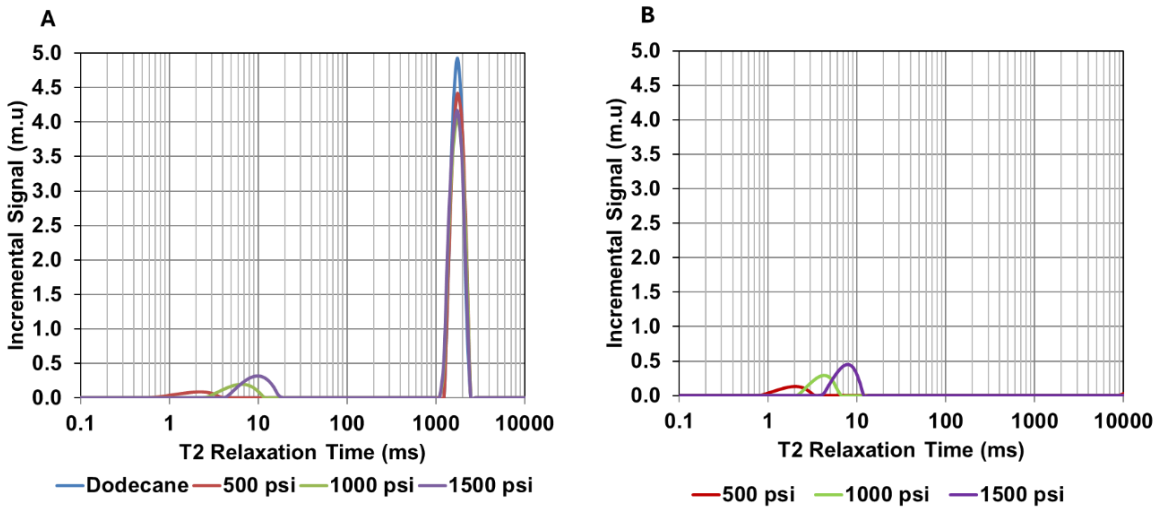


Figure 4.7 - T_2 relaxation data before (A) and after (B) dodecane subtraction is shown as a function of H_2 injection pressure. After subtracting the baseline dodecane signal in blue (1000–2000 ms), only the free H_2 signal remains between 1–10 ms, suggesting that no H_2 interaction with dodecane.

For dead oil, which contains a broader range of alkanes (C_9–C_{17}, **Figure 4.8**), the T_2 distribution is also broader, ranging from 35 to 4000 ms (**Figure 4.9A**). During hydrogen injection, the NMR distribution (**Figure 4.9B**) indicates that hydrogen remains exclusively in the free phase. No additional signal is observed, and the bulk dead oil signal remains unchanged (Figure 4.9B).

However, visual observations post-injection in the dead oil revealed some degree of gas trapping, as evidenced by visible bubbles (**Figure 4.10**). The less vigorous bubbling compared to the fluorinert can be attributed to the dead oil's higher viscosity, stronger molecular interactions, and complex hydrocarbon composition, which restrict hydrogen bubble mobility and promote localized gas trapping rather than rapid escape. In contrast, the lower viscosity and weaker intermolecular forces in fluorinert allow hydrogen to disperse more freely, resulting in faster bubble formation and release.

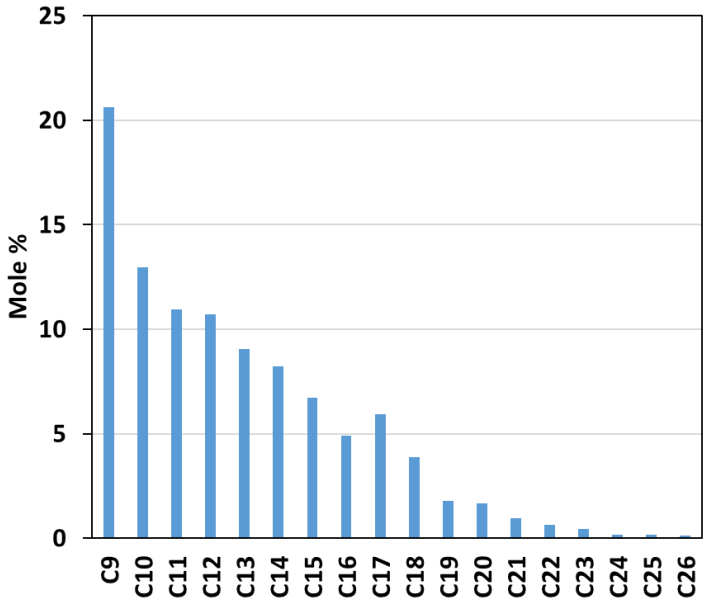


Figure 4.8 - Dead oil composition measured by gas chromatography showing a wide range of alkanes from C_9-C_{17}.

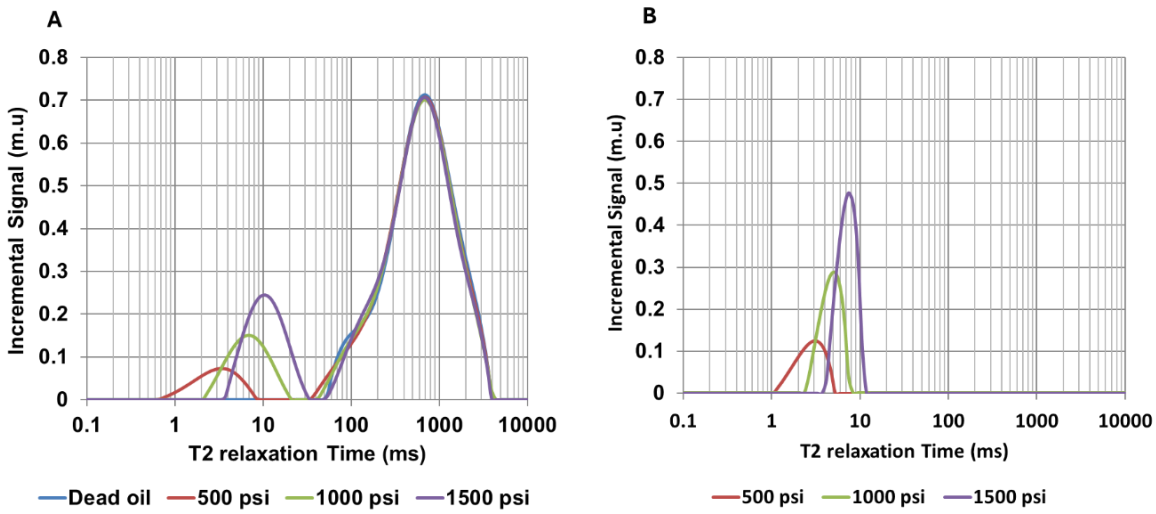


Figure 4.9 - T_2 relaxation data before (A) and after (B) Eagle Ford dead oil baseline subtraction are shown as a function of H_2 injection pressure. After subtracting the dead oil signal (35–4000 ms), only the free H_2 signal remains, indicating no interaction of H_2 with the oil.

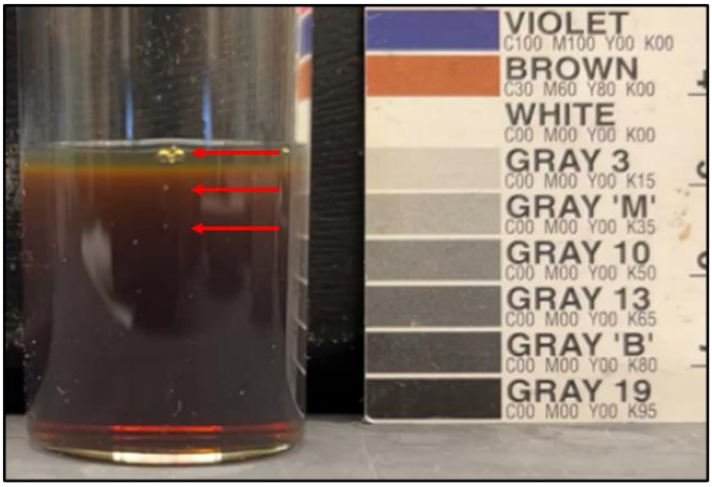


Figure 4.10 - Dead oil post hydrogen injection showing hydrogen bubbles (red arrows) coming out of the solution.

Finally, for the wax sample (**Figure 4.11**), after subtracting the wax baseline signal (0.1–300 ms), only free-phase hydrogen was detected, both through NMR measurements and visual observations.

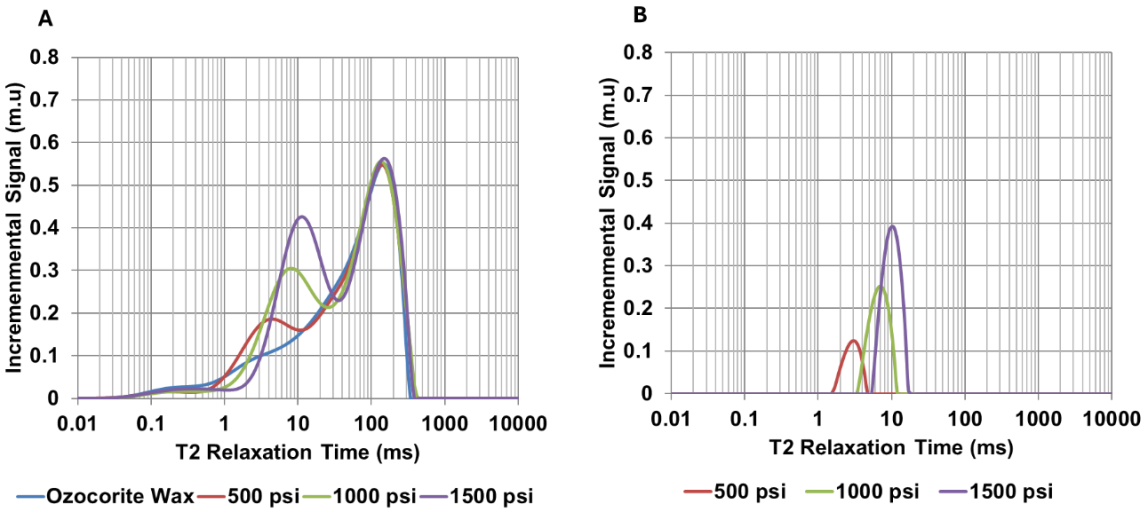


Figure 4.11 - T_2 relaxation data before (A) and after (B) subtraction of the ozokerite wax signal (0.1–300 ms) are shown as a function of H_2 injection pressure, indicating only free H_2 with no interaction with the wax.

4.5 Discussion

The results indicate that hydrogen predominantly remains in the free phase when in contact with DI water, exhibiting fast T_2 relaxation times (1–20 ms) after water signal subtraction. D_2O, used as a control fluid with a hydrogen index of zero, further confirms that free hydrogen exhibits short relaxation times.

For the fluorinert, the NMR data reveal an intermediate T_2 range (100–300 ms), which is 10 times slower than free hydrogen. This is interpreted as either dissolved hydrogen or trapped gas, as visually confirmed by post-injection bubble formation. While fluorinert fluids are generally considered inert, their low cohesive energy and high free volume may facilitate weak van der Waals interactions, leading to some degree of hydrogen retention. Therefore, when using this liquid as a confining fluid in core plug tests, some level of hydrogen interaction should be expected.

In organic fluids (dodecane, dead oil, and wax), only free hydrogen signals were detected, indicating limited molecular interaction under NMR. However, visual observation, post-injection

revealed hydrogen bubbles in dead oil, suggesting physical gas trapping rather than true dissolution. The distinction between these two behaviors lies in the NMR response: if hydrogen had truly dissolved at the molecular level, an intermediate T_2 relaxation time would be observed. Instead, the presence of only free hydrogen signals confirms that hydrogen remains in a separate gas phase. This suggests that in the dead oil, hydrogen is physically trapped rather than fully dissolved in the liquid phase. Ultimately, this trapped hydrogen remains producible after injection, as visually confirmed when pressure was released following the experiment. This interaction could become more significant in storage conditions with higher pressure and temperature. The solubility of hydrogen in crude oil can reach up to 0.8mol/kg at 380 °C and 10 MPa (Cai et al. 2001, Ji et al. 2013).

Overall, these findings demonstrate that hydrogen has limited solubility in our test conditions (**Figure 4.12**).

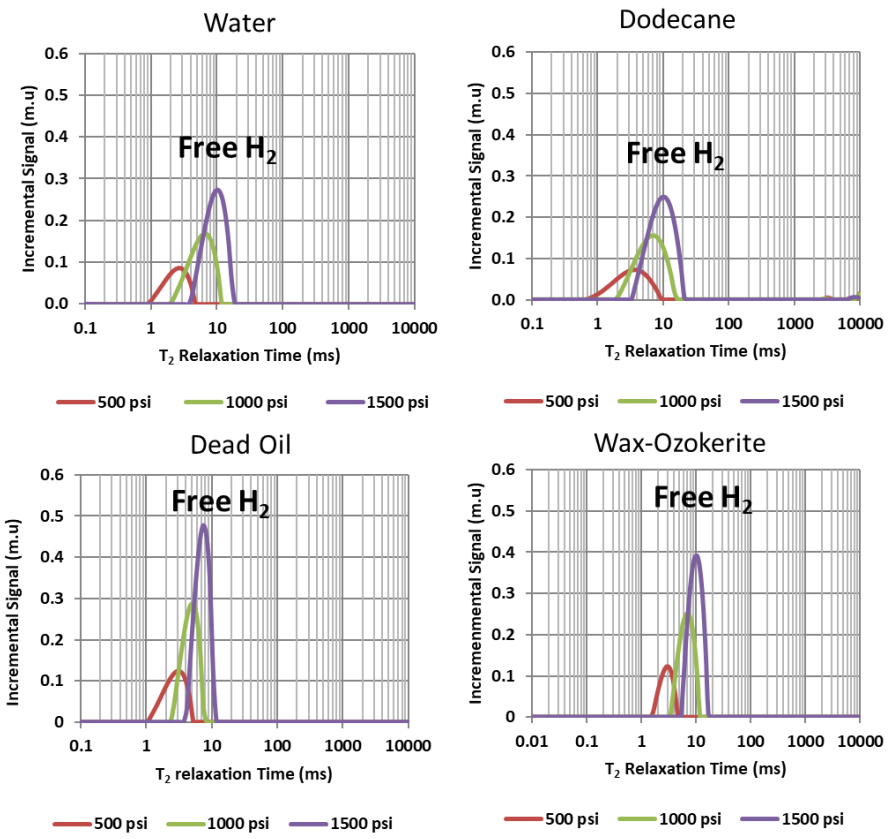


Figure 4.12 - Summary of hydrogen interaction in our study as a function of pressure after baseline subtraction. Only free hydrogen signals are detected, appearing within the 1–20 ms relaxation time window. While the NMR peak shapes vary across fluids, the total hydrogen signal remains relatively consistent. For example, at 1500 psi, the cumulative signal for all fluids ranges between 2.45 and 2.49 cc.

To build on these findings, future studies will investigate the impact of hydrogen in these fluids within porous media under NMR at higher pressures, making the results more applicable to storage conditions.

4.6 Conclusion

This study establishes a baseline for hydrogen interaction in organic reservoir fluids (dodecane, dead oil, and ozokerite wax) and inorganic fluids (D_2O and fluorinert) to support core plug measurements. Under the tested conditions, hydrogen remains primarily in the free phase in DI water and dodecane, while in dead oil, it is physically trapped as an immiscible gas phase. This

process is expected to be reversible and induce minimal loss during the production phase. Fluorinert exhibits both hydrogen molecular dissolution and hydrogen trapping around 4-6 ±0.02cc of H_2 per 100 cc of fluid, as indicated by an intermediate T_2 relaxation signal (100–200 ms) and visual bubbles post-injection. This finding suggests potential signal interference in core plug measurements under confining stress, requiring careful interpretation. Therefore, T_2 >300ms responses on saturated plug measurement will be removed from our analysis and considered as an artefact of the measurement.

The NMR methodology effectively distinguishes free-phase hydrogen from dissolved hydrogen using T_2 relaxation times and baseline signal subtraction, providing a useful proxy for evaluating hydrogen-fluid interactions. Although conducted at relatively low temperatures and pressures, these findings provide a first step toward understanding hydrogen interaction and retention in bulk fluids, which could serve as a guide for cushion gas selection. Future research will focus on hydrogen interactions in rock-saturated samples, enabling a more comprehensive assessment of storage behavior in porous media.

Chapter 5: Hydrogen Interaction in Cyclohexane Using NMR for Geostorage Application

5.1 Abstract

Understanding hydrogen dissolution and vaporization in liquid hydrocarbons is crucial for assessing loss in reservoir fluids during geostorage. Cyclohexane was used as a proxy to understand the vaporization and dissolution of hydrogen under NMR. This study investigates the interaction between hydrogen and cyclohexane under high-pressure (1500 psi) conditions using low-field NMR T_2 relaxation. Two experiments were conducted to analyze (1) hydrocarbon vaporization, by monitoring free hydrogen in the gas phase, and (2) hydrogen dissolution, by tracking T_2 shifts in bulk liquid cyclohexane over 32 days.

Results show that free hydrogen remained stable, confirming minimal vaporization, while dissolved hydrogen induced a progressive shift in T_2 relaxation, indicating increased molecular mobility and a 3.42% rise in hydrogen content, as measured by the hydrogen index (HI). The dissolution process exhibited three phases: minimal uptake (0–100 hours), active dissolution (100–600 hours), and equilibrium beyond 600 hours. The estimated solubility reached 1.42 cc of H_2 per 100 cc of cyclohexane.

NMR can be used to evaluate hydrogen interactions, including vaporization and solubility. This study establishes a basis for evaluating hydrogen interactions in reservoir fluids.

5.2 Introduction

Accurate data on hydrogen solubility and vaporization in geological reservoir fluids is essential for assessing hydrogen loss during underground storage. NMR T_2 relaxation has been shown to distinguish between free gaseous hydrogen ($T_2 < 100$ ms) and hydrogen dissolved in bulk fluid (T_2

= 1000–2000 ms) (Ho et al. 2024, Mamoudou, Dang, et al. 2024, Dang et al. 2025), providing a powerful tool for studying hydrogen behavior in liquid systems.

Among hydrocarbon solvents, cyclohexane serves as a suitable fluid system due to its well-characterized physical properties and a known hydrogen solubility of approximately 0.1cc of H_2 per cc of cyclohexane at room temperature and atmospheric pressure (Kruyer and Nobel 1961). However, direct NMR-based measurements of hydrogen dissolution and phase behavior in cyclohexane remain limited, with most studies relying on conventional solubility methods. Traditional techniques for determining gas solubility in liquids, such as saturation and stripping methods (Markham and Kobe 1941, Brunner 1985, Gao et al. 1999), are effective but often time-intensive and require specialized apparatus. To overcome these limitations, this study employs low-field NMR T_2 relaxation to analyze hydrogen interaction in cyclohexane at high pressure.

This approach provides precise insights into hydrogen dissolution and vaporization, establishing a foundation for future core plug measurement. Given that T_2 relaxation in low-viscosity fluids is inversely proportional to viscosity (Coates et al. 1999) NMR offers a practical method for evaluating hydrogen behavior in liquid environments relevant to subsurface storage applications.

5.3 Theory and/or Methods

Two experiments were conducted to evaluate the behavior of free hydrogen and hydrogen dissolved in cyclohexane at a constant pressure of 1500 psi using a 2 MHz Magritek NMR instrument with a Daedalus® core holder (**Figure 5.1**).

In the first experiment, hydrocarbon vaporization was studied by placing 20 cc of cyclohexane in the Daedalus cell, ensuring that the hydrogen-cyclohexane interface was positioned below the NMR magnetic field. This configuration allowed for the selective analysis of gaseous (free)

hydrogen. In the second experiment, hydrogen dissolution was investigated by filling the cell with approximately 70 cc of cyclohexane and positioning the hydrogen-cyclohexane interface above the NMR magnetic field's sweet spot, focusing on hydrogen dissolution in cyclohexane. To minimize dead volume, glass beads (which produce no detectable NMR signal) were added to the cell.

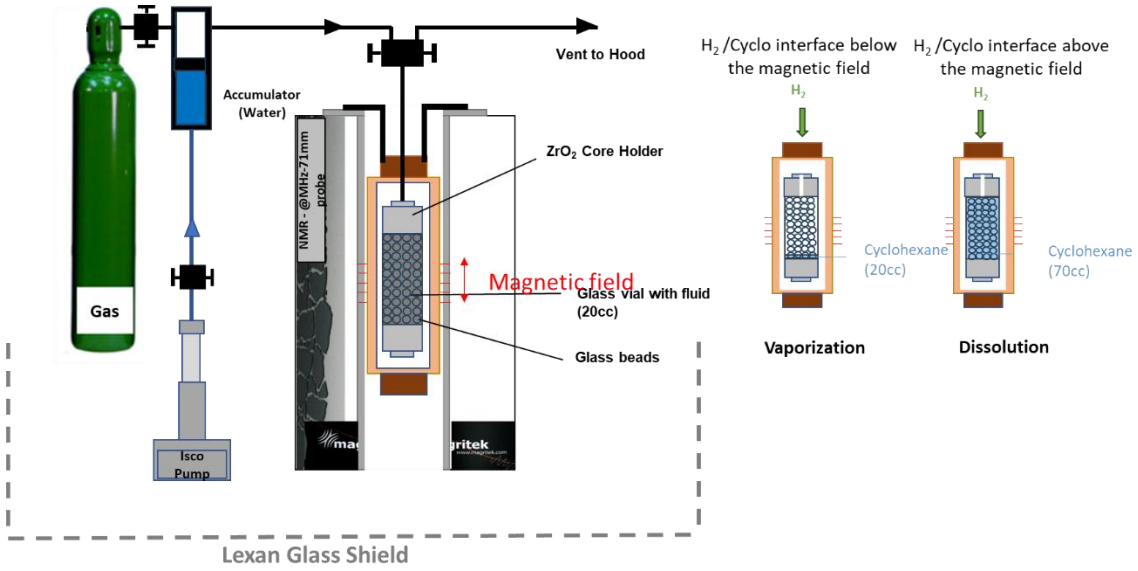


Figure 5.1 - Experimental schematic illustrating the vaporization and dissolution experiments with cyclohexane. The ZrO_2 cell, filled with cyclohexane, is positioned inside the NMR instrument. In the first experiment, the free gaseous hydrogen signal is monitored to determine vaporization of cyclohexane, while in the second experiment, the bulk liquid cyclohexane is monitored to assess hydrogen dissolution.

5.4 Results

5.4.1 Hydrogen vaporization

Figure 5.2 shows the T_2 relaxation time distribution from the vaporization experiment conducted at 1500 psi. Two main signals are evident: the signal around 10 ms corresponds to the free hydrogen and the signal, between 2000 and 3000 ms, represents the bulk liquid cyclohexane located at the bottom of the experimental cell (see chapter 4). Over three days, the cumulative signal (free hydrogen and cyclohexane) remains stable, as indicated by the unchanged cumulative

signal of approximately 3.0 ± 0.1m.u., confirming no increase in free gas volume and no vaporization of cyclohexane.

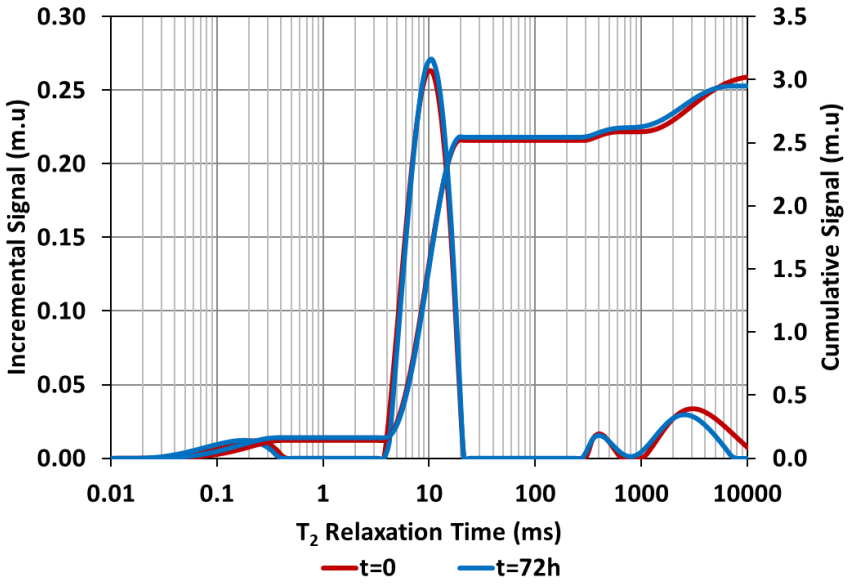


Figure 5.2 - T_2 relaxation data during hydrogen injection at 1500 psi in cyclohexane showing minimal change in free hydrogen signal (10 ms) after 3 days.

Using Equation 4.3 the free hydrogen and bulk cyclohexane volume is calculated on **Figure 5.3.** This figure confirms that the free hydrogen volume remains constant around 36.5±0.5cc and the bulk cyclohexane volume below 1cc.

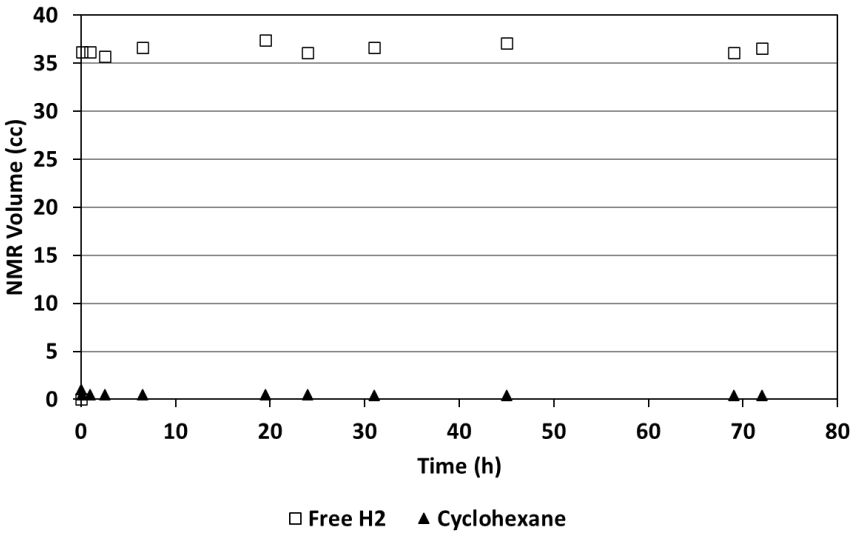


Figure 0.3 - Free hydrogen (T_2=10 ms) and bulk cyclohexane (T_2= 2000-3000 ms) volume over time showing no changes in volume at 1500 psi.

5.4.2 Hydrogen dissolution

Figure 5.4 presents the T_2 distribution of cyclohexane exposed to hydrogen over 30 days at 1500 psi. Unlike the first experiment, where the T_2 distribution remained unchanged, this experiment shows significant changes in shape, amplitude, and average T_2 mean over time.

Upon hydrogen injection, the T_2 curve initially broadens during the first 100 hours, followed by a gradual narrowing between 100 and 768 hours. After 51 hours, the amplitude increases, and the T_2 values shift from 1660 ms to 2780 ms, eventually stabilizing after 600 hours (25 days). The cumulative signal increases from 29.22 to 30.31 ± 0.02 m.u after 32 days (768 hours), confirming hydrogen dissolution in cyclohexane. This shift suggests that the newly formed cyclohexane-hydrogen mixture is less viscous and more mobile due to the presence of dissolved hydrogen.

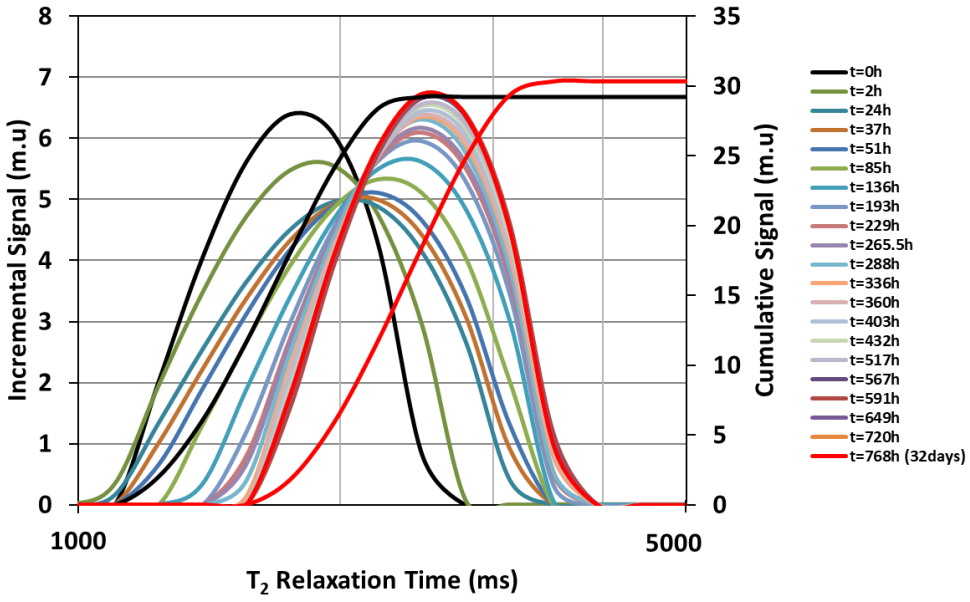


Figure 0.4 - T_2 relaxation data during hydrogen injection at 1500 psi in cyclohexane as a function of time, showing a T_2 shift toward longer times as hydrogen dissolves into cyclohexane.

The extent of hydrogen dissolution is further illustrated in **Figure 5.5**, which plots the HI over time. The equation 4.3 can be modified to account for the density change over time due to hydrogen at 1500 psi.

$$HI = (\frac{NMR_{Cyclo}}{NMR_{water}})_{14psi}(\frac{\rho_{cyclo}}{\rho_{water}})_{1500psi} \quad \text{Equation 5.1}$$

Where NMR_{Cyclo} (cm^3) and NMR_{water} (cm^3) represent the NMR T_2 signal of cyclohexane and water measured at ambient pressure with the same amount of volume in the cell, and ρ_{cyclo} (g/cm) and ρ_{water} (g/cm) denote the density of cyclohexane and water at 1500 psi, as obtained from the NIST handbook.

The data reveal three distinct phases: minimal dissolution (0–100 hours), active dissolution (100–600 hours), and equilibrium, where dissolution ceases. Over the 32 days (768 hours), the HI increases from 0.91 to 0.94, reflecting the gradual uptake of hydrogen by cyclohexane by 3.42%. Ultimately, the solubility reached 1.42 cc of H_2 per 100 cc of cyclohexane.

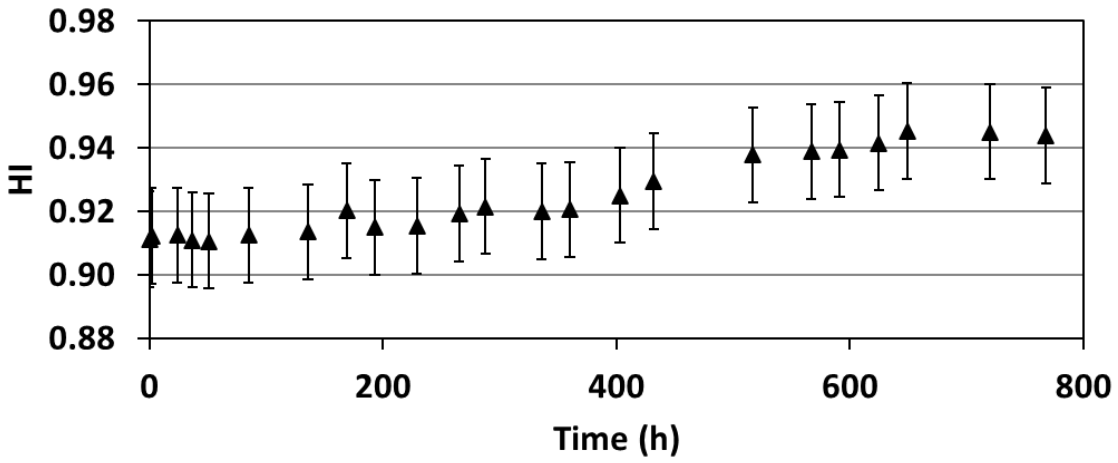


Figure 0.5 - HI of cyclohexane over 32 days following hydrogen injection at 1500 psi, showing an increase in hydrogen nuclei content from 0.91 to 0.94.

5.5 Discussion

The results from the NMR analysis provide insights into hydrogen dissolution and vaporization behavior in cyclohexane at 1500 psi. The first experiment (Figure 5.3) demonstrated that free hydrogen volume remained stable over time, confirming the absence of measurable hydrocarbon loss to the gas phase.

Conversely, the hydrogen second experiment focusing on the bulk cyclohexane (Figure 5.5) revealed notable changes in T_2 relaxation behavior, indicating hydrogen uptake into the liquid phase. The T_2 distribution initially broadened within the first 100 hours, followed by a narrowing trend between 100 and 768 hours, suggesting progressive hydrogen dissolution into the liquid phase. The increase in cumulative signal (from 29.22 to 30.31 ± 0.02 m.u.) and the shift in T_2 values (from 1660 ms to 2780 ms) confirm that dissolved hydrogen alters the relaxation dynamics of cyclohexane, likely due to changes in viscosity and molecular mobility.

The hydrogen index analysis (Figure 5.5) further supports these findings. Over 32 days, the HI increased from 0.91 to 0.94, reflecting a 3.42% rise in hydrogen content and a solubility of 1.42 cc of H_2 per 100 cc of cyclohexane. This indicates continuous dissolution until equilibrium is reached. The dissolution process occurs in three distinct phases: minimal dissolution from 0 to 100 hours, active dissolution between 100 and 600 hours, and an equilibrium phase beyond 600 hours. These phases illustrate a time-dependent hydrogen uptake process.

Additionally, the results show that low-field NMR T_2 relaxation is effective in quantifying hydrogen solubility and phase interactions in liquid systems. However, while T_2 relaxation provides insights into hydrogen solubility, it is less sensitive to fluid viscosity changes and may not fully capture molecular diffusion and phase behavior (Coates et al. 1999). To overcome these

limitations, T_1 relaxation measurements, which are more sensitive to viscosity and molecular interactions, will be incorporated in future studies to improve the quantification of hydrogen dissolution dynamics in cyclohexane

5.6 Conclusion

This study used low-field NMR T_2 relaxation to investigate hydrocarbon vaporization and dissolution in bulk cyclohexane liquid under pressure. Results confirmed that free hydrogen remained stable, indicating minimal vaporization, while dissolved hydrogen caused a measurable shift in T_2 relaxation, reflecting increased molecular mobility. The HI increased by 3.42% over 32 days, revealing a progressive dissolution process with three distinct phases: minimal uptake, active dissolution, and equilibrium. These findings demonstrate NMR's effectiveness in characterizing hydrogen interactions and provide a foundation for future studies on hydrogen behavior in reservoir fluids and core plugs.

Chapter 6: Evaluation of Hydrogen Storage in Partially Saturated Sandstone and Shales using NMR.

6.1 Abstract

The growing use of hydrogen as a clean energy carrier has increased interest in underground hydrogen storage as a large-scale, long-term solution. Effective storage depends on selecting reservoirs and caprock with minimal leakage risk and favorable geochemical properties. This chapter examines the hydrogen storage mechanism and mobility in partially saturated sandstone and organic-rich shales using NMR T_2 relaxation.

For shales, NMR experiments at 5000 psi on dried Eagle Ford, Duvernay, and Marcellus formations showed that H_2 occupied the entire pore network, regardless of thermal maturity, with T_2 relaxation times matching the bulk hydrogen response, confirming free-phase hydrogen as the dominant storage mechanism. Minimal hysteresis as a function of pressure indicated negligible hydrogen loss in contact with the caprock under our test conditions.

In partially saturated Berea sandstone, the hydrogen-filled pore volume matches the calculated helium pore volume. Also, no evidence of hydrogen dissolution in water was observed (i.e., no intermediate T_2 relaxation between 100–300 ms). The absence of significant hysteresis suggests full recovery and minimal capillary trapping in our test conditions.

6.2 Introduction

The technical and economic feasibility of hydrogen geostorage depends on factors such as gas storage volume, reservoir and caprock integrity, and potential geochemical interactions (Zivar et al. 2021). Hydrogen can interact with geological formations through various mechanisms, including changes in mineral wettability (Iglauer et al. 2021, Zeng et al. 2022, Higgs et al. 2022)

and mineral dissolution (Bensing et al. 2022, Al-Yaseri et al. 2023). In deep radioactive repository, redox reactions in shales, such as Fe^{3+} reduction to Fe^{2+}, can lead to the transformation of pyrite into pyrrhotite (Truche et al. 2010, Truche et al. 2013). These processes may affect hydrogen storage volume, induce H_2S production, and alter pore fluid composition, potentially compromising reservoir integrity (Flesch et al. 2018). However, recent studies suggest that abiotic geochemical reactions in sandstone reservoirs pose a lower risk to hydrogen storage (Yekta et al. 2018, Hassanpouryouzband et al. 2022). Despite this research on hydrogen reactivity, research on hydrogen storage mechanisms and storage capacity in reservoir rocks is limited.

Extensive research has been conducted on natural gas (such as methane) storage in porous and nanoporous geological formations, under NMR particularly in bulk (Gerritsma et al. 1971; Akkurt et al. 1996) and in nanoporous shales (Sigal et al. 2011; Kausik et al. 2011; Tinni et al. 2015). In nanoporous shales, gases like methane exist both as an adsorbed phase on pore surfaces and as free gas within the pore interior at high pressures (Kausik et al. 2012).

However, studies on hydrogen storage mechanism using NMR under geostorage conditions are scarce. Recent work by Ho et al. (2024) demonstrated that hydrogen in dried sandstone behaves as free hydrogen, as indicated by an increase in amplitude and a shift to longer T_2 relaxation times.

This study extends the previous work and investigates hydrogen storage mechanisms in both caprock and partially saturated reservoir rocks. First, we examine hydrogen storage in shales of varying thermal maturity, including Eagle Ford and Duvernay from the oil window (O) and Marcellus from the gas window (G), to assess caprock interactions. We then evaluate hydrogen storage in sandstone as a function of water saturation, using it as a proxy for an aquifer reservoir.

6.3 Experimental Methods

6.3.1 Sample description and experimental apparatus

The experimental method involved using NMR T_2 relaxation to analyze hydrogen storage behavior in organic-rich shales and partially saturated sandstones. Shale core plugs (approximately 2.5 inches long and 1 inch in diameter) from the Eagle Ford (O) and Duvernay (O) formations along with a Marcellus (G) and Berea sandstone, were prepared by Soxhlet extraction with a toluene-methanol (80:20) mixture, followed by drying at 100°C. Total porosity, mineralogy, and organic content were determined through helium pycnometry and Fourier-transform infrared spectroscopy. Thermal maturity (Tmax) was measured using HAWK® **(Table 6.1).**

Table 6.1 - Petrophysical sample description.

Sample	Porosity (%)	TOC (wt%)	Tmax (°C)	Total Clays (wt%)	Total Carbonates (wt%)	Quartz + Feldspars (wt%)	Other Minerals (wt%)
Berea SS	21	0	N/A	10	0	90	0
Eagle Ford	5.1	4.9	455	16	62	13	8
Duvernay	5.8	5	460	43	0	42	15
Marcellus	4.3	11.5	492	24	67	8	1

NMR signals were recorded in real-time during hydrogen injection and withdrawal to evaluate hydrogen uptake and storage mechanisms. The NMR T_2 relaxation distribution was measured using a 2 MHz NMR Magritek Instrument RCA with a Carr–Purcell–Meiboom–Gill (CPMG) sequence. The hydrogen injection tests were conducted inside a zirconium dioxide (ZrO_2) NMR-transparent pressure cell at confining pressure up to 5000 psi, while maintaining an effective pressure of 1250 psi **(Figure 6.1). Figure 6.2** shows a photograph of a jacketed Berea sandstone in PTFE shrink wrap before placement inside the ZrO_2 . A fluorinert HT-230 was used as the confining fluid. For each pressure, the injection rate was around 1 cc/min. Hydrogen was injected at both ends of the sample to ensure no pore fluid displacement. For shale samples, T_2 relaxation measurements were collected every 24 hours to ensure pressure equilibrium, whereas, for

sandstone samples, measurements were taken every hour. Nitrogen gas was used to purge the system before and after each experiment.

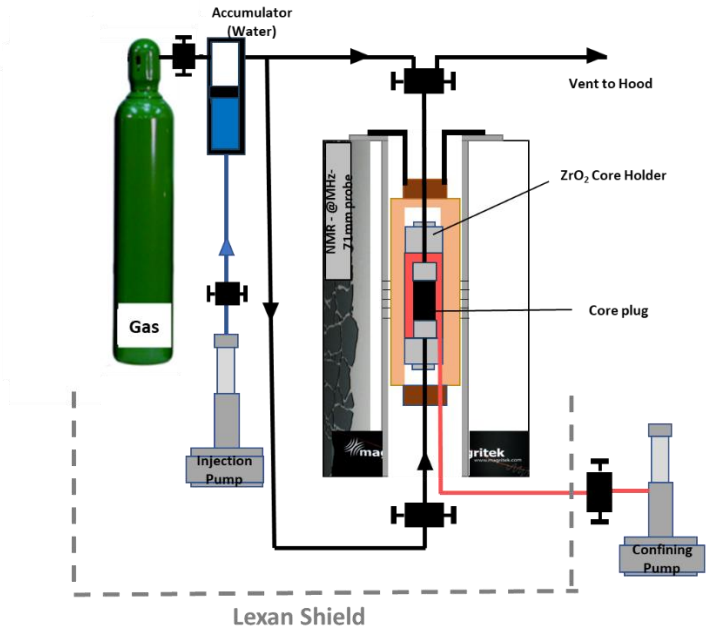


Figure 6.1 - General NMR experimental apparatus. The plug sample is placed inside an NMR transparent ZrO_2 pressure cell, placed within a 2 MHz NMR spectrometer. Hydrogen is compressed using a Teledyne Isco pump filled with water inside an accumulator. Fluorinert is used in a second pump to supply confining pressure.

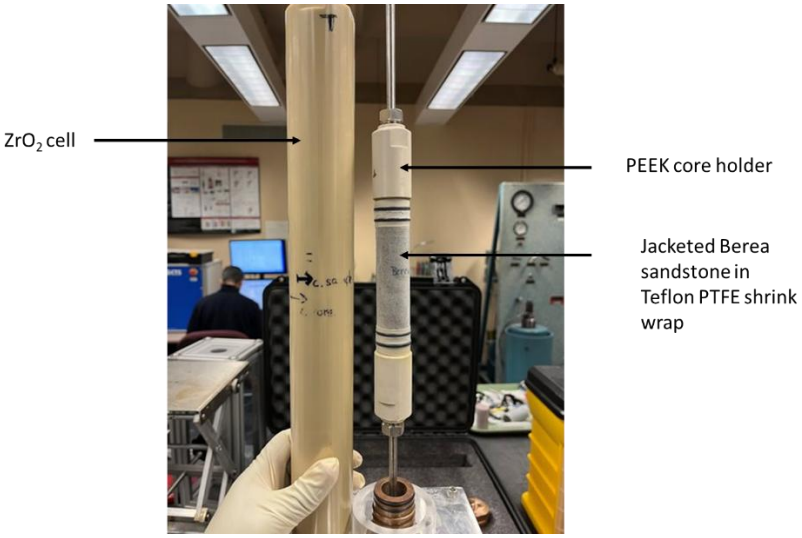


Figure 6.2 - Jacketed Berea sandstone positioned between two PEEK (Polyether Ether Ketone) core holders. The sample is wrapped in shrink-fit Polytetrafluoroethylene (PTFE) before assembly inside the ZrO_2 cell.

6.3.2 Baseline signal subtraction

Since the hydrogen signal is of interest, a baseline NMR measurement was recorded at 1250 psi confining pressure before injection to capture signals from unconnected pores, hydroxyl groups in clays, and bound fluids in shales, as well as initial water in sandstone. During the experiment, this baseline was subtracted to isolate the NMR T_2 relaxation response of hydrogen from background signals using Magritek RCA processing software. At each pressure, the decay curve without hydrogen was removed from the raw NMR decay, and the resultant signal was inverted to generate the new T_2 distribution. This approach ensured that only hydrogen gas relaxation responses were analyzed, distinguishing free-phase hydrogen from other storage mechanisms.

6.4 Results

6.4.1 Free hydrogen signal

The NMR T_2 distribution of bulk hydrogen was first measured at pressures up to 1500 psi by Ho et al. (2024) (**Figure 6.3**) to characterize its relaxation behavior. Results showed that bulk hydrogen has a T_2 relaxation time ranging from 1 to 20 ms, significantly shorter than that of water or hydrocarbons (1000–2000 ms, Chapter 3). As pressure increased, the signal amplitude increased due to the higher hydrogen molecule concentration, and the T_2 mean shifted to higher values, indicating stronger intermolecular interactions. These findings are consistent with previous studies on bulk methane (Kausik et al. 2011), where increasing pressure leads to greater molecular density and longer relaxation times, due to spin rotation mechanism.

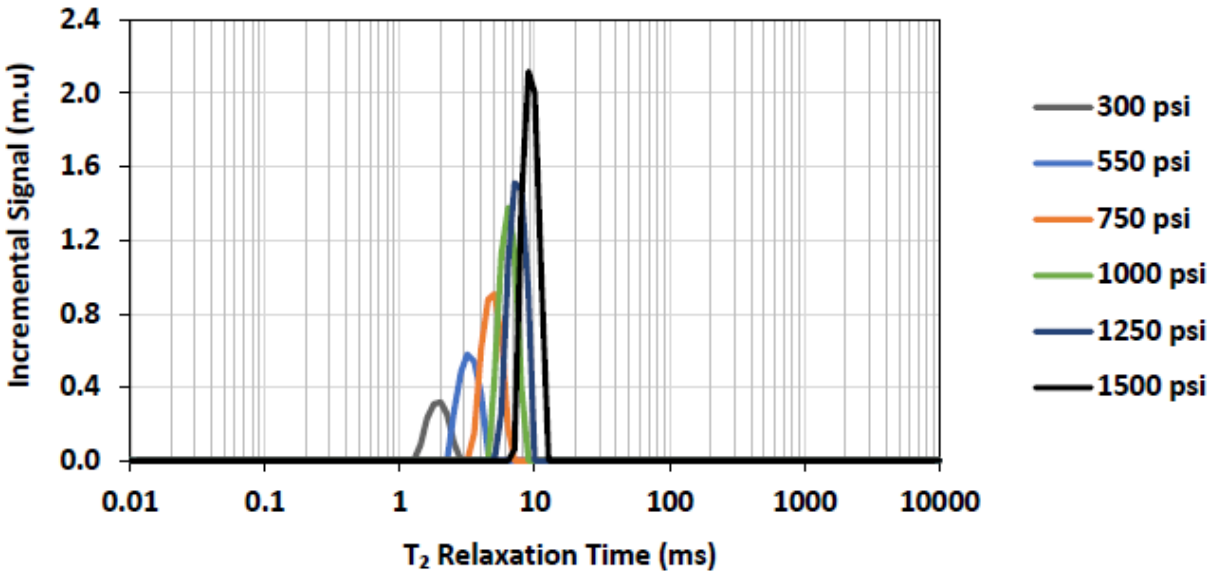


Figure 6.3 - NMR T_2 relaxation of free hydrogen at room temperature at different pressures up to 1500 psi (Ho et al. 2024).

6.4.2 Hydrogen in shales

When hydrogen is injected into shales (**Figure 6.4**), its behavior varies depending on the formation. In the Eagle Ford and Duvernay, hydrogen exhibits an increase in amplitude and a shift toward higher relaxation times with increasing pressure, behaving similarly to free hydrogen. Moreover, the T_2 range for these samples (2–30 ms) is consistent with that of free gases relaxation time.

In contrast, the Marcellus shale displays a reduced T_2 distribution (0.05 to 20 ms) and forms two distinct peaks, where the T_2 amplitude increases without any shift to longer T_2 with pressure. This behavior is likely attributed to the presence of sub-nanoscale pores. Previous work on methane in nanoporous Vycor glass (Song and Kausik 2019) has shown that in nanopores the methane signal amplitude increases without a shift in T_2 because the dominant relaxation mechanism of methane gas confined in nm-sized pores is surface relaxation rather than spin rotation. Research (Curtis et

al. 2011, Sinha 2017) has shown that gas shales such as Marcellus can contain pores smaller than 10 nm.

Additionally, when hydrogen signal data is converted to hydrogen-occupied porosity using the HI at 5000 psi (Equation 4.1 and 4.2) the values align closely with helium porosity (**Figure 6.5**), confirming that hydrogen fully occupies the available pore space in the shale samples. Interestingly no additional porosity was observed with hydrogen in all three shales, suggesting minimal to no adsorption of hydrogen, or adsorption signal was below the NMR detection threshold.

Furthermore, minimal to no hydrogen loss is observed due to hysteresis (**Figure 6.6**) for all shales, suggesting that hydrogen retention in the shales is negligible.

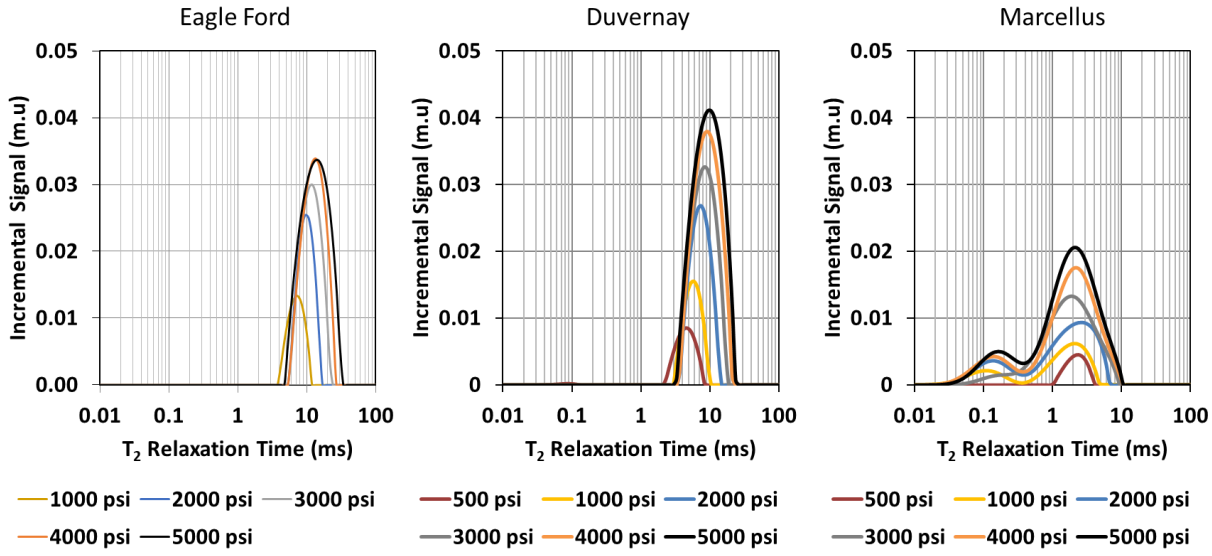


Figure 6.4 - NMR T_2 distribution of H_2 in Eagle Ford, Duvernay and Marcellus. The Eagle Ford and Duvernay show similar responses to bulk hydrogen, however, for the Marcellus, from the gas window, relaxation distribution split into 2 peaks, which could be due to the presence of sub-nanometer pores.

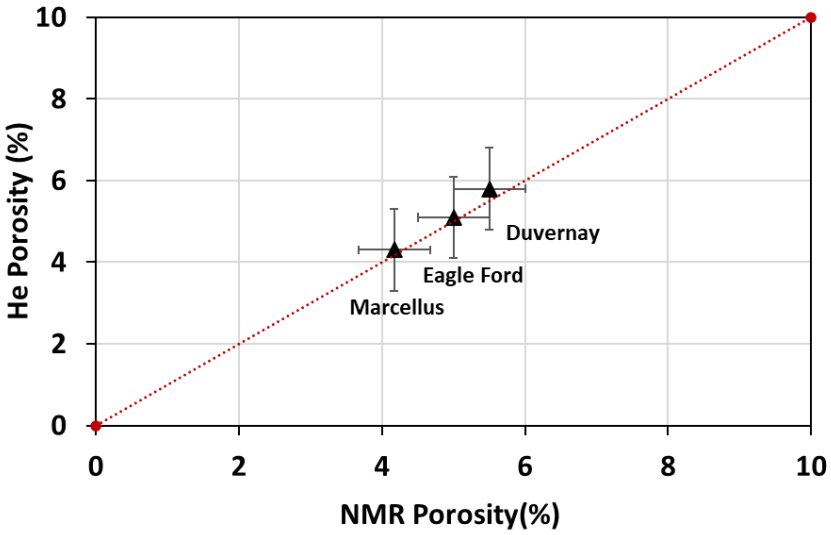


Figure 6.5 - H_2 porosity measured by NMR (5000 psi) comparison with helium porosity. Good agreement is observed between the H_2 occupied porosity and helium porosity, showing that hydrogen can fill all empty pore space.

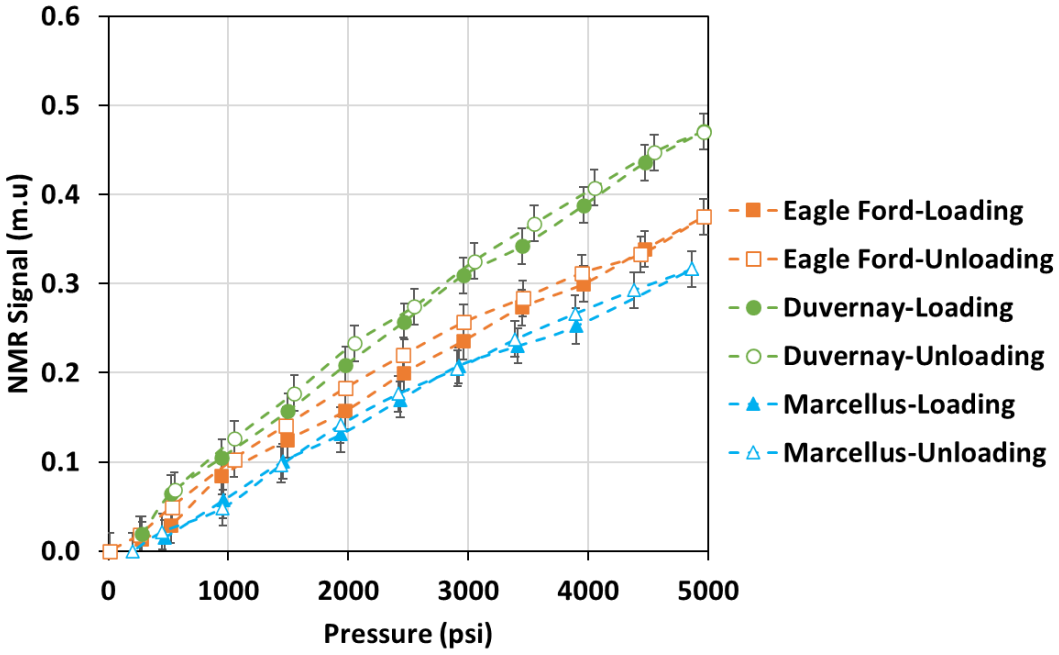


Figure 6.6 - H_2 intake during loading and unloading in Eagle Ford, Duvernay, and Marcellus shales up to 5000 psi. The results show minimal to no hysteresis.

6.4.3 Hydrogen in sandstones

Hydrogen injection into partially saturated Berea sandstone was conducted to evaluate the influence of water saturation (Sw) on storage capacity at 30% and 80%. **Figure 6.7** presents the NMR T_2 distribution of water within the Berea pore volume at different saturation levels. Notably, the signal for the dry sample is negligible, indicating an insignificant contribution of clay protons (or hydroxyl groups).

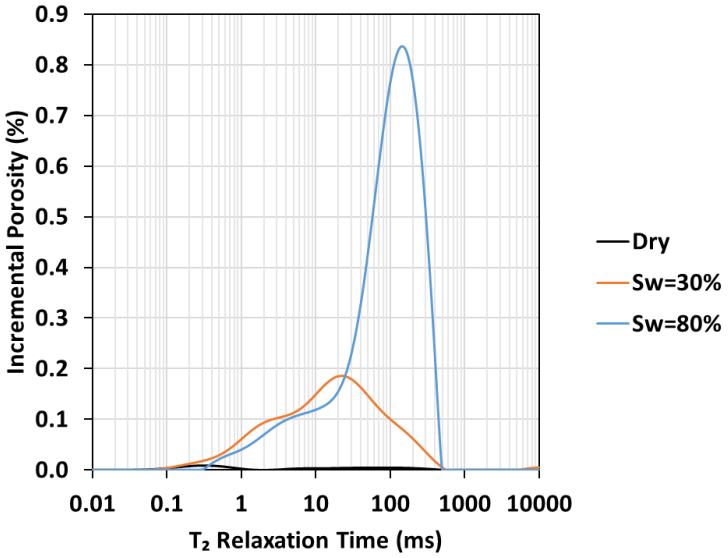


Figure 6.7 - NMR T_2 relaxation for the Berea sandstone at dried and partially saturated conditions.

When hydrogen is injected into Berea (**Figure 6.8**), it behaves as bulk hydrogen, regardless of Sw, like the behavior observed in bulk hydrogen Figure 6.3. With increasing pressure, the T_2 amplitude increases, and the relaxation times shift toward higher values. Additionally, hydrogen amplitude decreases with increasing Sw at each pressure point. This effect is more pronounced at higher Sw, where most of the pore volume is occupied by water as the wetting phase, leaving less space for H_2 storage. Also, at high Sw, the presence of water shifts the average T_2 mean toward shorter times. For instance, at 5000 psi, the T_2 mean decreases to 10 ms, compared to 30 ms for the dry and Sw = 30% states, suggesting that water-filled pores restrict hydrogen access and mobility.

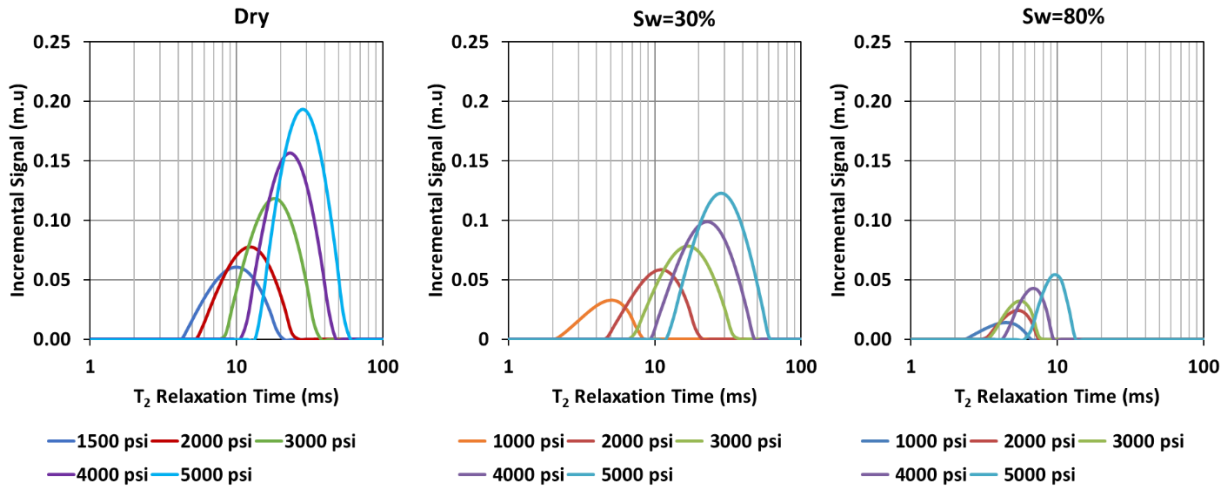


Figure 6.8 - NMR T_2 distribution of H_2 in Berea at different saturations (dry, sw=30% and Sw=80%).

When the T_2 data is converted to hydrogen-filled porosity at 5000 psi in **Figure 6.9**, the values closely match the available porosity from the calculated helium pycnometry. This indicates that hydrogen fills the empty pore space regardless of water saturation, with the plot clearly showing a linear relationship between storage capacity and empty pore space.

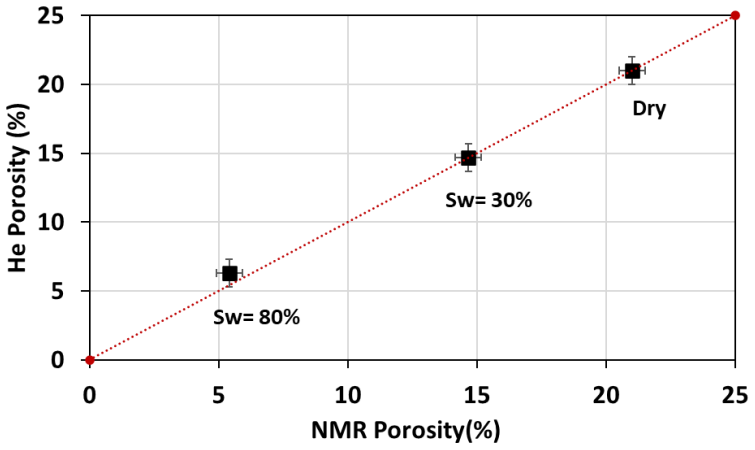


Figure 6.9 - Comparison between H_2 NMR measured porosity (at 5000 psi) with calculated helium porosity. NMR-measured porosity matches helium porosity. Note: Helium porosity was measured on the sample in a dried state only.

Finally, **Figure 6.10** shows the NMR response during the loading and unloading phases in dry and SW=80% conditions. Notably, no significant hysteresis was observed during withdrawal (**Figure 6.11**), indicating that hydrogen can be fully recovered without evidence of trapping or capillary retention in partially saturated sandstone.

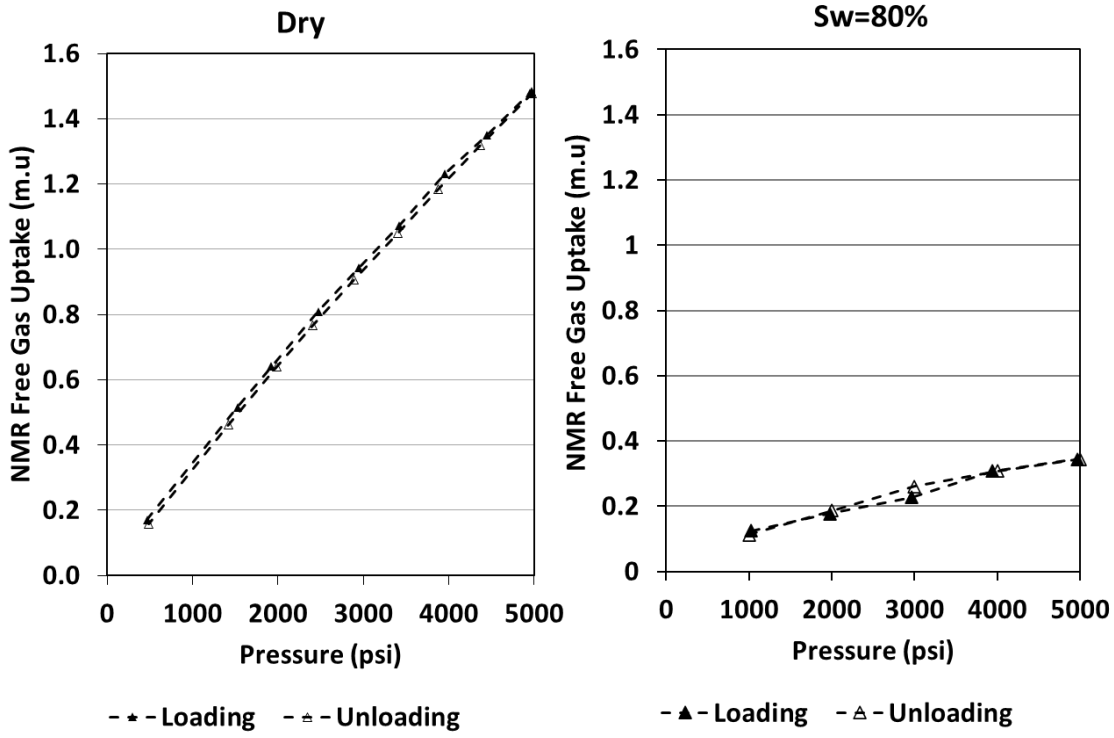


Figure 6.10 - H_2 intake between loading and unloading H_2 into dried and partially saturated (Sw = 80%) Berea sandstone. Insignificant hysteresis is observed regardless of water saturation.

6.5 Discussion

The results indicate that NMR can be used to evaluate storage mechanisms and capacity in shales and partially saturated sandstone with water. In all rocks studied, hydrogen behaves as a free phase, irrespective of shale organic content and maturity, and brine saturation in sandstone, with bulk relaxation dominating. An excellent match was observed between the hydrogen measured porosity at 5000 psi and helium porosity, suggesting minimal to no excess hydrogen due to adsorption in shales.

In the Marcellus shale, however, the T_2 distribution does not show the free hydrogen signature (i.e., increased amplitude and a shift to longer relaxation times). Its absence is attributed to the presence of sub-nanopores, where surface relaxation dominates. Furthermore, the results show insignificant hysteresis for all samples, indicating that hydrogen can be fully recovered after injection in aquifers or depleted gas reservoirs with low water saturation. A recent molecular modeling study (Kim et al. 2025) confirms the limited diffusivity of hydrogen through caprock, with diffusivity on the order of 10^{-7} m^2/s—only marginally faster than gases such as CO_2. Considering that reservoir caprocks have retained methane and other hydrocarbons for millions of years, these findings are promising and support the effective containment of hydrogen in depleted oil and gas reservoirs. However, the biotic and abiotic geochemistry of hydrogen may pose concerns (Amigáň et al. 1990, Panfilov 2010, Truche et al. 2010), and the results presented in this study underscore the need for further investigation.

6.6 Conclusion

NMR T_2 relaxation was successfully employed to evaluate hydrogen storage behavior in both shales and sandstones under reservoir-relevant conditions. The results demonstrate that NMR T_2 relaxation effectively captures hydrogen behavior in porous media. In the shale samples (Eagle

Ford, Duvernay, and Marcellus), hydrogen remained entirely in the free phase, occupying the full pore network with no evidence of interaction or trapping, regardless of thermal maturity. In the Berea sandstone, the measured hydrogen-filled pore volume matched the helium porosity, confirming complete pore access. No hydrogen dissolution in water was observed under the test conditions. Across all cases, no significant hysteresis was detected between loading and unloading, indicating efficient hydrogen mobility and full recovery potential. These findings collectively support the suitability of these formations for underground hydrogen storage.

General Conclusion and Recommendations for Future Work

NMR has been demonstrated to be an effective tool for characterizing pore structure, fluid behavior, and recovery mechanisms in subsurface systems. In the context of EOR, NMR provides a practical method to evaluate and compare reservoir candidates for HnP processes by directly measuring oil and water. For CO_2 storage applications, NMR enables the assessment of tortuosity and pore structure alterations in cements and caprocks under storage conditions. For H_2 storage, NMR allows quantification of hydrogen solubility in reservoir fluids and continuous monitoring of signal response over time. Measurements on shales and sandstones confirmed that hydrogen occupies the available pore space with minimal interaction and no detectable hysteresis, supporting both its recovery and containment.

While this dissertation has leveraged NMR as a powerful tool to investigate fluid–rock interactions in porous systems and explore their implications for EOR and geostorage, certain limitations remain. Acknowledging these limitations is essential to guide subsequent research efforts and refine existing methodologies. The following recommendations are proposed:

In the first study, hydrocarbon gas mixtures C_1:C_2 (72:28) were injected hydrostatically into preserved samples. To better replicate subsurface conditions, future experiments should be conducted under confining pressure while enabling live monitoring of produced fluids. This setup would provide more accurate estimations of oil and brine recovery factors during HnP-EOR cycles.

In the pressure-step saturation tests, twin samples were individually saturated with brine and dodecane. However, in real subsurface environments, both fluids coexist. A more realistic approach would involve using doped fluids, such as D_2O for water, to facilitate fluid differentiation and improve pore-type partitioning when both oil and water are present.

For the second study involving cement integrity under $scCO_2$ exposure, future research should focus on assessing effective diffusivity under confinement to accurately simulate geostorage conditions. It is also recommended to extend the duration of $scCO_2$ exposure to several months. Such long-term experiments would improve understanding of $scCO_2$ propagation limits, particularly the bi-carbonation reaction and its impact on pore sizes Supplementary measurements like nanoindentation can be used to track changes in mechanical properties such as Young's modulus over time. These measurements should be performed before and after carbonation, as well as at the carbonation front.

In the UHS study, hydrogen was injected from both ends of the core plug. Future investigations could include hydrogen core flooding under confining pressure in brine-saturated sandstones at various injection rates. This would allow for the evaluation of hydrogen displacement efficiency over multiple injections and production cycles. Additionally, in the presence of magnetic field gradients, spatial NMR profiling could provide insights into saturation profiles and reveal potential viscous fingering phenomena along the core length.

Future diffusion experiments in shale formations could utilize D_2O-saturated core plugs containing natural fractures, tested under confining pressure. Such experiments would help assess leakage risks as a function of injection pressure, offering critical insights into long-term containment in geostorage applications.

References

Abrams, M. A., Gong, C., Garnier, C., and Sephton, M. A. 2017. A new thermal extraction protocol to evaluate liquid rich unconventional oil in place and in-situ fluid chemistry. *Marine and Petroleum Geology* **88**: 659-675.

Adriao Cruz, F. 2023. ScCO2-Fluids-Rock Interactions in Nanoporous Media: Applications in Enhanced Oil Recovery and Carbon Geostorage.

Ahmed, R., Shah, S., Osisanya, S., Hassani, S., Omosebi, O., Elgaddafi, R., Maheshwari, H., Srivastava, A., Hwang, J., and Sharma, M. 2015. Effect of H2S and CO2 in HPHT wells on tubulars and cement. *Final project report, prepared under US Department of Interior Bureau of Safety and Environmental Enforcement project* (E12PC00035).

Al-Yaseri, A., Al-Mukainah, H., Yekeen, N., and Al-Qasim, A. S. 2023. Experimental investigation of hydrogen-carbonate reactions via computerized tomography: Implications for underground hydrogen storage. *International Journal of Hydrogen Energy* **48** (9): 3583-3592.

Al Hameli, F., Belhaj, H., and Al Dhuhoori, M. 2022. CO2 sequestration overview in geological formations: Trapping mechanisms matrix assessment. *Energies* **15** (20): 7805.

Amigáň, P., Greksak, M., Kozánková, J., Buzek, F., Onderka, V., and Wolf, I. 1990. Methanogenic bacteria as a key factor involved in changes of town gas stored in an underground reservoir. *FEMS Microbiology Ecology* **6** (3): 221-224.

Bachu, S. 2015. Review of CO2 storage efficiency in deep saline aquifers. *International Journal of Greenhouse Gas Control* **40**: 188-202.

Barlet-Gouedard, V., Rimmele, G., Goffe, B., and Porcherie, O. 2006. Mitigation strategies for the risk of CO2 migration through wellbores. *Proc.,* SPE/IADC Drilling Conference and ExhibitionSPE-98924-MS.

Baur, M. E., Garland, C. W., and Stockmayer, W. H. 1959. Diffusion coefficients of H2O-D2O mixtures. *Journal of the American Chemical Society* **81** (12): 3147-3148.

Bensing, J. P., Misch, D., Skerbisch, L., and Sachsenhofer, R. F. 2022. Hydrogen-induced calcite dissolution in Amaltheenton Formation claystones: Implications for underground hydrogen storage caprock integrity. *International Journal of Hydrogen Energy* **47** (71): 30621-30626.

Bloembergen, N., Purcell, E. M., and Pound, R. V. 1948. Relaxation effects in nuclear magnetic resonance absorption. *Physical review* **73** (7): 679.

Brunauer, S., Emmett, P. H., and Teller, E. 1938. Adsorption of gases in multimolecular layers. *Journal of the American chemical society* **60** (2): 309-319.

Brunner, E. 1985. Solubility of hydrogen in 10 organic solvents at 298.15, 323.15, and 373.15 K. *Journal of chemical and Engineering Data* **30** (3): 269-273.

Buntoro, A. and Rubiandini, R. 2000. The effect of neat magnesium oxide (MgO) as expanding additive on cement shear bond strength at high temperature up to 2500C. *Proc.,* Proceedings World Geothermal Congress.

Cadogan, S. P., Maitland, G. C., and Trusler, J. M. 2014. Diffusion coefficients of CO2 and N2 in water at temperatures between 298.15 K and 423.15 K at pressures up to 45 MPa. *Journal of Chemical & Engineering Data* **59** (2): 519-525.

Cai, H. Y., Shaw, J. M., and Chung, K. H. 2001. Hydrogen solubility measurements in heavy oil and bitumen cuts. *Fuel* **80** (8): 1055-1063. https://www.sciencedirect.com/science/article/pii/S001623610000171X.

Carey, J. W., Wigand, M., Chipera, S. J., WoldeGabriel, G., Pawar, R., Lichtner, P. C., Wehner, S. C., Raines, M. A., and Guthrie Jr, G. D. 2007. Analysis and performance of oil well cement with 30 years of CO2 exposure from the SACROC Unit, West Texas, USA. *International journal of greenhouse gas control* **1** (1): 75-85.

Carroll, S., Carey, J. W., Dzombak, D., Huerta, N. J., Li, L., Richard, T., Um, W., Walsh, S. D., and Zhang, L. 2016. Role of chemistry, mechanics, and transport on well integrity in CO2 storage environments. *International Journal of Greenhouse Gas Control* **49**: 149-160.

Chakravarty, A., Tinni, A., Rai, C. S., and Sondergeld, C. H. 2018. NMR Considerations in Shales at Elevated Temperature. *Proc.,* SPE/AAPG/SEG Unconventional Resources Technology Conference. https://doi.org/10.15530/URTEC-2018-2902883.

Chang, D., Vinegar, H. J., Morriss, C., and Straley, C. 1994. Effective porosity, producible fluid and permeability in carbonates from NMR logging. *Proc.,* SPWLA Annual Logging SymposiumSPWLA-1994-A.

Coates, G. R., Xiao, L., and Prammer, M. G. 1999. NMR logging. *Principles and Interpretation Halliburton Energy Service, Huston, Texas*.

Curtis, M. E., Ambrose, R. J., Sondergeld, C. H., and Rai, C. S. 2011. Investigation of the Relationship between Organic Porosity and Thermal Maturity in the Marcellus Shale. *Proc.,* North American Unconventional Gas Conference and Exhibition. https://doi.org/10.2118/144370-MS.

Curtis, M. E., Cardott, B. J., Sondergeld, C. H., and Rai, C. S. 2012. The Development of Organic Porosity in the Woodford Shale Related To Thermal Maturity. *Proc.,* SPE Annual Technical Conference and Exhibition. https://doi.org/10.2118/160158-MS.

Daigle, H. and Dugan, B. 2009. Extending NMR data for permeability estimation in fine-grained sediments. *Marine and Petroleum Geology* **26** (8): 1419-1427.

Daigle, H. and Dugan, B. 2011. An improved technique for computing permeability from NMR measurements in mudstones. *Journal of Geophysical Research: Solid Earth* **116** (B8).

Dang, S. 2019. Understanding the fundamental drive mechanisms for huff-n-puff enhanced oil recovery in tight formations.

Dang, S., Mamoudou, S., Rai, C., and Sondergeld, C. 2023. Experimental Observation of Diffusion as the Main Drive Mechanism in Unconventional Shales. *Proc.,* SPE/AAPG/SEG Unconventional Resources Technology Conference. https://doi.org/10.15530/urtec-2023-3864848.

Dang, S., Mukherjee, S., Sondergeld, C., and Rai, C. 2021. Measurement of effective tortuosity in unconventional tight rock using nuclear magnetic resonance. *Proc.,* Unconventional Resources Technology Conference, 26–28 July 20211476-1489.

Dang, S. T., Krukowski, E. G., Dick, M. J., Veselinovic, D., Mendoza, R. A., Watson, R., Rai, C., and Sondergeld, C. 2023. Understanding NMR Responses of Different Rock-Fluid Components Within Organic-Rich Argillaceous Rocks: Comparison Study Across 2, 12, and 23 MHz Spectroscopy. *Proc.,* SPE/AAPG/SEG Unconventional Resources Technology Conference. https://doi.org/10.15530/urtec-2023-3863533.

Dang, S. T., Mamoudou, S., Rai, C. S., and Ho, T. A. 2025. *10.1039/D4CP04366A*. Evaluation of hydrogen storage in sandstone reservoirs using 1H nuclear magnetic resonance spectroscopy. *Physical Chemistry Chemical Physics* **27** (3): 1237-1240. http://dx.doi.org/10.1039/D4CP04366A.

Duguid, A. and Scherer, G. W. 2010. Degradation of oilwell cement due to exposure to carbonated brine. *International journal of greenhouse gas control* **4** (3): 546-560.

Duguid, A., Zaluski, W., El-Kaseeh, G., Lee, S.-Y., and Piercy, M. 2019. Well integrity risk assessment to inform containment risk monitoring for carbon capture, utilization, and storage, applied to the Weyburn-Midale Field, Canada. *International Journal of Greenhouse Gas Control* **86**: 226-238.

Dunn, K.-J., Bergman, D. J., and LaTorraca, G. A. 2002. *Nuclear magnetic resonance: Petrophysical and logging applications*: Elsevier.

Flesch, S., Pudlo, D., Albrecht, D., Jacob, A., and Enzmann, F. 2018. Hydrogen underground storage—Petrographic and petrophysical variations in reservoir sandstones from laboratory experiments under simulated reservoir conditions. *International Journal of Hydrogen Energy* **43** (45): 20822-20835.

Fleury, M. and Brosse, E. 2018. Transport in tight rocks. *Geological Carbon Storage: Subsurface Seals and Caprock Integrity*: 31-43.

Fleury, M. and Romero-Sarmiento, M. 2016. Characterization of shales using T1–T2 NMR maps. *Journal of Petroleum Science and Engineering* **137**: 55-62.

Fragoso, A., Wang, Y., Jing, G., and Aguilera, R. 2015. Improving recovery of liquids from shales through gas recycling and dry gas injection. *Proc.,* SPE Latin America and Caribbean Petroleum Engineering ConferenceD011S007R004.

Freedman, R. 2006. Advances in NMR Logging. *Journal of Petroleum Technology* **58** (01): 60-66. https://doi.org/10.2118/89177-JPT.

Frimmel, F. 1996. *Paul N. Cheremisinoff, Handbook of Water and Wastewater Treatment Technology, Marcel Decker, Inc., New York (1994), 840 pp. bound and illustrated, Price: 195 US $, ISBN: 0-8247-9277-7*, Elsevier (Reprint).

Gabrielli, P., Poluzzi, A., Kramer, G. J., Spiers, C., Mazzotti, M., and Gazzani, M. 2020. Seasonal energy storage for zero-emissions multi-energy systems via underground hydrogen storage. *Renewable and Sustainable Energy Reviews* **121**: 109629.

Galle, C. 2001. Effect of drying on cement-based materials pore structure as identified by mercury intrusion porosimetry: A comparative study between oven-, vacuum-, and freeze-drying. *Cement and concrete research* **31** (10): 1467-1477.

Gannaway, G. 2014. NMR investigation of pore structure in gas shales. *Proc.,* SPE Annual Technical Conference and Exhibition?SPE-173474-STU.

Gao, W., Robinson, R. L., and Gasem, K. A. 1999. High-pressure solubilities of hydrogen, nitrogen, and carbon monoxide in dodecane from 344 to 410 K at pressures to 13.2 MPa. *Journal of Chemical & Engineering Data* **44** (1): 130-132.

Gardeh, M. G., Kistanov, A. A., Nguyen, H., Manzano, H., Cao, W., and Kinnunen, P. 2022. Exploring mechanisms of hydration and carbonation of MgO and Mg (OH) 2 in reactive magnesium oxide-based cements. *The Journal of Physical Chemistry C* **126** (14): 6196-6206.

Gerritsma, C. J., Oosting, P. H., and Trappeniers, N. J. 1971. Proton-spin-lattice relaxation and self-diffusion in methanes: II. Experimental results for proton-spin-lattice relaxation times. *Physica* **51** (3): 381-394. https://www.sciencedirect.com/science/article/pii/0031891471900486.

Gherardi, F., Audigane, P., and Gaucher, E. C. 2012. Predicting long-term geochemical alteration of wellbore cement in a generic geological CO2 confinement site: Tackling a difficult reactive transport modeling challenge. *Journal of Hydrology* **420**: 340-359.

Hassanpouryouzband, A., Adie, K., Cowen, T., Thaysen, E. M., Heinemann, N., Butler, I. B., Wilkinson, M., and Edlmann, K. 2022. Geological hydrogen storage: geochemical reactivity of hydrogen with sandstone reservoirs. *ACS Energy Letters* **7** (7): 2203-2210.

Hassanpouryouzband, A., Joonaki, E., Edlmann, K., Heinemann, N., and Yang, J. 2020. Thermodynamic and transport properties of hydrogen containing streams. *Scientific Data* **7** (1): 222.

Hawthorne, S. B., Miller, D. J., Grabanski, C. B., Sorensen, J. A., Pekot, L. J., Kurz, B. A., Gorecki, C. D., Steadman, E. N., Harju, J. A., and Melzer, S. 2017. Measured crude oil MMPs with pure and mixed CO2, methane, and ethane, and their relevance to enhanced oil recovery from middle Bakken and Bakken shales. *Proc.,* SPE Canada Unconventional Resources Conference?D021S009R007.

Hawthorne, S. B., Miller, D. J., Jin, L., and Gorecki, C. D. 2016. Rapid and simple capillary-rise/vanishing interfacial tension method to determine crude oil minimum miscibility pressure: pure and mixed CO2, methane, and ethane. *Energy & Fuels* **30** (8): 6365-6372.

Heinemann, N., Alcalde, J., Miocic, J. M., Hangx, S. J., Kallmeyer, J., Ostertag-Henning, C., Hassanpouryouzband, A., Thaysen, E. M., Strobel, G. J., and Schmidt-Hattenberger, C. 2021. Enabling large-scale hydrogen storage in porous media–the scientific challenges. *Energy & Environmental Science* **14** (2): 853-864.

Hemme, C. and Van Berk, W. 2018. Hydrogeochemical modeling to identify potential risks of underground hydrogen storage in depleted gas fields. *Applied Sciences* **8** (11): 2282.

Henkel, S., Pudlo, D., Werner, L., Enzmann, F., Reitenbach, V., Albrecht, D., Würdemann, H., Heister, K., Ganzer, L., and Gaupp, R. 2014. Mineral reactions in the geological underground induced by H2 and CO2 injections. *Energy Procedia* **63**: 8026-8035.

Higgs, S., Da Wang, Y., Sun, C., Ennis-King, J., Jackson, S. J., Armstrong, R. T., and Mostaghimi, P. 2022. In-situ hydrogen wettability characterisation for underground hydrogen storage. *International Journal of Hydrogen Energy* **47** (26): 13062-13075.

Hirasaki, G. and Mohanty, K. 2007. Fluid-Rock Characterization for NMR Well Logging and Special Core Analysis, Rice Univ., Houston, TX (United States).

Hirasaki, G. J., Lo, S.-W., and Zhang, Y. 2003. NMR properties of petroleum reservoir fluids. *Magnetic resonance imaging* **21** (3-4): 269-277.

Ho, T. A., Dang, S. T., Dasgupta, N., Choudhary, A., Rai, C. S., and Wang, Y. 2024. Nuclear magnetic resonance and molecular simulation study of H2 and CH4 adsorption onto shale and sandstone for hydrogen geological storage. *International Journal of Hydrogen Energy* **51**: 158-166.

Hoffman, B. T. 2018. Huff-N-Puff gas injection pilot projects in the eagle ford. *Proc.,* SPE Canada Unconventional Resources Conference?D012S001R001.

Hosseini, M., Ali, M., Fahimpour, J., Keshavarz, A., and Iglauer, S. 2022. Basalt-H2-brine wettability at geo-storage conditions: Implication for hydrogen storage in basaltic formations. *Journal of Energy Storage* **52**: 104745.

Hosseini, M., Fahimpour, J., Ali, M., Keshavarz, A., and Iglauer, S. 2022. Hydrogen wettability of carbonate formations: Implications for hydrogen geo-storage. *Journal of Colloid and Interface Science* **614**: 256-266.

Huerta, N. J., Hesse, M. A., Bryant, S. L., Strazisar, B. R., and Lopano, C. L. 2013. Experimental evidence for self-limiting reactive flow through a fractured cement core: Implications for time-dependent wellbore leakage. *Environmental science & technology* **47** (1): 269-275.

Iglauer, S., Ali, M., and Keshavarz, A. 2021. Hydrogen wettability of sandstone reservoirs: implications for hydrogen geo-storage. *Geophysical Research Letters* **48** (3): e2020GL090814.

Ji, S., Wang, Z., Guo, A., Zhou, Y., and Chen, K. 2013. Determination of Hydrogen Solubility in Heavy Fractions of Crude Oils by a Modified Direct Method. *Journal of Chemical & Engineering Data* **58** (12): 3453-3457. https://doi.org/10.1021/je400729v.

Kausik, R., Fellah, K., Rylander, E., Singer, P. M., Lewis, R. E., and Sinclair, S. M. 2016. NMR Relaxometry in Shale and Implications for Logging. *Petrophysics - The SPWLA Journal of Formation Evaluation and Reservoir Description* **57** (04): 339-350.

Kausik, R., Minh, C. C., Zielinski, L., Vissapragada, B., Akkurt, R., Song, Y., Liu, C., Jones, S., and Blair, E. 2011. Characterization of gas dynamics in kerogen nanopores by NMR. *Proc.,* SPE Annual Technical Conference and Exhibition?SPE-147198-MS.

Kelly, S., Bonnie, R. J. M., Dick, M. J., and Veselinovic, D. 2021. NMR Wettability Index Measurements and Methods Compared on a Variety of Unconventional Samples. *Proc.,* SPWLA 62nd Annual Logging Symposium. https://doi.org/10.30632/SPWLA-2021-0096.

Kenyon, W. 1997. Petrophysical principles of applications of NMR logging. *The log analyst* **38** (02).

Kim, C., Devegowda, D., Dang, S. T., and Mehana, M. 2025. Modeling the diffusivity of hydrogen and the associated cushion gas in depleted hydrocarbon reservoir caprocks. *International Journal of Hydrogen Energy* **105**: 248-257. https://www.sciencedirect.com/science/article/pii/S0360319925000680.

Kleinberg, R. L. 1996. Utility of NMR T2 distributions, connection with capillary pressure, clay effect, and determination of the surface relaxivity parameter ρ2. *Magnetic resonance imaging* **14** (7-8): 761-767.

Kleinberg, R. L. 2001. NMR well logging at Schlumberger. *Concepts in magnetic Resonance* **13** (6): 396-403.

Kleinberg, R. L. and Jackson, J. A. 2001. An introduction to the history of NMR well logging. *Concepts in Magnetic Resonance* **13** (6): 340-342.

Kravanja, G. and Knez, Ž. 2023. Carbonization of Class G well cement containing metakaolin under supercritical and saturated environments. *Construction and Building Materials* **376**: 131050.

Kruyer, S. and Nobel, A. 1961. Solubility of hydrogen in benzene, cyclohexane, decalin, phenol and cyclohexanol. *Recueil des Travaux Chimiques des Pays-Bas* **80** (10): 1145-1156.

Kutchko, B. G., Strazisar, B. R., Dzombak, D. A., Lowry, G. V., and Thaulow, N. 2007. Degradation of well cement by CO2 under geologic sequestration conditions. *Environmental science & technology* **41** (13): 4787-4792.

Kutchko, B. G., Strazisar, B. R., Hawthorne, S. B., Lopano, C. L., Miller, D. J., Hakala, J. A., and Guthrie, G. D. 2011. H2S–CO2 reaction with hydrated Class H well cement: Acid-gas injection and CO2 Co-sequestration. *International Journal of Greenhouse Gas Control* **5** (4): 880-888.

Kutchko, B. G., Strazisar, B. R., Huerta, N., Lowry, G. V., Dzombak, D. A., and Thaulow, N. 2009. CO2 reaction with hydrated class H well cement under geologic sequestration conditions: Effects of flyash admixtures. *Environmental science & technology* **43** (10): 3947-3952.

Kutchko, B. G., Strazisar, B. R., Lowry, G. V., Dzombak, D. A., and Thaulow, N. 2008. Rate of CO2 attack on hydrated class H well cement under geologic sequestration conditions. *Environmental science & technology* **42** (16): 6237-6242.

Li, L. and Sheng, J. J. 2016. Experimental study of core size effect on CH4 huff-n-puff enhanced oil recovery in liquid-rich shale reservoirs. *Journal of Natural Gas Science and Engineering* **34**: 1392-1402.

Li, L., Sheng, J. J., and Xu, J. 2017. Gas selection for huff-n-puff EOR in shale oil reservoirs based upon experimental and numerical study. *Proc.,* SPE Canada Unconventional Resources Conference?D011S001R007.

Loucks, R. G., Ruppel, S., Reed, R. M., Hammes, U., and Zahm, C. 2011. Origin and classification of pores in mudstones from shale-gas systems. *Search and Discovery article* **40855**: 1-32.

Luo, A., Li, Y., Chen, X., Zhu, Z., and Peng, Y. 2022. Review of CO2 sequestration mechanism in saline aquifers. *Natural Gas Industry B* **9** (4): 383-393.

Luquot, L., Abdoulghafour, H., and Gouze, P. 2013. Hydro-dynamically controlled alteration of fractured Portland cements flowed by CO2-rich brine. *International Journal of Greenhouse Gas Control* **16**: 167-179.

Mamoudou, S., Curtis, M., Dang, S., and Rai, C. 2024. Experimental evaluation of cement integrity on exposure to supercritical CO2 using NMR: Application to geostorage. *Heliyon* **10** (2).

Mamoudou, S., Dang, S., Curtis, M., and Rai, C. 2024. Evaluation of Hydrogen Interaction with Mudrocks: Implication for Geo-Storage. *Proc.,* SPE/AAPG/SEG Unconventional Resources Technology Conference. https://doi.org/10.15530/urtec-2024-4042532.

Mamoudou, S., Dang, S., and Rai, C. 2025. Hydrogen interaction in bulk fluids for geological storage application using NMR. *Next Energy* **7**: 100298. https://www.sciencedirect.com/science/article/pii/S2949821X25000614.

Mamoudou, S., Perez, F., Tinni, A., Dang, S., Sondergeld, C. H., Rai, C. S., and Devegowda, D. 2020. Evaluation of Huff-n-Puff in Shale Using Experiments and Molecular Simulations. In *Unconventional Resources Technology Conference, Virtual, 20–22 July 2020*, 1944-1961.

Mamoudou, S., Tinni, A., Curtis, M., Sondergeld, C. H., and Rai, C. S. 2021. Impact of EOR Huff-n-puff on rock microstructure. *Proc.,* Unconventional Resources Technology Conference, 26–28 July 2021384-396.

Markham, A. E. and Kobe, K. A. 1941. The Solubility of Gases in Liquids. *Chemical Reviews* **28** (3): 519-588.

Mason, H. E., Du Frane, W. L., Walsh, S. D., Dai, Z., Charnvanichborikarn, S., and Carroll, S. A. 2013. Chemical and mechanical properties of wellbore cement altered by CO2-rich brine using a multianalytical approach. *Environmental science & technology* **47** (3): 1745-1752.

Matteson, A., Tomanic, J., Herron, M., Allen, D., and Kenyon, W. 2000. NMR relaxation of clay/brine mixtures. *SPE Reservoir Evaluation & Engineering* **3** (05): 408-413.

Min, B., Mamoudou, S., Dang, S., Tinni, A., Sondergeld, C., and Rai, C. 2020. Comprehensive experimental study of huff-n-puff enhanced oil recovey in eagle ford: Key parameters and recovery mechanism. *Proc.,* SPE Improved Oil Recovery Conference.

Miocic, J., Heinemann, N., Edlmann, K., Scafidi, J., Molaei, F., and Alcalde, J. 2023. Underground hydrogen storage: a review. *Geological Society, London, Special Publications* **528** (1): SP528-2022-88.

Mitchell, J., Gladden, L., Chandrasekera, T., and Fordham, E. 2014. Low-field permanent magnets for industrial process and quality control. *Progress in nuclear magnetic resonance spectroscopy* **76**: 1-60.

Odiachi, J., Cruz, F., and Tinni, A. 2022. Diffusional and Electrical Tortuosity in Unconventional Shale Reservoirs. *Proc.,* SPE Annual Technical Conference and Exhibition?D011S018R006.

Odusina, E., Sondergeld, C., and Rai, C. 2011. An NMR study on shale wettability. *Proc.,* SPE Canada Unconventional Resources Conference?SPE-147371-MS.

Panfilov, M. 2010. Underground storage of hydrogen: in situ self-organisation and methane generation. *Transport in porous media* **85**: 841-865.

Perez, F. and Devegowda, D. 2020. A Molecular Dynamics Study of Soaking During Enhanced Oil Recovery in Shale Organic Pores. *SPE Journal* **25** (02): 832-841. https://doi.org/10.2118/199879-PA.

Perkins, T. K. and Johnston, O. C. 1963. A Review of Diffusion and Dispersion in Porous Media. *Society of Petroleum Engineers Journal* **3** (01): 70-84. https://doi.org/10.2118/480-PA.

Qazvini, A. and Torabi, F. 2012. Feasibility study of solvent-based huff-n-puff method (cyclic solvent injection) to enhance heavy oil recovery. *Proc.,* SPE Canada Heavy Oil ConferenceSPE-157853-MS.

Rassenfoss, S. 2017. Shale EOR works, but will it make a difference? *Journal of Petroleum Technology* **69** (10): 34-40.

Rimmelé, G., Barlet-Gouédard, V., Porcherie, O., Goffé, B., and Brunet, F. 2008. Heterogeneous porosity distribution in Portland cement exposed to CO2-rich fluids. *Cement and Concrete Research* **38** (8-9): 1038-1048.

Sheng, J. J. 2017. Optimization of huff-n-puff gas injection in shale oil reservoirs. *Petroleum* **3** (4): 431-437.

Sinha, A. 2017. Surface area study in organic rich shales using nitrogen adsorption.

Sondergeld, C., Curtis, M., Dang, S., Mamoudou, S., and Rai, C. 2022. Does EOR in unconventionals change the rock? *Fuel* **310**: 122176. https://www.sciencedirect.com/science/article/pii/S0016236121020524.

Sondergeld, C. and Rai, C. 1993. A new concept in quantitative core characterization. *The Leading Edge* **12** (7): 774-779.

Sondergeld, C. H. and Rai, C. S. 1994. A new exploration tool: Quantitative core characterization. *Experimental Techniques in Mineral and Rock Physics: The Schreiber Volume*: 249-268.

Song, Y.-Q. and Kausik, R. 2019. NMR application in unconventional shale reservoirs – A new porous media research frontier. *Progress in Nuclear Magnetic Resonance Spectroscopy* **112-113**: 17-33. https://www.sciencedirect.com/science/article/pii/S0079656519300159.

Sulucarnain, I., Sondergeld, C. H., and Rai, C. S. 2012. An NMR study of shale wettability and effective surface relaxivity. *Proc.,* SPE Canada Unconventional Resources Conference?SPE-162236-MS.

Thomas, W. R., Helms, L. W., Driggers, T., Trice, D. W., and Thomas, G. L. 2016. EOG Resources (EOG) Earnings Call. *May* **6**: 2016.

Timur, A. 1968. Effective porosity and permeability of sandstones investigated through nuclear magnetic resonance principles. *Proc.,* SPWLA Annual Logging SymposiumSPWLA-1968-K.

Timur, A. 1969. Pulsed nuclear magnetic resonance studies of porosity, movable fluid, and permeability of sandstones. *Journal of Petroleum Technology* **21** (06): 775-786.

Tinni, A. 2015. Pore connectivity and hydrocarbon storage in shale reservoirs.

Tinni, A., Odusina, E., Sulucarnain, I., Sondergeld, C., and Rai, C. S. 2015. Nuclear-Magnetic-Resonance Response of Brine, Oil, and Methane in Organic-Rich Shales. *SPE Reservoir Evaluation & Engineering* **18** (03): 400-406. https://doi.org/10.2118/168971-PA.

Tinni, A., Sondergeld, C., and Rai, C. 2014. NMR T1-T2 response of moveable and non-moveable fluids in conventional and unconventional rocks. *Proc.,* International symposium of the society of core analysts, avignon, france8-11.

Truche, L., Berger, G., Destrigneville, C., Guillaume, D., and Giffaut, E. 2010. Kinetics of pyrite to pyrrhotite reduction by hydrogen in calcite buffered solutions between 90 and 180°C: Implications for nuclear waste disposal. *Geochimica et Cosmochimica Acta* **74** (10): 2894-2914. https://www.sciencedirect.com/science/article/pii/S0016703710000979.

Truche, L., Jodin-Caumon, M.-C., Lerouge, C., Berger, G., Mosser-Ruck, R., Giffaut, E., and Michau, N. 2013. Sulphide mineral reactions in clay-rich rock induced by high hydrogen pressure. Application to disturbed or natural settings up to 250 C and 30 bar. *Chemical Geology* **351**: 217-228.

Um, W., Rod, K. A., Jung, H. B., and Brown, C. F. 2017. Geochemical alteration of wellbore cement by CO2 or CO2+ H2S reaction during long-term carbon storage. *Greenhouse Gases: Science and Technology* **7** (5): 852-865.

van der Meer, L. B., Hofstee, C., and Orlic, B. 2009. The fluid flow consequences of CO2 migration from 1000 to 600 metres upon passing the critical conditions of CO2. *Energy Procedia* **1** (1): 3213-3220.

Walsh, S. D., Du Frane, W. L., Mason, H. E., and Carroll, S. A. 2013. Permeability of wellbore-cement fractures following degradation by carbonated brine. *Rock Mechanics and Rock Engineering* **46**: 455-464.

Walsh, S. D., Mason, H. E., Du Frane, W. L., and Carroll, S. A. 2014a. Experimental calibration of a numerical model describing the alteration of cement/caprock interfaces by carbonated brine. *International Journal of Greenhouse Gas Control* **22**: 176-188.

Walsh, S. D., Mason, H. E., Du Frane, W. L., and Carroll, S. A. 2014b. Mechanical and hydraulic coupling in cement–caprock interfaces exposed to carbonated brine. *International Journal of Greenhouse Gas Control* **25**: 109-120.

Wang, X., Luo, P., Er, V., and Huang, S. 2010. Assessment of CO2 flooding potential for Bakken formation, Saskatchewan. *Proc.,* SPE Canada Unconventional Resources Conference?SPE-137728-MS.

Wigand, M., Kaszuba, J. P., Carey, J. W., and Hollis, W. K. 2009. Geochemical effects of CO2 sequestration on fractured wellbore cement at the cement/caprock interface. *Chemical Geology* **265** (1-2): 122-133.

Yekta, A. E., Pichavant, M., and Audigane, P. 2018. Evaluation of geochemical reactivity of hydrogen in sandstone: Application to geological storage. *Applied Geochemistry* **95**: 182-194.

Yu, Y., Li, L., and Sheng, J. J. 2016. Further discuss the roles of soaking time and pressure depletion rate in gas huff-n-puff process in fractured liquid-rich shale reservoirs. *Proc.,* SPE Annual Technical Conference and Exhibition?D021S035R005.

Zainuddin, W. N., Xie, S. X., Kechut, N. I., Kantaatmadja, B. P., Singer, P. M., and Hirasaki, G. J. 2019. Hydrogen-Deuterium Exchange Between Rock Minerals and D2O. *Proc.,* SPE Middle East Oil and Gas Show and Conference. https://doi.org/10.2118/194978-MS.

Zarghami, S., Boukadi, F., and Al-Wahaibi, Y. 2017. Diffusion of carbon dioxide in formation water as a result of CO 2 enhanced oil recovery and CO 2 sequestration. *Journal of Petroleum Exploration and Production Technology* **7**: 161-168.

Zeng, L., Hosseini, M., Keshavarz, A., Iglauer, S., Lu, Y., and Xie, Q. 2022. Hydrogen wettability in carbonate reservoirs: Implication for underground hydrogen storage from geochemical perspective. *International Journal of Hydrogen Energy* **47** (60): 25357-25366.

Zivar, D., Kumar, S., and Foroozesh, J. 2021. Underground hydrogen storage: A comprehensive review. *International journal of hydrogen energy* **46** (45): 23436-23462.